# INVESTIGATION OF ADVANCED GaN HEMTs FOR DIGITAL AND HIGH FREQUENCY APPLICATIONS

Dissertation

zur Erlangung des akademischen Grades

Doktoringenieur (Dr.-Ing.)

Vorgelegt der Fakultät für Elektrotechnik und Informationstechnik der Technischen Universität Ilmenau

von Herrn

Nader Al Mustafa

Gutachter: 1. PD Dr.-lng. habil. Frank Schwierz (Betreuer)

2. Univ.-Prof. Dr.-lng. habil. Hannes Töpfer

3. Dr.-lng. Ralf Granzner

Tag der wissenschaftlichen Aussprache: 22.11.2019

urn:nbn:de:gbv:ilm1-2019000577

## Acknowledgment

Firstly, I would like to express my sincere gratitude to my supervisor PD Dr. habil. Frank Schwierz for the continuous support of my Ph.D. study and research, for his patience, motivation, and immense knowledge. My sincere thanks also go to Dr. Ralf Granzner for his help, discussion, and enthusiasm throughout my process

Thanks as well to Dr. Mario Kittler for his support of this work and for support of computer and software problems.

I would like to thank Dr. rer. nat. Jörg Pezoldt, Nanotechnology Institute at the TU Ilmenau, for many helpful discussions. Dr. Vladimir Polyakov, Fraunhofer Institute for Applied Solid State Physics IAF.

Warmly thanks to Faculty of Science, University of Damascus, Syria for their support during my Ph.D. study.

I am very grateful to my Mother, my Father, my sisters and my brothers for all their love and support. Of course I will never forget my wife Shereen and my sons, Muhammad and Shaker for their encouragement, patience and support throughout my life.

## Zusammenfassung

Die physikalischen Eigenschaften des Galliumnitrid (GaN) und der darauf basierenden Materialien eignen sich besonders zur Herstellung von leistungselektronischen Bauelementen. Die große Bandlücke und hohe elektrische Durchbruchfeldstärke von GaN in Kombination mit einem zweidimensionalen Elektronengas hoher Dichte durch induzierte Polarisation in der AlGaN/GaN-Grenzfläche ermöglicht die Entwicklung von Transistoren mit hohen Sperrspannungen, niedrigen Durchlasswiderständen und niedrigen Schaltladungen. Die aus herkömmlichen GaN-HEMTs hergestellten Transistoren haben jedoch bereits ihre Leistungsgrenze erreicht. Um die zukünftigen Bedürfnisse von leistungselektronischen Bauelementen zu erfüllen, werden Forschungen zu nichtklassischen HEMT-Konzepten, zum Beispiel Superjunction GaN-HEMT, PNT GaN-HEMTs oder zu neuartigen Barrierematerialien durchgeführt.

Diese Arbeit will die GaN-Technologie durch neue Ansätze in Design und Charakterisierung hocheffizienter GaN-Transistoren vorantreiben, um ihr volles Potential zu entfalten.

Das Ziel der vorliegenden Arbeit ist es, verschiedene nichtklassische GaN HEMT-Konzepte hinsichtlich ihrer Performance sowie ihrer Eignung für zukünftige Logik, leistungselektronisch und RF Anwendungen zu bewerten und ihren Designspielraum einzugrenzen. Die Untersuchungen basieren auf numerischen Bauelementesimulationen unter Zuhilfenahme analytischer Berechnungen. Es wird gezeigt, dass das einfache und robuste Drift-Diffusionsmodell für die Simulation solcher nichtklassischen Bauelemente geeignet ist.

Die Koexistenz von zweidimensionalen Elektronen- und Löchergasen in GaN-basierten Heterostrukturen wird mittels analytischer Modelle, die im Rahmen dieser Arbeit entwickelt wurden, und selbstkonsistenten numerischen Lösungen der Schrödinger- und Poisson-Gleichungen untersucht.

Es kann gezeigt werden, dass für bestimmte Kombinationen von Bias-Bedingungen und Schichtdesign koexistierende 2DEGs und 2DHGs in GaN/AlGaN/GaN-Strukturen gebildet werden können, wobei sich das 2DHG an der Grenzfläche zwischen Grenzfläche und Grenzfläche befindet. Sobald ein 2DHG erzeugt ist, nimmt der Effekt der Gate-Spannung auf das 2DEG schnell ab und eine Sättigung der 2DEG-Dichte wird beobachtet. Außerdem ist es

in Strukturen mit dünnen Barrieren viel schwieriger, ein 2DHG selbst für große Oberflächenpotentiale zu erzeugen.

Die Formierung eines zweiten Kanals in AlGaN/GaN/AlGaN/GaN Heterostrukturen wurde untersucht. Es wurde gezeigt, dass für bestimmte Kombinationen von Bias-Bedingungen und Schichtdesign koexistierende zwei Kanäle in AlGaN2/GaN2/AlGaN1/GaN1-Strukturen gebildet werden können, wobei sich beide Kanäle am AlGaN1/GaN1 und AlGaN2/GaN2 befinden. Sobald der zweite Kanal erzeugt ist, nimmt die Wirkung der Gate-Spannung auf das erste 2DEG schnell ab und eine Sättigung des Drain-Stroms wird beobachtet. Besondere Aufmerksamkeit wurde auf einen neuartigen Inverter mit vertikalem Aufbauen gelegt, indem diese zwei Kanäle verwendet wurden.

Andererseits konzentrieren sich theoretische Untersuchungen von AlGaN/GaN-HEMT-Strukturen für leistungselektronische Anwendungen auf die Abschätzung von Oxidgrenzflächenladungen in MIS-HEMT-Strukturen, und es werden zwei Simulationsstudien zu alternativen selbstsperrenden HEMT-Konzepten vorgestellt.

Die Untersuchung von Oxidgrenzflächenladungen basiert auf einem Vergleich von gemessenen und simulierten Schwellenspannungen experimenteller HEMTs mit und ohne $Al_2O_3$-Schicht unter dem Gate. Wir finden, dass in beiden Fällen die geschätzte Oxidgrenzflächenladung die gleiche ist. Darüber hinaus entwickelten wir ein einfaches analytisches Schwellenspannungsmodell für die MIS HEMT Struktur, mit dem die Grenzflächenladung mit einem Taschenrechner abgeschätzt werden kann. Wir schlagen auch einen neuen Ansatz vor, bei dem die Wirkung einer p-dotierten Deckschicht mit der eines Gateoxids kombiniert wird, um einen selbstsperrenden HEMT zu erreichen. Wir konzentrieren uns auf die von Ota et al. mit 1D-Schrödinger-Poisson-Simulationen. Insbesondere zeigt unser analytisches Modell, dass die Schwellenspannung unabhängig von der Dicke sowohl der PNT-Schicht als auch der gespannten GaN-Kanalschicht ist. Darüber hinaus diskutieren wir Optionen zur Erhöhung der Elektronendichte in den ungesteuerten (ungated) Bauelementbereichen, um die Source/Drain-Widerstände zu reduzieren.

Darüber hinaus werden gated kubische InGaN/InN-Heterostrukturen für die Anwendung in InN-basierten Transistoren mit hoher Elektronenmobilität theoretisch untersucht. Die Bildung zweidimensionaler Trägergase in InGaN/InN-Strukturen wird im Detail untersucht und Designprobleme für die InGaN-Barriere untersucht. Es wird gezeigt, dass für bestimmte Oberflächenpotentiale eine unerwünschte Sättigung der Schichtdichte des Elektronengases in

der InN-Kanalschicht auftreten kann. Optionen zur Verbesserung der Elektronendichte in den Kanal- und Oberflächenpotentialbereichen für einen geeigneten Transistorbetrieb werden vorgestellt.

Abschließend wird die Bildung zweidimensionaler Elektronengase (2DEGs) in gitterangepassten AlScN/GaN- und AlYN/GaN-Heterostrukturen durch numerische selbstkonsistente Lösungen der Schrödinger- und Poisson-Gleichungen untersucht. Die Elektronenkonzentrationsprofile und die resultierenden 2DEG-Schichtdichten in diesen Heterostrukturen werden berechnet und mit denen verglichen, die an AlGaN/GaN-Grenzflächen auftreten. Die kombinierte Wirkung der stark polarisationsinduzierten gebundenen Ladungen und der großen Leitungsbandoffsets an den AlScN/GaN- und AlYN/GaN-Heteroübergängen führt zur Bildung von 2DEGs mit sehr hohen Elektronendichtedichten. Für die AlScN/GaN- und AlYN/GaN-Heterostrukturen werden 2DEG-Schichtdichten von etwa 4 bis 5-mal so groß wie für $Al_{0,3}Ga_{0,7}N$/GaN-Strukturen berechnet. Unsere Ergebnisse demonstrieren das Potenzial von AlScN- und AlYN-Barrieren für GaN-basierte Transistoren mit hoher Elektronenmobilität.

## Abstract

The physical features of Gallium nitride (GaN) and the related materials make them very suitable for the fabrication of power semiconductor devices. The large band gap and high electrical breakdown field strength of GaN in combination with high-density two-dimensional electron gases induced by polarization in AlGaN/GaN interface enables the development of transistors with high off-state voltages, low on-state resistances and low switching charges. However the transistors made of conventional GaN HEMTs have already approached their performance limit. In order to meet the future needs of power semiconductor devices, research efforts are being put on nonclassical HEMT concepts e.g. superjunction GaN HEMTs, PNT GaN HEMTs and GaN MIS FETs or on using a new barrier materials such AlScN and AlYN.

This work aims to push GaN technology by new approaches in design and characterization of highly-efficient GaN transistors in order to release its full potential.

The aim of the present work is the evaluation of different nonclassical GaN HEMT concepts regarding their performance and suitability for logic, power-switching and RF ampflication applications and to define their design space. The investigations are based on numerical device simulations supported by analytical calculations. It is shown that the simple and robust drift-diffusion model is well suited for the simulation of such nonclassical devices.

The co-existence of two dimensional- electron and hole gases in GaN-based heterostructures is investigated by means of analytical models, developed in the frame of this work, and self-consistent numerical solutions of the Schrödinger and Poisson equations.

It is shown that for certain combinations of bias conditions and layer design coexisting 2DEGs and 2DHGs can be formed in GaN/AlGaN/GaN structures, where the 2DHG is located at the cap/barrier interface and the 2DEG resides at the barrier/bulk interface. Once a 2DHG is created, the effect of the gate voltage on the 2DEG diminishes rapidly and a saturation of the 2DEG density is observed. Furthermore, in structures with thin barriers it is much more difficult to create a 2DHG even for large surface potentials.

The formation of second channel in AlGaN/GaN/AlGaN/GaN heterostructures has been investigated. It has been shown that for certain combinations of bias conditions and layer design coexisting two channels can be formed in AlGaN2/GaN2/AlGaN1/GaN1 structures where both channels are located at the AlGaN1/GaN1 and AlGaN2/GaN2. Once a second channel is

created, the effect of the gate voltage on the first 2DEG diminishes rapidly and a saturation of the drain current is observed. Special attention was paid to a novel vertical inverter design by employing these two channels.

On the other hand, theoretical investigations of AlGaN/GaN HEMT structures for power switch applications focus on the estimation of oxide interface charges in MIS HEMT structures and on two simulation studies dealing with alternative normally-off HEMT concepts.

The study on oxide interface charges is based on a comparison of measured and simulated threshold voltages of HEMTs with and without an oxide layer underneath the gate. Moreover, we developed a simple analytical threshold voltage model for the MIS HEMT structure which can be used to estimate the interface charge with a pocket calculator. We propose also a new approach to combine the effect of a p-type doped cap layer with that of a gate oxide for designing and achieving normally-off HEMT. We focus on the structures proposed by Ota et al. using 1D Schrödinger-Poisson simulations and analytical models. In particular, our analytical model shows that the threshold voltage is independent on the thicknesses of both the PNT layer and the strained GaN channel layer. Additionally, we discuss options to increase the electron sheet density in the ungated regions in order to reduce the source/drain resistances.

Moreover, gated cubic InGaN/InN heterostructures for application in InN-based HEMTs are investigated theoretically. The formation of two-dimensional carrier gases in InGaN/InN structures is studied in detail and design issues for the InGaN barrier are investigated. It is shown that for certain surface potentials an undesirable saturation of the sheet density of the electron gas in the InN channel layer may occur. Options to enhance the electron sheet density in the channel and surface potential ranges for proper transistor operation are presented.

Finally, the formation of two-dimensional electron gases in lattice-matched AlScN/GaN and AlYN/GaN heterostructures is investigated by numerical self-consistent solutions of the Schrödinger and Poisson equations. The electron concentration profiles and the resulting 2DEG sheet densities in these heterostructures are calculated and compared to those occurring at AlGaN/GaN interfaces. The combined effect of the strong polarization-induced bound charges and the large conduction band offsets at the AlScN/GaN and AlYN/GaN heterojunctions results in the formation of 2DEGs with very high electron sheet densities.about 4 … 5 times as large as those in $Al_{0.3}Ga_{0.7}N$/GaN. Our results demonstrate the potential of AlScN and AlYN barriers for GaN-based high electron mobility transistors.

# TABLE OF CONTENT

# 1. Introduction

At the present time it is hard to imagine our life without electronics. Electronics industry impacts lives through its myriad of services and products offered by the healthcare, automotive and consumers industries, among others.

The development of electronics devices began with the first transistor in 1947. An important step was the invention of the metal-oxide-semiconductor field-effect-transistor (MOSFET) and of the integrated circuit in 1959 [1].

Since these dates, the semiconductor industry has been dominated by silicon (Si). This is largely due to the cost and the ease of creating a native oxide on Si which enables the well-established complementary metal-oxide-semiconductor (CMOS) process which has revolutionised the digital world we live in.

Although Si (medium band gap material) is used in the power semiconductor devices, however, silicon based power devices rapidly reached the theoretical limit of silicon material.

However, there are some novel Si-based device structures such as insulated-gate bipolar transistor (IGBT) and Superjunction MOSFET that pushed silicon power device beyond the traditional silicon power device performance limit. Unfortunately, these devices suffer from high switching loss and limited switching frequency range.

Therefore, new materials with superior properties are needed as potential replacements. These materials are, in particular, gallium nitride (GaN), silicon carbide (SiC) and diamond.

The first GaN based transistors were realised in 1990's [2, 3] and since then have been extensively researched and developed, due the outstanding properties of GaN such as wide bandgap and good electron transport properties, for power amplification at high frequencies and high-voltage power switches [4-8].

A characteristic feature of GaN is its wide band gap (band gap energy $E_g$ = 3.4 eV). The wide energy band gap generally translates into the ability to support high internal electric fields before electronic breakdown occurs. Besides these advantages, GaN has the ability to form heterojunctions to wider band gap semiconductors such as aluminium gallium nitride (AlGaN) or aluminium nitride (AlN) with band gaps up to 6.2 eV. The direct result of forming such heterojunctions is the formation of a two-dimensional electron gas (2DEG) with high sheet

density at the interface between the AlGaN barrier and the GaN channel layer. Due to strong polarization effects, 2DEGs with sheet densities exceeding $10^{13}$ $cm^{-2}$ are easily formed even without intentionally doping the AlGaN barrier [9, 10].

These properties can be exploited to realise devices which have the ability to provide high output power and can be operated as power switches or power amplifiers. GaN power devices are expected to prevail in high end applications over more traditional semiconductors devices based on Si or gallium arsenide (GaAs) with GaN offering up to five times the power density of GaAs. By 2022 it is expected that GaN devices will have a market value of around $2.6 billion [11]. MarketsandMarkets, the second-largest market research firm worldwide in terms of premium market research reports published annually, published a report in February 2016 titled "GaN Power Devices Market - Global Forecast to 2022", which outlined their expectation that the global gallium nitride (GaN) power device market will rise at a compound annual growth rate (CAGR) of 24.5% from 2016 to $2.6bn in 2022.

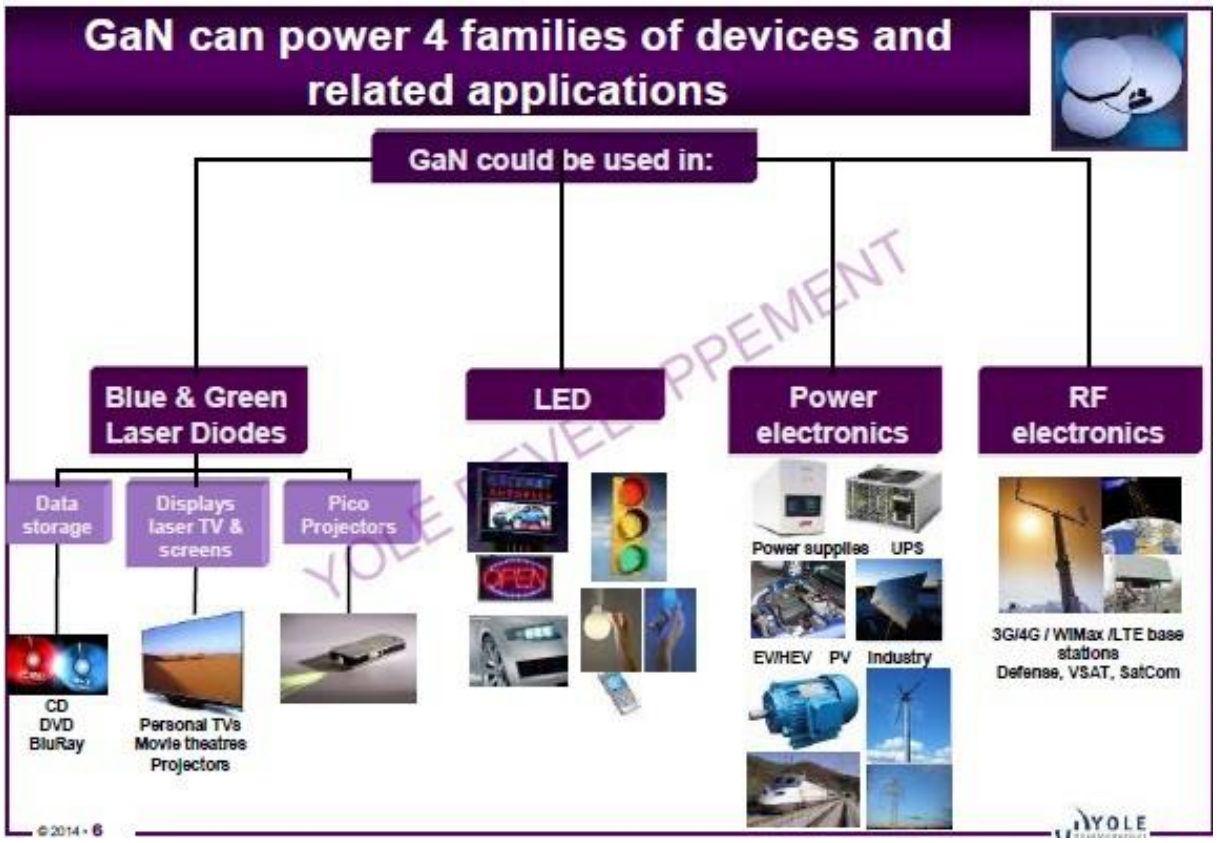


Source: Yole Développement, France.

https://pradeepchakraborty.wordpress.com/category/yole-developpement/

Figure 1.1: Some of the present and future applications for GaN devices.

Figure 1.1 shows some of the end user applications into which GaN devices are, and will be, incorporated. These can power 4 families of devices and related applications, (i) blue and green laser diodes, (ii) LEDs, (iii) power electronics and (iv) RF. Under theses 4 families come many applications such as airborne radar systems, mobile phone base stations, hybrid cars, photovoltaic inverters, lighting and energy and space applications.

### 1.1. GaN-Based HEMTs Specifications and Problems

GaN high electron mobility transistors (HEMTs) are very promising for power electronics [4-8]. Commonly GaN HEMTs are normally-on (depletion-mode) devices, i.e., and they possess a conductive channel at zero gate voltage and can only be switched off by applying a negative gate voltage. For many applications, however, normally-off (enhancement-mode) transistors, which are already off at zero gate bias and can be switched on by applying a positive gate voltage, are needed. The main problem of achieving normally-off operation is the very high polarization-induced sheet concentration of the 2DEG (two-dimensional electron gas) channel at the AlGaN/GaN interface. Normally-off operation requires that the 2DEG must be completely depleted without applying a negative gate voltage.

Several approaches for achieving normally-off GaN HEMTs have been reported in the literature. These include the use of a very thin AlGaN barriers, recessed gates, a fluoride plasma treatment of the zone underneath the gate, the piezo-neutralization technique, or hybrid MIS-HEMT structures [7, 8, 12-14]. These approaches have in common, that conventional top-gate structures are used and that normally-off operation is achieved by specific vertical designs of the layer stack underneath the gate

Although experimental normally-off devices could successfully be realized by these methods, traditionally the normally-off GaN HEMTs behaved worse compared to their normally-on counterparts. It should be noted, however, that the excellent performance of these normally-off devices are plagued with current collapse and instability problems, which greatly limit the power performance.

Beside the power-switching and RF ampflication applications, GaN-based devices may also be exploited in circuits based on a complementary design in harsh environments, such as for digital logic or for voltage amplification. Such circuits employing GaN-based devices may be used at elevated temperatures (up to 1000 ◦C [15]) or in ambients with ionising radiations not accessible to Si-based metal-oxide-semiconductor FETs (MOSFETs). For the complementary circuits, p-channel devices are necessary. However, with this device type being very new in GaN, there is

a lack of understanding about p-channel device physics. In a p-channel device, the majority carrier channel – a 2-D hole gas (2DHG) – can be formed in analogy with the 2DEG in n-channel devices by using a polarisation difference at a heterointerface. Hence, similar carrier densities can be achieved, making it very attractive to fabricate such p-channel devices.

### 1.2. Objectives of the research thesis

The two main objectives of the thesis are

(i) Achieving a significantly improved understanding of the physics and insights in the operation of the promising, but still widely unexplored, nonclassical GaN HEMT architecture e.g. superjunction GaN HEMT, PNT GaN HEMTs and GaN MIS FET.

(ii) Elaborating optimized nonclassical GaN HEMT structures by theoretical considerations and extensive device simulations.

The work will mainly be focused on normally-off nonclassical GaN HEMTs for power electronic applications. To a limited extend, however, normally-off transistors with classical structure for use in power switch applications will be investigated as well.

The current thesis will significantly go beyond the current state of the art and enhance the state of knowledge particularly in the following areas:

- Investigation of the coexistence 2DEG and 2DHG in GaN/AlGaN/GaN heterojunction.
- Investigation of the effects of certain design details that are specific for piezo-neutralization technique (PNT) HEMTs on the transistor performance, design optimization, and elaboration of favorable PNT HEMT designs that outperform conventional top-gate GaN in normally-off state.
- Theoretical investigation of a novel enhancement/depletion (E/D)-mode double channel AlGaN/GaN HEMTs logic.
- Comparison of the behaviour of double channel GaN HEMTs and GaN MISHEMTs in terms of current collapse, elaboration of the merits and drawback of both designs.
- Elaboration of differences and similarities of the classical and the nonclassical GaN HEMTs and transfer these to power devices with high voltage and seeking for concepts and feasibility studies for breakdown voltage using physically based simulation and analytical models and compare with experimental measurements.
- Detailed study of the 2DEG formation in AlScN/GaN and AlYN/GaN structures and compare the results with those obtained for conventional AlGaN/GaN structures.

**The organisation of this thesis is as the follows.**

*Chapter 2* covers the fundamental background on GaN-based HEMTs required for this work. GaN-based semiconductor material properties and merits are reviewed. The Origin of two dimensional electron gas (2DEG) and GaN-based HEMT device principal operation is enlightened. Description of operation as microwave power amplifier, as power switching device and as logic device is given. Theoretical breakdown voltage and ON-state resistance, power device theoretical limitations and premature breakdown mechanisms are discussed in details.

*Chapter 3* gives overview on GaN-based HEMTs physics-based device simulation as an engineering tool for design, analysis and evaluation of innovative concepts. Introduction to the physical-based models, structure definition and geometrical meshing is given. Empirical parameters matching and adjustment of models parameters to match the experimental device measured results are discussed.

*Chapter 4* studies the co-existence of two dimensional- electron and hole gases in GaN-based heterostructures by means of analytical models, developed in the frame of this work, and self-consistent numerical solutions of the Schrödinger and Poisson equations. The design and characterization of new vertical-design enhancement/depletion (E/D)-mode inverters or complementary in double channel AlGaN/GaN HEMTs logic is presented.

*Chapter 5* presents a comprehensive theoretical investigation of AlGaN/GaN HEMT Structures for power switch applications. Nature and origin of foxed charge at oxid/GaN interface is extracted. In addition, different design options for a normally-off MIS HEMT and simulating tunneling at Schottky contacts are discussed. Furthermore, the design of nonclassical normally-off GaN HEMTs using a piezo neutralization technique are presented.

*Chapter 6* presents gated cubic InGaN/InN heterostructures for application in InN-based high electron mobility transistors and the formation of two-dimensional electron gases (2DEGs) in lattice-matched AlScN/GaN and AlYN/GaN heterostructures, were investigated by numerical self-consistent solutions of the Schrödinger and Poisson equations. The electron concentration profiles and the resulting 2DEG sheet densities in these heterostructures are calculated and compared to those occurring at AlGaN/GaN interfaces.

# Ch a p t e r 2

# Fundamentals of GaN-based HEMT Devices and Technology

## 2.1 Introduction to Electronic Properties of Semiconductor Materials

Wide-bandgap semiconductor Gallium Nitride (GaN)-based material devices is standing in the centre of attention this thesis. Owing to the unique properties of GaN such as wide bandgap and good electron transport properties, GaN HEMTs are very promising for power electronic applications. These properties compared to Si are [17,18,19]:

- Large band gap (3.4 eV compared to 1.1 eV for Si, a bandgap three times or more)
- High critical field (around $3.3x10^6$ V/cm compared to $0.3\ x10^6$ V/cm for Si)
- High electron mobility and saturation velocity (700 - 2000 $cm^2$/V.s and $2.5x\ 10^7$cm/s compared to 1350 $cm^2$/V.s and $1.0x10^7$cm/s for Si, respectively).

These properties mean that GaN based devices offer the following potential benefits compared to Si, see Figure 2.1.:

1. Higher breakdown voltage, ten times higher than that of Si. The critical field for GaN is around $3x10^6$ V/cm meaning that for electrodes on GaN with a spacing of 1μm, then theoretically a bias voltage of just above 300 V could be applied without material breakdown. However, no GaN transistor (HEMT) to date has managed to reach this theoretical performance.
2. Lower on-state resistance, good or better than that of Si. AlGaN/GaN high electron mobility transistors (HEMTs) display on resistances of < 1mΩ$cm^2$ compared to > 100mΩ$cm^2$ for Si leading to much lower on-state power loses, improving the efficiency of the device, in switching applications for instance.
3. Faster switching frequencies resulting in circuits using GaN HEMTs requiring smaller capacitors and inductors and so reducing overall size.
4. Higher temperature capabilities. Devices have been shown to work beyond 300°C, leading to much reduced need for large heat sinks and cooling systems.

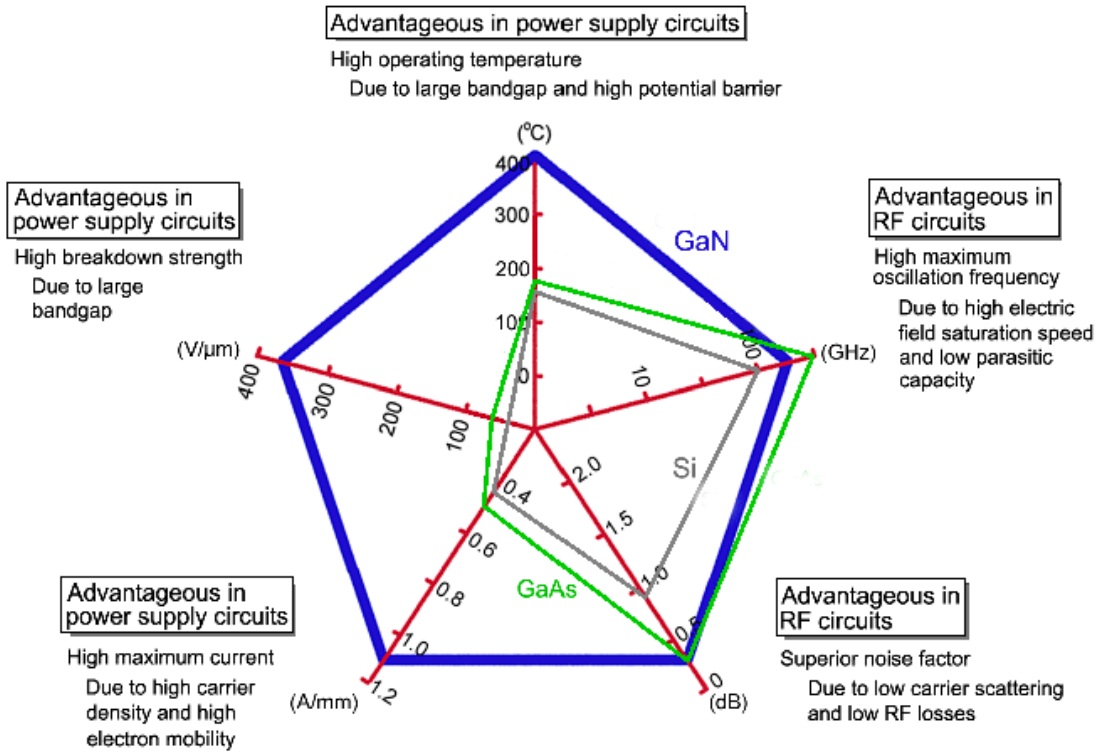


**Figure 2.1** GaN material merits compared to Si and GaAs [16].

Table 2.1 compares various semiconductor materials which have been used for power electronics and ones which are still currently undergoing research for future power electronic applications and includes the following: $E_g$ - the material's band gap; $\mu_n$ - the electron mobility in the semiconductor; $v_{sat}$ - the electron saturation velocity; $E_C$ - the critical breakdown field.

| **Property** | **Si** | **GaAs** | **4H-SiC** | **GaN** | **Diamond** |
|---|---|---|---|---|---|
| $E_g$(eV) | 1.1 | 1.4 | 3.3 | 3.4 | 5.5 |
| $\mu_n$(cm$^2$/V.s) | 1350 | 8500 | 700 | 700(Bulk) 2000(2DEG) | 1900 |
| $v_{sat}$($10^7$cm/s) | 1.0 | 1.0 | 2.0 | 2.5 | 2.7 |
| $E_C$(MV/cm) | 0.3 | 0.4 | 3.0 | 3.3 | 5.6 |
| *JFoM* ($E_C.v_{sat}/2\pi$) | 1 | 7.1 | 180 | 760 | 2540 |
| *BFoM* ($\varepsilon\ \mu_n\ E_C^3$) | 1 | 15.6 | 130 | 650 | 4110 |
| *BHFFoM* ($\mu_n\ E_C^2$) | 1 | 10.8 | 22.9 | 77.8 | 470 |
| *KFoM* $\kappa(v_{sat}/\varepsilon)^{1/2}$ | 1 | 0.45 | 4.61 | 1.6 | 32.1 |

**Table 2.1:** Comparison of different semiconductors commonly used for high frequency and high power electronic applications. [17].

To make a fair comparison of these materials, a figure of merit (FOM) in Table 2.1 can be assigned to them which brings together some of the properties which make them so useful for high power and high frequency applications. The four figures of merit that are highly regarded in the power electronics sector and have been used frequently over the years to make comparisons between semiconductor materials are the Johnson Figure of Merit (JFoM) [20], the Baliga Figure of Merit (BFoM) [21] for low frequency operation, the Baliga Figure of Merit for high frequency operation (BHFFoM) [22] and the Keyes Figure of Merit (KFoM) [23]. The JFoM takes into account the breakdown voltage and the saturated electron drift velocity of the material and is 760 times higher for GaN than it is for Si, the higher number indicating its superiority. The Baliga FOMs are based on the relative permittivity, electron mobility, and breakdown field. These FOMs are a measure of the power handling capabilities of the material and again are far superior to Si being 650 (BFOM) and 77.8 (BHFFoM) times higher. The KFoM provides a thermal limitation to the switching behaviour of transistors and is 1.6 times higher for GaN.

These numbers have been provided just to show how GaN compares relatively to Si. As can be seen from Table 2.1 the FOM numbers for diamond are higher than those of GaN, however, diamond is still at very early stages of research and will require a great deal more time and investment to be competitive with the state-of-the-art GaN devices.

### 2.1.1. Material Structure and Polarization Wurtzite GaN-Based Semiconductors

III-N based semiconductors especially GaN-based crystallize in different structures, wurtzite hexagonal close packed (HCP) (α-phase), cubic zinkblende (β-phase) and Rock-salt [24], [25].

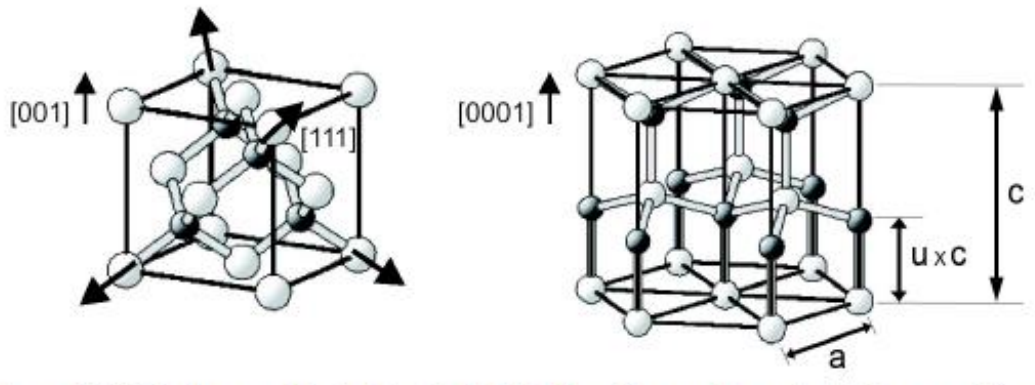


**Figure 2.2:** III-Nitrides crystallize in cubic zinc-blende (left) and hexagonal wurtzite (right) structure. They both lack the centre of symmetry, so they show piezoelectricity. The wurtzite, which is a lower symmetry crystal, possesses also the spontaneous polarization. The lattice parameters *a*, *c* and *u* are shown for the wurtzite structure. The arrows on the zinc-blende structure depict the set of <111> directions. Adapted from [26].

Today, the wurtzite crystal structure, depicted in Fig. 2.2(right), is of main interest for electronic and optoelectronic applications. The wurtzite structure has a hexagonal unit cell and consists of two intercepting Hexagonal Closed Packed (HCP) sub-lattice. Hence it is defined by two lattice parameters, the length of a side of the hexagonal base $a_0$ and the height of the cell $c_0$, in ideal ratio $c_0/a_0 = \sqrt{8/3} \approx 1.633$, as shown in Figure 2.1–2. Each sub-lattice is constituted by one type of atoms which are shifted with respect to each other along the c axis by the internal cell parameter $u_0 = 3/8$. The structural and polarization parameters of III-Ns are reported in Table 2.2.

| **Parameter** | **GaN** | **AlN** | **InN** |
|---|---|---|---|
| $\boldsymbol{a_0(A^\circ)}$ | 3.197 | 3.108 | 3.580 |
| $\boldsymbol{c_0/a_0}$ | 1.6297 | 1.6033 | 1.6180 |
| $\boldsymbol{\epsilon_1 = (u_0 - u_{ideal}) \times 10^{-3}}$ | 1.9 | 6.4 | 3.7 |

Reference [27]

**Table 2.2**: Structural and polarization parameters of III-N wurtzite semiconductors

Common nitride compounds AlN, GaN, and InN and their related alloys do not show these ideal values. As the lattice non-ideality increases, $c_0/a_0$ ratio moves away from 1.633 of the ideal lattice [28]. Owing to the extremely high electronegativity (here given in Pauling's scale) of N atom , which is 3.04 and only for Gallium (1.81), Aluminum (1.61) and/or Indium (1.78) atoms [28]. This results in values for $c_0/a_0$ and $u_0$ deviating from the aforementioned ideal ones [10]. Due to this electronic charge redistribution inherent to the crystal structure the group III-N semiconductors exhibit exceptionally strong polarization. This polarization refers to spontaneous polarization, $P_{sp}$, [28]. Because the wurtzite structure lacks inversion symmetry along its c-axis (called the pyroelectric axis), the directions <0001> and <000$\overline{1}$> are not equivalent. Thus, GaN shows two possible polarities, in cation-face, i.e. Ga-face, the polarization field points away from the surface to the substrate, while in anion-face, i.e. N-face, the direction of the polarization field is inverted.

Due to this lack of inversion symmetry, when stress is applied along the <0001> direction to the group III-N semiconductors' lattice, the ideal lattice parameters $c_0$ and $a_0$ of the crystal structure will change to accommodate the stress. Therefore, the polarization strength will be changed. This additional polarization in strained group III-N crystals is called piezoelectric polarization, $P_{pz}$ [22]. For example, if the nitride crystal is under biaxial compressive stress, the

in-plane lattice constant $a_0$ will decrease and the vertical lattice constant $c_0$ will increase. Hence, the $c_0/a_0$ ratio will increase towards 1.633 of the ideal lattice and the total polarization strength of the crystal will decrease because the piezoelectric and spontaneous polarizations will act in the opposite directions. It is clear that if tensile stress is applied to the crystal, the total polarization will increase because the piezoelectric and spontaneous polarizations in that case act in the same direction. The piezoelectric polarization, $P_{pz}$, is simply expressed via the piezoelectric coefficients $e_{33}$ and $e_{13}$ as:

$$P_{pz} = e_{33}\varepsilon_3 + e_{13}(\varepsilon_1 + \varepsilon_2) \qquad 2\text{-}1$$

where $a_0$ and $c_0$ are the equilibrium values of the lattice parameters, $\varepsilon_3 = (c - c_0)/c_0$ is the strain along the c axis, and the in-plane strain $\varepsilon_1 = \varepsilon_2 = (a - a_0)/a_0$ is assumed to be isotropic.

The different strains in the lattice are related as in:

$$\varepsilon_3 = -2.\frac{C_{13}}{C_{33}}.\varepsilon_1 \qquad 2\text{-}2$$

where $C_{13}$ and $C_{33}$ are elastic constants. Eq. 2–1 and Eq. 2–2 can be combined to obtain the following equation:

$$P_{pz} = 2.\frac{a-a_0}{a_0}\left[e_{13} - e_{33}\frac{C_{13}}{C_{33}}\right] \qquad 2\text{-}3$$

Since in the wurtzite III-nitrides the piezoelectric coefficient $e_{13}$ is always negative while $e_{33}$, $C_{13}$, and $C_{33}$ are always positive, it turns out that $(e_{13} - e_{33}\frac{C_{13}}{C_{33}})$ will always be negative [20,22]. As a consequence, the value of piezoelectric polarization ($P_{pz}$) in group III-N is always negative for layers under tensile stress ($a > a_0$) and positive for layers under compressive stress ($a < a_0$). As spontaneous polarization in group III-nitrides is always negative, it can be concluded that for layers under tensile stress, spontaneous and piezoelectric polarizations are parallel to each other, and for layers under compressive stress the two polarizations are anti-parallel.

Polarization itself and gradients in polarization at interfaces and surfaces of AlGaN/GaN heterostructures induce fixed sheet charges, which in turn cause strong electric fields inside heterostructure. In the nitrides the electric field can reach strength of $3 \times 10^6$ V/cm and therefore enhance electron or hole accumulation (depending on the polarity of the material) at AlGaN/GaN interfaces. This accumulation is known as polarization induced doping that is the source of the Two-Dimensional Electrons Gas (2DEG) that will be discussed in the followin.

### 2.1.2. $Al_xGa_{1-x}N$/GaN Heterostructures and 2DEG Formation

The unique feature of the HEMT is usually referred to as a Two-Dimensional Electrons Gas (2DEG) (or a Two-Dimensional Holes Gas (2DHG)) with its high density and high mobility. This 2DEG (or 2DHG) forms a channel from electrons (holes) accumulated along a heterojunction in a quantum well [29]. The term 2DEG refers to the condition in which electrons have quantized energy levels in one spatial direction but are free to move in the other two directions, parallel to the interface, and thus enhance in mobility. Enhanced electron mobility is the key feature that differentiates HEMTs from another FETs.

In early generation AlGaAs/GaAs-based HEMTs the origin of the carrier was a junction between a heavily doped high bandgap and a lightly doped low bandgap region. In GaN-HEMTs based structures such as $Al_xGa_{1-x}N$/GaN heterostructure, this carrier accumulation is mainly due to the bound sheet charge that appears in the AlGaN at the interface due to discontinuity in the polarization.

In general, if the polarization field ($\vec{P}$) changes in space, there will be a bound charge density ($\rho$) associated with it which is given by:

$$\rho = -\vec{\nabla}.\vec{P} \qquad 2\text{-}4$$

For wurtzite III-nitrides polarization is always directed along the c-axis, perpendicular to the

heterostructure interface. Hence, at the $Al_xGa_{1-x}N$/GaN heterojunction, which is assumed to be planar and abrupt a bound sheet charge (σ) will be formed that is given by [9]:

$$\sigma = \vec{P}_{(AlGaN)} - \vec{P}_{(GaN)}$$

$$= \left(\vec{P}_{sp(AlGaN)} + \vec{P}_{pz(AlGaN)}\right) - \left(\vec{P}_{sp(GaN)} + \vec{P}_{pz(GaN)}\right) \qquad 2\text{-}5$$

This bound charge, which is induced by a change in polarization of the two layers, will attract compensating mobile charge at the interface. If the bound charge is positive as for Ga-face GaN it will cause a negative mobile sheet charge.

To calculate the amount of polarization induced sheet charge density at the interface between AlxGa1-xN and GaN, material parameters for $Al_xGa_{1-x}N$ alloys can be calculated from the known Al mole fraction values of $0 \geq x \geq 1$ [10], [30].

The piezoelectric polarization for GaN $\vec{P}_{pz(GaN)}$ is assumed to be zero since bulk GaN buffer layers are assumed none-strained and thus strain-free. Since $Al_xGa_{1-x}N$ grown on Ga-face GaN is always under tensile strain, both piezoelectric and spontaneous polarizations have the same sign and add up.

The high positive polarization induced sheet charge density, formed at $Al_xGa_{1-xN}$/GaN interface for Ga-face layers, can be compensated by free electrons to form a two-dimensional electron gas (2DEG). It is not clear where the electrons come from: they can be attracted from the bulk GaN buffer layer or from donor-like surface states [31], or from carrier injection from the metal contacts [9]. The maximum sheet carrier concentration for GaN buffers thicker than 1 μm can be expressed as [9], [10]:

$$n_S(x,d) = \frac{+\sigma}{e} - \frac{\varepsilon_0 \varepsilon(x)}{de^2}[e\Phi_b(x) + \Delta(x) - \Delta E_C(x)] \qquad 2\text{-}6$$

Where: $\varepsilon_0$ is the dielectric constant of vacuum, ε is the relative dielectric constant of the barrier layer, d the thickness of the $Al_xGa_{1-x}N$ layer, $e\Phi_b(x)$ the Schottky barrier height of the gate contact on top of the AlxGa1-xN layer, $\Delta$(x) the position of the conduction band below the Fermi-level at the interface, and $\Delta E_C$(x) the conduction band offset at the interface. $\Delta(x)$ is calculated using the expression (see Figure 2.3).

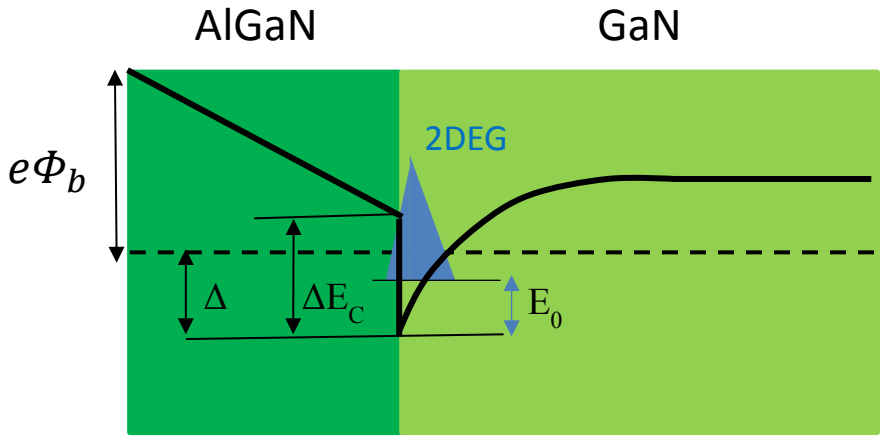


**Figure. 2.3.** Vertical cross-section of the conduction band in the heterostructure. The dashed line is the position of the Fermi level in the semiconductor. *Φb* is a barrier height. In the case of a heterostructure or a HEMT far from the gate the barrier height is determined by the surface sheet charge. Under the gate of a HEMT, it is determined by the Schottky barrier, modified by the applied gate voltage. Δ is the penetration of the conduction band edge below the Fermi level at the AlGaN/GaN interface, *ΔEC* is the conduction band offset, *E0*, is the lowest subband level of the 2DEG. The labels correspond to the ones used in equations (2.17) and (2.18). Adapted from [33].

$$\Delta(x) = \left(\frac{9\pi\hbar e^2 n_S(x,d)}{8\varepsilon_0\sqrt{8m^*\varepsilon(x)}}\right)^{2/3} + \frac{\pi\hbar^2}{m^*} n_S(x,d) \qquad 2\text{-}7$$

where the first term, in the Figure 2.3 labelled as $E_0$, is the lowest subband level of the 2DEG with the effective electron mass $m^* \approx 0.228$ me [32]. It follows from the equations (2.6) and (2.7) that the formula to calculate electron sheet density ns is itself dependent on ns, thus the calculation cannot be solved analytically.

### 2.1.3. Carrier Mobility in $Al_xGa_{1-x}N$/GaN heterostructures, 2DEG

Reducing the dimensionality of an electrically conducting system is known to have a dramatic effect on the nature of the observable physical phenomena. In the case of two-dimensional systems, where charge carriers are free to move in the x− y directions but confined spatially in the z, a vast array of ground states and non-equilibrium effects have been revealed, concomitant to improvements in material quality. A figure often used to gauge such quality is the carrier mobility ($\mu$) and the longitudinal conductivity is given by [34]:

$$\sigma = q.n_S.\mu \qquad 2\text{-}8$$

where q is the electron charge, $\sigma$ is a function of the sheet carrier (electrons) concentration ($n_S$) and μ is the mobility.

The carriers are accelerated by the presence of an electric field and achieve an average velocity determined by the carrier scattering processes. As the free carriers are transported along the direction of the electric field, their velocity increases until they experience scattering. In the bulk semiconductor, the scattering can occur either by interaction with the lattice or at ionized donor and acceptor atoms. Consequently, the mobility is dependent upon the lattice temperature and the ionized impurity concentration. The low field mobility (μ) is defined as the proportionality constant relating the average carrier velocity ($v_D$) to the electric field (E):

$$v_D = \mu.E \qquad 2\text{-}9$$

This expression is valid at low electric fields. However, at high electric fields the velocity is no longer found to increase in proportion to the electric field. In fact, the velocity approaches a constant value known as the saturated drift velocity. (See section 2.1.4 below)

As the carriers travel through a semiconductor, they undergo a variety of interactions with the host material. The electron mobility is the most popular and most important transport parameter

used to characterize the microscopic quality of the semiconductor layers. Mobility is considered to be the figure of merit for materials used for electronic devices.

In addition to the high carrier concentration in the 2DEG created by the polarization induced doping at the AlGaN/GaN interface; carriers in the 2DEG have unique high mobility properties. GaN-based semiconductors' large bandgap, large dielectric breakdown field, good electron transport properties (an electron mobility possibly in excess of 2000 $cm^2.V^{-1}.s^{-1}$ and a predicted peak velocity of $2.5 \times 10^7$ $cm.s^{-1}$ at room temperature), and good thermal conductivity are merits for high-power/temperature electronic devices.

Electron mobility is a key parameter in the operation of GaN-based HEMT as it affects the access resistances as well as the rate with which the carrier velocity increases with electric field. Consequently, the low-field mobility in GaN is depending on various scattering events.

The electron mobility is limited by the interaction of electrons with phonons and, in particular, with optical phonons. This holds for bulk mobility as well as that in AlGaN/GaN HEMTs' 2DEG.

Khan et al. showed in their early work, illustrated in Figure 2.4, that the mobility for the single GaN layer increases from 450 $cm^2$ $V^{-1}$ $s^{-1}$ at room temperature to 1200 $cm^2$ $V^{-1}$ $s^{-1}$ at 150 K. It then decreases for lower temperatures due to ionized impurity scattering. On the other hand, the electron mobilities of the heterojunction increases from 1500 $cm^2$ $V^{-1}$ $s^{-1}$ at room temperature to a value of 5000 $cm^2$ $V^{-1}$ $s^{-1}$ at 150 K and remains essentially constant for temperatures down to 80 K. This enhanced electron mobility is associated to the presence of 2DEG at the hetero-interfaces. The 2DEG mobility enhancement is caused by a much higher volume electron concentration (compared to the bulk n-GaN), which results in a larger Fermi energy and a more effective screening [34], [35].

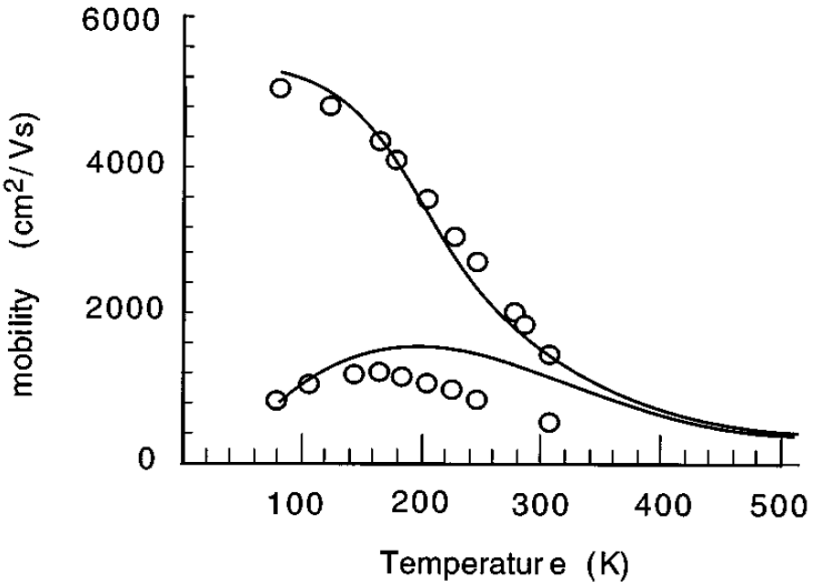


**Figure 2.4** Experimental (dots) and calculated (lines) electron Hall mobility in GaN vs. temperature for $Al_{0.1}Ga_{0.9}N$/GaN two dimensional electron gas (2DEG) (upper curve) and bulk *n*-GaN $n = 1 \times 10^{17}$ $cm^{-3}$(lower curve) [33].

The 'traditional' scattering mechanisms in 2DEG and their effects on the carrier mobility have been studied for AlGaAs/GaAs and Si-MOSFET systems. They are important in AlGaN/GaN 2DEG transport as well. Electrons moving in the 2DEG experience interface-roughness scattering due to the non-abrupt interface between AlGaN and GaN. The 2DEG wave-function is mostly confined in GaN, but there is a finite part that penetrates the AlGaN barrier, leading to alloy-disorder scattering. Interface-roughness scattering and alloy scattering are short-range scattering sources [36]. Charged impurities are always present in the semiconductors samples, and constitute a form of long-range Coulombic scattering source.

The lattice vibrates at finite temperatures and phonons form a potent scattering mechanism at high temperatures. An important form of Coulombic scattering in AlGaN/GaN 2DEGs is dislocation scattering, owing to the large density of dislocations in the material. The cores of threading edge dislocations have dangling bonds that introduce states in the gap of the semiconductor, causing a dislocation to become a line of charge. Such charged dislocations scatter conduction electrons. Dislocations also scatter from strain-fields that develop around them.

Due to the very high electric fields that result from the large polarization ($\backsim$ 1 MV/cm), electrons in the 2DEG are electro-statically pushed close to the AlGaN/GaN interface, and the

centroid of the wave function is brought closer to the hetero-interface. This directly leads to an increased sensitivity to alloy disorder and interface roughness scattering, which turn out to be the dominant scattering processes at low temperatures, and even at room temperature for very high density 2DEGs. In addition to the microscopic disorder in an alloy layer, the dipole moment in each unit cell is no more periodic with the crystal lattice; therefore it leads to 'dipole-scattering'. This interesting novel scattering mechanism has no analogue in traditional non-polar and weakly-polar semiconductors.

For the design of GaN-based HEMTs structures with high conductivity the following should be taken into consideration [37]. The mobility of low-density AlGaN/GaN 2DEGs ($n_{2DEG} \leq 10^{12}$ $cm^{-2}$) is limited by scattering from charged defects such as dislocations, dipoles, residual impurities. Mobility of high-density AlGaN/GaN 2DEGs is insensitive to scattering by various charged impurities. Alloy disorder scattering limits the mobility for AlGaN/GaN 2DEGs at low temperatures. At extremely high carrier densities, alloy scattering is as severe as scattering from phonons, even at room temperature.

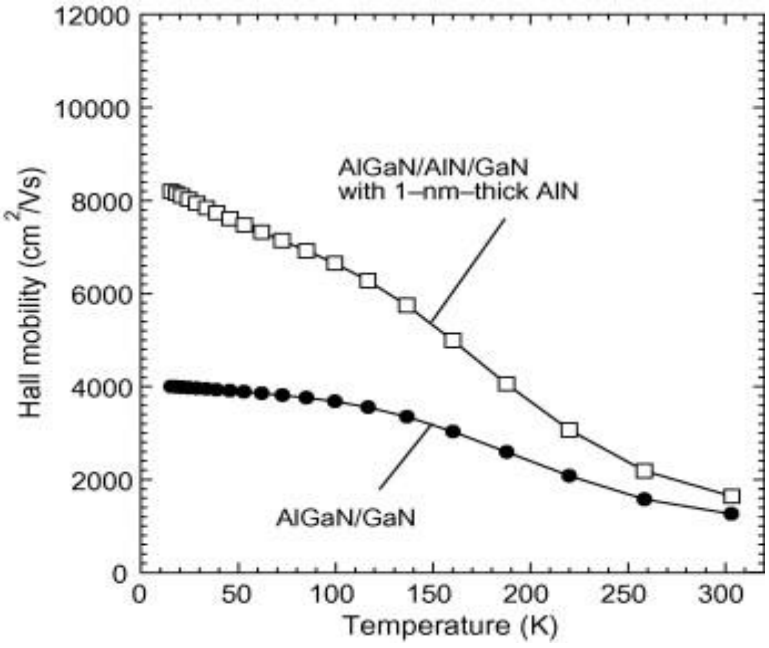


**Figure 2.5.** Temperature dependence of electron Hall mobility for AlGaN/GaN and AlGaN/AlN/GaN wafers [39].

An additional enhancement of the mobility can be achieved by the insertion of 1-nm-thick AlN interfacial layer. Figure 2.5 shows the temperature dependence of the hall mobilities for the AlGaN/AlN/GaN structure with the 1-nm-thick AlN. From this figure, it is clear that the saturation of hall motilities al low temperatures, in which the alloy disorder and/or interface roughness are the dominant scattering processes [38], is markedly reduced in the case of the AlGaN/AlN/GaN structure compared with that in the case of the AlGaN/GaN structure. For

example, a structure with an AlN layer thickness of 1.0 nm showed a highly enhanced Hall mobility ($\mu_{Hall}$) of 1770 $cm^2/Vs$ (7260 $cm^2/Vs$) with a low sheet resistance ($\rho_s$) of 365 Ω/sq (87 Ω/sq) and $n_s = 1.0 \times 10^{13}/cm^2$ at room temperature (at 77K) compared with those of a sample without the AlN interfacial layer ($\mu_{Hall}$ = 1287 $cm^2/Vs$ (3998 $cm^2/Vs$), $\rho_s$ = 539 Ω/sq (174 Ω/sq), and $n_s = 0.9 \times 10^{13}/cm^2$).

### 2.1.4. Carrier Velocity in GaN-Based Material Systems

The steady-state electron drift velocity versus electric field has been calculated for the nitride binaries and ternaries at different temperatures and for various doping concentrations [40]. As expected, Monte Carlo simulations [41], [42] confirm that electron velocity of GaN depends on doping concentration, electric field, and temperature. The variation of electron velocity with electric field always shows a peak.

Figure 2.6 shows the calculated electron steady-state drift velocity versus applied electric field, for GaN, $Al_{0.2}Ga_{0.8}N$, $Al_{0.5}Ga_{0.5}N$, $Al_{0.8}Ga_{0.2}N$ and AlN materials [40].

The velocity-field characteristics can be described by (i) Ohmic in low field region; (ii) Nonlinear transport characterized by a hump in the velocity-field curve at fields of ∽ 10 to 50 kV/cm; (iii) peak velocity region occurring at ∽ $2 \times 10^5$ V/cm; (iv) negative resistance region followed by and (v) saturation and until breakdown.

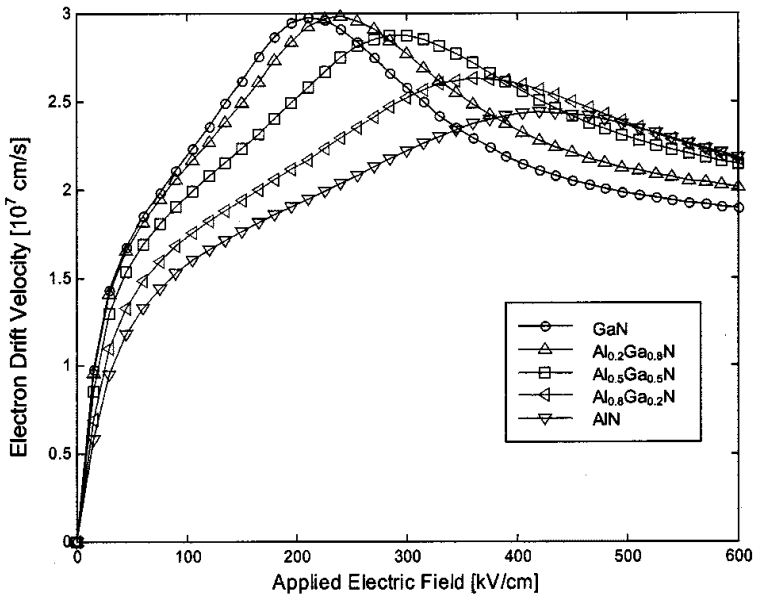


**Figure 2.6.** Monte Carlo simulations of electron drift velocity versus applied electric field for GaN, $Al_{0.2}Ga_{0.8}N$, $Al_{0.5}Ga_{0.5}N$, $Al_{0.8}Ga_{0.2}N$, and AlN. Lattice temperature is at 300K, and electron concentration is equal to $10^{17}cm^{-3}$ (Results are taken from [40]).

The obtained velocity-field characteristics for GaN-based semiconductors suggest a rather high electron peak and saturation velocity together with high field. The combination of high-field and high electron velocity in GaN-based semiconductors confirms the potential to increase of output power densities, since high current densities and high voltages would be achieved at the same time. More theory on GaN-based semiconductors transport is discussed in section 3.3.2.2 below.

Velocity–field curves have also been calculated for a temperature range of 77–1000 K [43]. The variation of electron velocity with electric field as a function of the temperature is shown in Figure 2.7. Calculated temperature dependence of electron mobility in GaN quantum wells was found to be higher than in the bulk GaN material, which is counterintuitive as carrier scattering into the barrier where the mass is higher and velocity is lower would lower the velocity instead. Unfortunately, many GaN parameters necessary for Monte Carlo calculations are not yet precisely known. In view of this uncertainty, it may be unwise to draw any definitive conclusion regarding the calculated effect of compensation on the electron mobility.

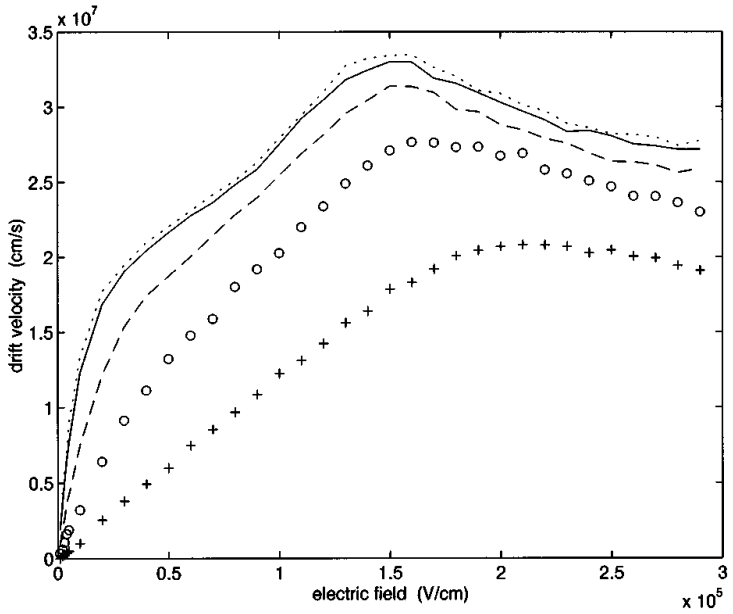


**Figure 2.7.** Monte Carlo simulations of temperature dependence of velocity field characteristics of GaN, $n = 10^{17}$ $cm^{-3}$. Dotted line, $T$=77 K; line, $T$=150 K; dashed line, $T$ =300 K; circles, $T$=500 K; plusses, $T$=1000 K. [43].

## 2.2. AlGaN/GaN-Based HEMTs

The main feature of GaN-based power and high-frequency devices is the two-dimensional electron gas, 2DEG, at the AlGaN/GaN heterojunction. The first report on the fabrication and operation of AlGaN/GaN heterojunction FETs, also called HEMTs, was by Khan et al. in 1993 [2].

Figure 2.8 shows the schematic view of an AlGaN/GaN HEMT and the energy band diagram under the gate electrode (principle of operation), respectively. A high carrier density is generated at the AlGaN/GaN hetero-interface due to spontaneous and piezoelectric polarization effects (section 2.1.2 above). The combination of the large carrier density and high breakdown voltage enables high power output operation.

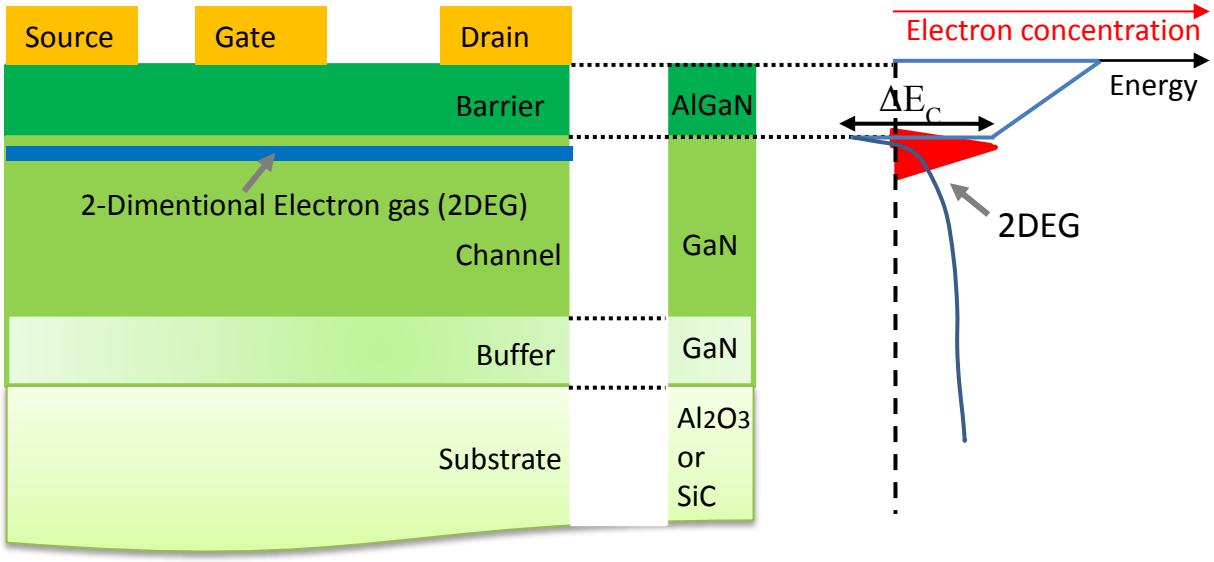


**Figure 2.8.** A schematic AlGaN/GaN based HEMT structure. The figure is not to scale. In a real transistor, the length of the device is much larger than the thickness of the AlGaN barrier. The 2-dimensional electron gas (2DEG) is in the potential well in the GaN layer, which is the lower band-gap semiconductor in this heterostructure, near the heterostructure interface. The 2DEG creates the channel, which leads current in the device. The current flows between the ohmic contacts, the source and the drain, and is controlled by the voltage applied at the gate, which is a Schottky contact.

A GaN-based HEMT transistor is a three terminal device in which the current flowing between the source and the drain ohmic contacts is modulated by the Schottky metal gate contact. The gate is shifted away from the drain to reduce this field and hence increase the breakdown voltage of the device. However, increasing the distance between the gate and drain has a negative impact on the performance of high frequency devices, especially reducing the current gain cut-

off frequency ($f_T$) (section 2.2.2 below). The majority carriers, electrons, are traveling through the highly conductive 2DEG channel formed at the AlGaN/GaN interface and their number is modulated by the electric field resulting from the gate bias. The contribution of $V_G$ will therefore transform the expression for the electron sheet density, given in equation (2.8), to

$$n_S(x,d) = \frac{+\sigma}{e} - \frac{\varepsilon_0 \varepsilon(x)}{de^2}[e(\Phi_b(x) - V_G) + \Delta(x) - \Delta E_C(x)] \qquad 2\text{-}10$$

The conducting channel (under the heterointerface, between the source and drain terminals) can be viewed as a resistance. For small drain-source voltage $V_D$, the drain current $I_D$ is approximately linear. When a negative voltage is applied to the gate, the electrons are partially depleted from the channel and its resistance increases. As the negative gate voltage $V_G$ is increased, a threshold voltage $V_{Th}$ is reached. At the threshold, the channel is closed, i.e., completely depleted of electrons, and the $I_D$ drops to zero. This condition is called *pinch-off*. Such transistor is usually working in a depletion mode, i.e. at $V_{GS}$ = 0 V gate conditions the device is normally in its "ON" state allowing current to flow through it. Such characteristics are big problem for switching applications for safe operation reasons. High current levels in the device may occur unintentionally when gate control is lost. Therefore, reliable normally-OFF devices are needed.

### 2.2.1. AlGaN/GaN HEMTs as Microwave Transistors

GaN-based HEMTs were first considered for microwave applications due to their superior properties. It is important to understand the behavior of devices at higher frequencies both in small and large signal operation. A good power device is that which allows to switch as large current as possible, on and off across as large a load resistance as possible, to obtain the maximum output power across this load resistance. In GaN-based HEMTs due to the large values of the access resistances (the series resistance between the gate electrode edge and the source/drain electrode edge), the maximum drain current is not velocity limited but mobility limited hence the $n_s \cdot \mu$ combination in microwave transistors is more important than the $n_s \cdot v_{sat}$ combination. The 2DEG channel provides the high carrier density and high carrier mobility as a consequence of the strong polarization field present in the GaN system.

Schematic DC I-V characteristics of GaN-based HEMT are illustrated in Figure 2.9. In such devices both high current densities and high drain voltage are available and explain the large power capacity. The maximum output current $I_{DS\,max}$, the knee voltage $V_{knee}$ and the breakdown voltage $V_{BR\,OFF}$ can be measured to estimate the maximum output power in class-A operation.

$$P_{max} = \frac{I_{DS\,max}(V_{BR\,OFF} - V_{knee})}{8} \qquad 2\text{-}11$$

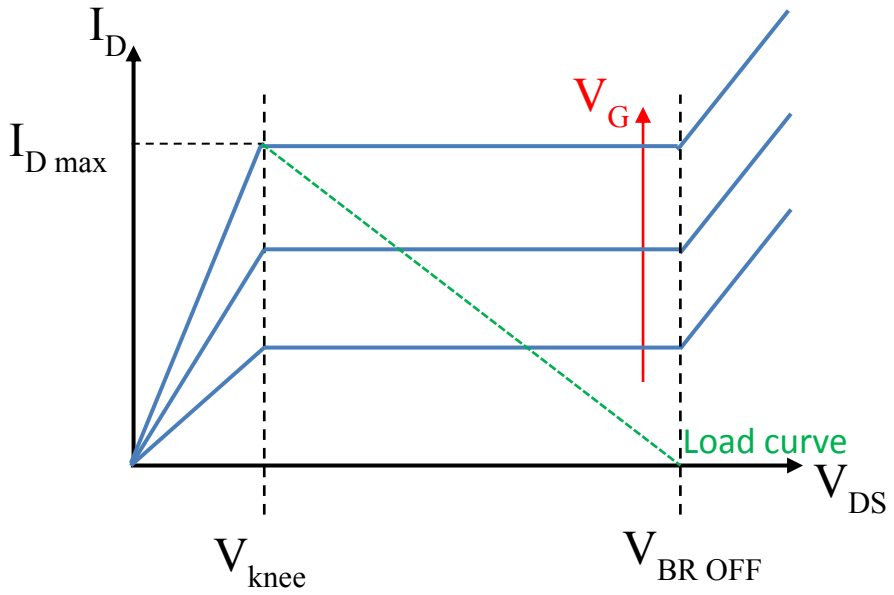


**Figure 2.9.** Illustration of operation points on I-V curves of microwave class-A power amplifier.

Threshold voltage, $V_{Th}$, is the gate-source voltage necessary to stop the current in the device by totally depleting the 2DEG channel from mobile carriers.

$$V_{Th} = V_{GS}\Big|_{\substack{I_{DS}\to 0 \\ V_{DS}>V_{GS}}} \qquad 2\text{-}12$$

The ability of the gate to modulate the current flow between the source and the drain is expressed by the transconductance, $g_m$, defined as:

$$g_m = \frac{\partial I_D}{\partial V_{GS}}\Big|_{V_{DS}=const.} \qquad 2\text{-}13$$

Additional figure of merits are commonly used to characterize the microwave power HEMTs in terms of high frequency performance [44]; the current-gain cut-off frequency, $f_T$, and the maximum frequency of oscillation $f_{max}$ and just describe the small signal behaviour of the device. These parameters could be extracted from small signal measurements (S-parameters). The cut-off frequency, $f_T$, value is extracted from the $|h_{21}|^2$ parameter-curve where it equals gain of 0 dB. The maximum frequency of oscillation, $f_{max}$, value is extracted from the maximum unilateral transducer-power gain, MUG, and maximum stable gain, MSG, parameters curves where it reaches gain of 0 dB.

Thermal management is important in a microwave device in order to reach a maximal output power. Self-heating effect that elevates the channel temperature reduces the low-field carrier mobility and their saturation velocity. The available drain current decreases at high drain voltage, thus the output power density is reduced.

### 2.2.2. AlGaN/GaN HEMTs as Power Switching Transistors

Silicon has long been the dominant semiconductor for high voltage power switching devices, most commonly making use of structures like the double-diffused metal-oxide-semiconductor (DMOS), UMOS etc, [45]. However, silicon power devices are rapidly approaching theoretical limits for performance (see section 2.4.2 below). There have been successful efforts to push beyond limits of Si by novel device structures like the Super Junction MOSFET [46], [47], CoolMOSTM [48] and RESERF MOSFET [49].

At the same time, wide bandgap materials, particularly GaN and SiC, have attracted much attention because they offer a number of potential advantages over silicon. These potential advantages arise from the fundamental physical properties of the material. GaN-based High Electron Mobility Transistors (HEMTs) are considered to be excellent candidates for high-power switching applications such as highly efficient power switches in switched power-supplies or AC motor-drive systems, due to their high electron mobility ($\mu \sim 1500\ cm^2\ V^{-1}\ s^{-1}$), high saturation velocity and high sheet-carrier density ($n_s \sim 10^{13}\ cm^{-2}$) in the two dimensional electron gas (2DEG) channel. These in turn yield a high $ns \cdot \mu$ product which contributes to a low ON-state resistance, $R_{ON}$. The high critical electric field-strength (~ 3.5 MV/cm) allows high natural OFF-state blocking capability in smaller device regions thereby also reducing the $R_{ON}$ [50], [51], [52]. The polarization induced doping results in low electron scattering. In addition to their good thermal limitation the wide bandgap is suitable for high temperature operation up to 400 °C. In GaN-based HEMTs' structures the operating temperature is only limited by the extrinsic materials like the SiNx passivation layer, Schottky metal stability etc.

An important limitation called the power-frequency ($pf^2$) [54] limit relates to the inherent limit on the breakdown voltage a high frequency device technology can achieve. This limits the output power one can obtain from a given device technology. The $pf^2$ limit, well-known in microwave power transistor design, imposes particularly severe performance limits on broadband microwave power amplifiers.

In high frequency transistors HEMT, there is a high-field drift region separating the control region or the channel from the output terminal. If the length of this region is $D_{drift}$, and the semiconductor breakdown electric field is $E_{max}$, then the transistor breakdown voltage is,

$$V_{br} = E_{max} D_{drift} \qquad 2\text{-}19$$

This drift layer introduces space-charge transit time, $\tau_{sct}$. If the electron velocity is $v_{sat}$, then the space charge transit time

$$\tau_{sct} = D_{drift}/2v_{sat} \qquad 2\text{-}20$$

and (ignoring all other transit delays) the unity current-gain cutoff frequency is

$$f_T \leq v_{sat}/\pi D_{drift} \qquad 2\text{-}21$$

Combining equation 2.19 and equation 2.21, we get

$$f_T V_{br} \leq E_{max} v_{sat}/\pi \qquad 2\text{-}22$$

which is purely dependent on the material parameters. So, the transistor $f_T$ and $V_{br}$ have to be traded against each other, with extended drift regions giving high breakdown voltages but low $f_T$ and thin drift regions giving low breakdown voltages but high $f_T$.

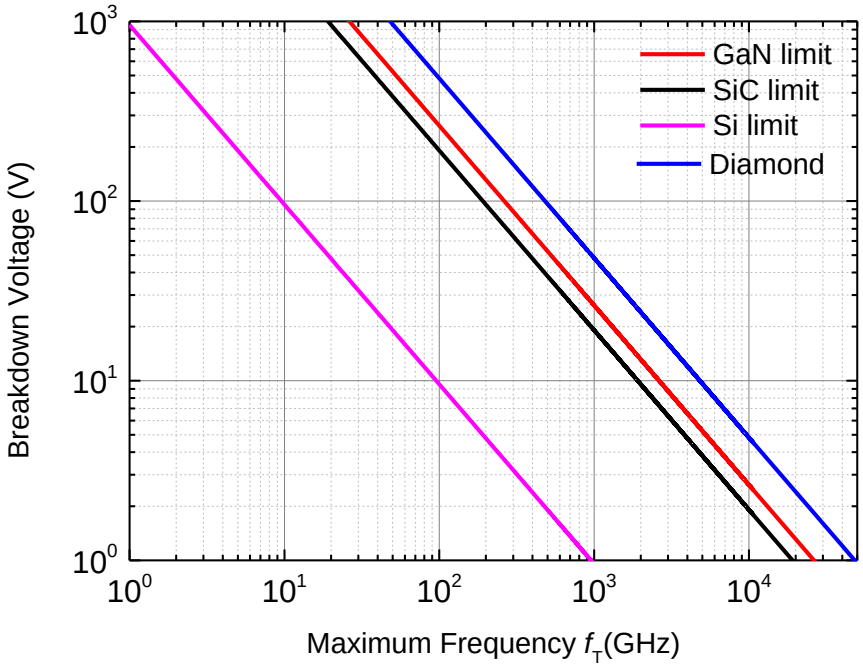


**Figure 2.10:** Plot of the maximum operating voltage for transistors made of selected semiconductors as a function of estimated $f_T$. The plot estimates are based on the equation (2-22) and table 2.1

### 2.2.3. AlGaN/GaN HEMTs as Logic Device

Presently silicon dominates digital logic applications. However, the feature sizes of silicon devices approach values where fundamental physics limitations lead to diminishing returns on investment in further scaling. Thus advanced research and development in microelectronics are

focusing on new materials that might have significant or even overwhelming advantages over silicon in certain applications.

AlGaN/GaN high electron mobility transistors (HEMT) are excellent candidates for integrated circuits used in elevated temperature and radiation environments owing to the wide bandgap [54-57]. They can work in high temperature environments, such as automotive, aviation, chemical reactor, and oil exploration systems, and hard radiation environments, such as space applications. Also, AlGaN/GaN 2DEG has a high electron mobility and it provides a semi-insulating substrate that produces a high switching current and lower parasitic capacitance, thus a higher operating speed is achievable in digital applications. Using n-channel HEMTs, direct-coupled field-effect transistor (FET) logic (DCFL), such as an E/D HEMT inverter, NAND gate and D flip-flop, which features integrated enhancement/depletion-mode (E/Dmode) HEMTs, offers the simplest circuit configuration [58]. Recently, digital ICs based on integrated enhancement/depletion (E/D)-mode HEMTs have been demonstrated using a recess gate [56] and fluoride-plasma-treatment techniques [60].

In this thesis, for the first time, enhancement/depletion-mode (E/D-mode) double-channel HEMTs are proposed to implement an inverter. The detailed characteristics of such inverter will present in separate chapter.

Regards to the fascinating properties of GaN arise a question, do we need a wide bandgap and high mobility for Digital HEMTs?:

For digital devices, switch-off with high Ion/Ioff mandatory. However, Wide $E_G$ resulting in low $I_{off}$ (where $I_{off} \propto \exp(-E_G/mk_BT)$) and high $\mu$ give us high $I_{on}$ (fast switching). As a result, wide Bandgap and High Mobility are needed for digital devices.[1]

[1] 2D Materials: Transistors, Memristive Effects, Memristors, F. Schwierz, Workshop DFG-Forschergruppe 2093 TU Ilmenau.

## 2.3. Theoretical Breakdown Voltage and ON-State Resistance in Power Devices [61]

One of the most unique feature of power semiconductor devices is their ability to withstand high voltages. The desire to control larger power levels in motor drive and power distribution systems [61, 62] has encouraged the development of power devices with larger breakdown voltages.

In a semiconductor, the ability to support high voltages without the onset of significant current flow is limited by the avalanche breakdown phenomenon, which is dependent on the electric field distribution within the structure. High electric fields can be created within the interior of power devices as well as at their edges. The design optimization of power devices must be performed to meet the breakdown voltage requirements for the application while minimizing the ON-state voltage drop, so that the power dissipation is reduced.

In this section the theory behind the avalanche and the punch-through breakdown limitations and the ideal specific ON-state resistance are discussed.

### 2.3.1. Theoretical Breakdown Voltage

Power devices are designed to support high voltages within a depletion region formed across either a p–n junction, a metal-semiconductor (Schottky-barrier) contact, or a metal-oxide-semiconductor (MOS) interface. Any charge carrier that enter the depletion layer either due to the space-charge generation phenomenon or by diffusion from adjacent quasineutral regions are swept out by the electric field produced in the region by the applied voltage. As the applied voltage (drain voltage) is increased, the electric field in the depletion region increases, resulting in acceleration of the mobile carriers to higher velocities. With further increase in the electric field, the mobile carriers gain sufficient kinetic energy from the electric field, so that their interaction with the lattice atoms produces the excitation of electrons from the valence band into the conduction band. The generation of electron–hole pairs due to energy acquired from the electric field in the semiconductor is referred to as the impact-ionization. Since the electron–hole pairs created by impact-ionization also experience acceleration by the electric field in the depletion region, they participate in the creation of further pairs of electrons and holes. As a result, impact ionization is a multiplicative phenomenon, which produces a cascade of mobile carriers being transported through the depletion region leading to a significant current flow through it. Since the device is unable to sustain the application of higher voltages due to a rapid increase in the current, it is considered to undergo avalanche breakdown. Thus, avalanche breakdown limits the maximum operating voltage for power devices.

The physics of the avalanche breakdown can be analyzed in relation to the properties of the semiconductor region (depletion region) that is supporting the voltage. This holds true for an abrupt p-n junction or a metal–semiconductor (Schottky barrier) contact (Figure 2.11). However, one-dimensional 1D abrupt junction can be used to understand the drift region within power devices. The case of a $p^+$-n junction is illustrated in Figure 2.11(a) where the $p^+$ side is assumed to be very highly doped, so that the electric field supported within it can be neglected. When this junction is reverse-biased by the application of a positive bias to the n-region, a depletion region is formed in the n-region together with the generation of a strong electric field within it that supports the voltage.

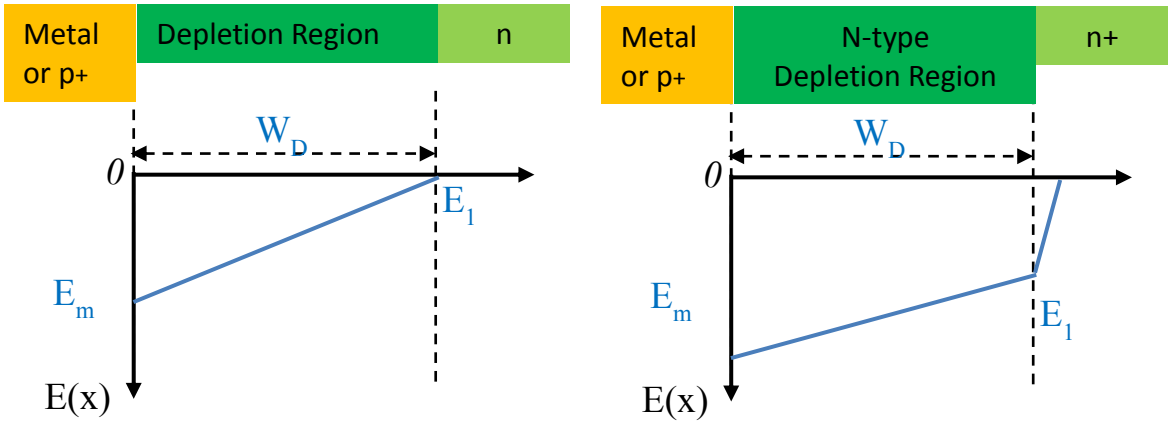


**Figure 2.11.** Electric field for (a) an abrupt parallel-plane (metal or $p^+$)/n junction and (b) punch-through design for a (metal or $p^+$)-i-n junction.

An analytical solution for the avalanche breakdown voltage in abrupt one-dimensional junctions, BV, as a function of the donor concentration in the uniformly doped n-region, $N_D$, the can be derived for GaN [63]:

$$BV = 2.87 \times 10^{15} N_D^{-3/4} \qquad 2\text{-}23$$

The avalanche breakdown voltages calculated using this solution is shown in Figure 2.12 for GaN material system.

The onset of the avalanche breakdown for an abrupt parallel-plane junction is accompanied by a maximum electric field at the junction referred to as the critical electric field for breakdown, $E_C$. The critical electric field for wurtzite GaN as a function of doping concentration is given by [63]:

$$E_C = 3.4 \times 10^4 N_D^{1/8} \qquad 2\text{-}24$$

In the case of some power devices designs the resistance of the drift region is greatly reduced during ON-state current flow by the injection of a large concentration of minority carriers. In these cases, the doping concentration of the drift region does not determine the resistance to the

ON-state current flow. Consequently, it is preferable to use a thinner depletion region with a reduced doping concentration to support the voltage. This configuration for the drift region is called the punch-through design.

The electric field distribution for the punch-through design is shown in Figure 2.11(b). In comparison with the triangular electric field distribution shown in Figure 2.11(a), the electric field for the punch-through design takes a trapezoidal shape. The electric field varies more gradually through the drift region due to its lower carrier concentration and then very rapidly with distance within the n+ end region due to its very high carrier concentration. The electric field at the interface between the drift region and the n+ end region is given by:

$$E_1 = E_m - \frac{qN_D}{\varepsilon_S} W_p \qquad 2\text{-}25$$

Where $E_m$ is the maximum electric field at the junction, $N_D$ is the doping concentration in the drift region, and $W_P$ is the width of the drift region. The voltage supported by the punch-through diode is given by:

$$V_{PT} = \left(\frac{E_m + E_1}{2}\right) W_p \qquad 2\text{-}26$$

If the small voltage supported within the n+ end region is neglected. The punch-through diode undergoes avalanche breakdown when the maximum electric field ($E_m$) becomes equal to the critical electric field ($E_C$) for breakdown. Using this condition in Eq. 2–26 together with the field distribution in Eq. 2–25, the breakdown voltage for the punch-through diode is given by:

$$BV_{PT} = E_C W_P - \frac{qN_D W_P^2}{2\varepsilon_S} \qquad 2\text{-}27$$

The punch-through breakdown voltages calculated using this relationship are shown in Figure 2.12 for GaN with various thicknesses for the drift region. In performing these calculations, the change in the critical electric field with doping concentration was taken into account. For any doping concentration for the drift region, the breakdown voltage for the punch-through diode is reduced due to the truncation of the electric field at the n+ end region.

The breakdown voltage becomes smaller as the thickness of the drift region is reduced. It can be seen that a 5μm thickness of the drift region with doping concentration of $10^{16}$ $cm^{-3}$ gives more than 1200 V of breakdown voltage. The actual experimental value of the breakdown voltage is far from these theoretical predictions. The material imperfections, such as the vertically threading dislocations, lead to premature breakdown. Therefore, the edge termination technique should be developed for GaN to prevent the early breakdown, and the crystal quality should be advanced to improve the GaN device performance [64].

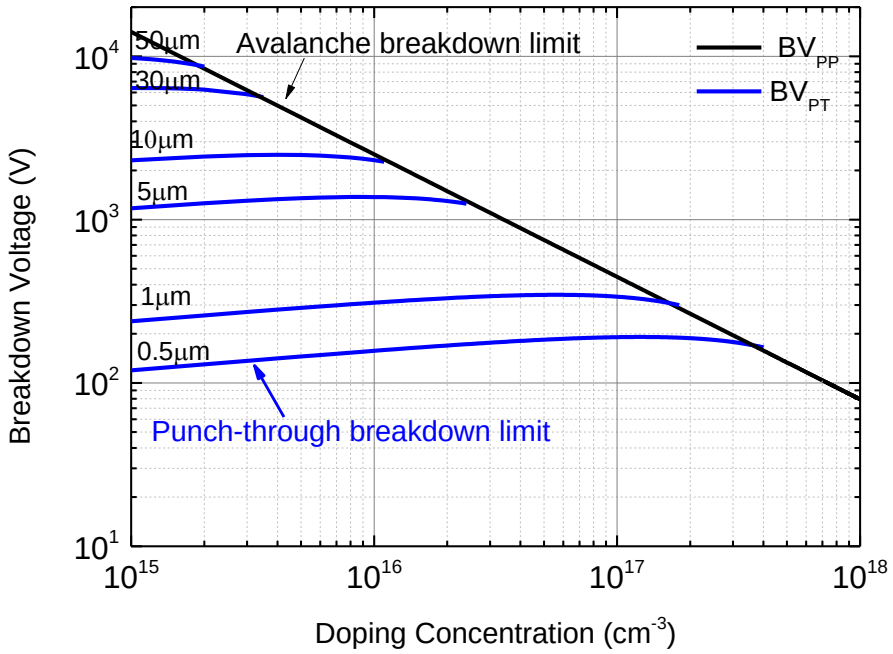


**Figure 2.12.** Breakdown Voltage as function of drift region doping level for GaN.

### 2.3.2. Power Device Limits Calculation

The semiconductor structures discussed above contain a drift region, which is designed to support the blocking voltage. The properties (doping concentration and thickness) of the ideal drift region can be analyzed by assuming an abrupt junction profile with high carrier concentration on one side and a low uniform carrier concentration on the other side, while neglecting any junction curvature effects by assuming a parallel-plane configuration. The resistance of the ideal drift region can then be related to the basic properties of the semiconductor material. Such semiconductor structure own a triangular electric field distribution, as shown in Figure 2.13, within a uniformly doped drift region with the slope of the field profile being determined by the doping concentration.

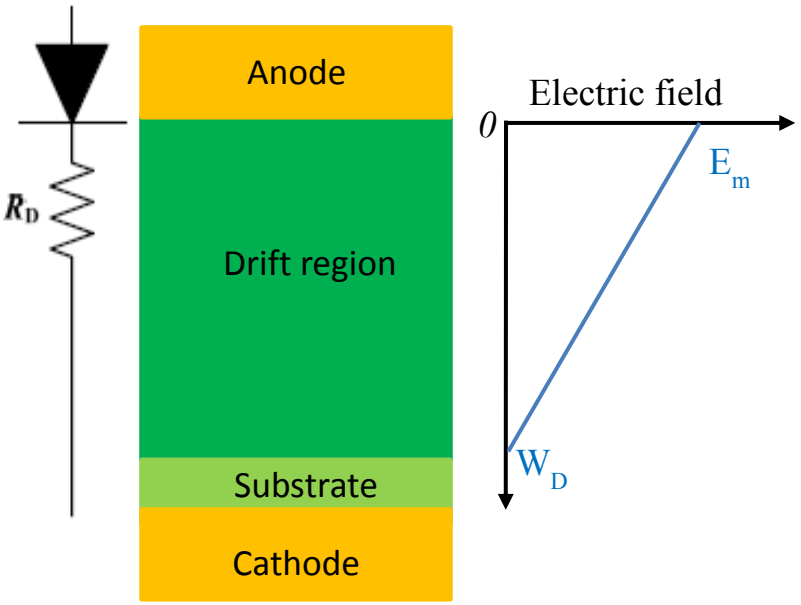


**Figure 2.13.** The ideal drift region and its electric field distribution [63]

The maximum voltage that can be supported by the drift region is determined by the maximum electric field ($E_m$) reaching the critical electric field ($E_c$) for breakdown for the semiconductor material. The critical electric field for breakdown and the doping concentration then determine the maximum depletion width ($W_D$). The resistance of ideal drift region of area, A, is given by:

$$R.A = \int_0^{W_D} \rho(x)dx = \int_0^{W_D} \frac{dx}{q\mu_n N_D(x)} \qquad 2\text{-}28$$

The specific resistance (resistance per unit area) of the ideal uniformly doped drift region is therefore:

$$R_{on,sp} = \left(\frac{W_D}{q\mu_n N_D}\right) \qquad 2\text{-}29$$

The depletion width under breakdown conditions is given by:

$$W_D = \frac{2BV}{E_c} \qquad 2\text{-}30$$

where BV is the desired breakdown voltage. The doping concentration in the drift region required to obtain this BV is given by:

$$N_D = \frac{\varepsilon_S E_c^2}{2qBV} \qquad 2\text{-}31$$

Combining these relationships, the specific resistance of the ideal drift region is obtained:

$$R_{on-ideal} = \frac{4BV^2}{\varepsilon_S \mu_n E_c^3} \qquad 2\text{-}32$$

The denominator of this equation ($\varepsilon_S \mu_n E_C^3$) is commonly referred to as Baliga's figure of merit for power devices. It is an indicator of the impact of the semiconductor material properties on the resistance of the drift region.

Practical specific ON-resistance estimation is calculated using the following approximation:

For GaN [63]:

$$R_{ON}(\Omega.cm^2) = 3.12 \times 10^{-12} BV^{2.5} \qquad 2\text{-}33$$

For 4H-SiC [63]:

$$R_{ON}(\Omega.cm^2) = 5.55 \times 10^{-12} BV^{2.5} \qquad 2\text{-}34$$

and for Si [63]:

$$R_{ON}(\Omega.cm^2) = 6.65 \times 10^{-9} BV^{2.5} \qquad 2\text{-}35$$

Using the typical sheet carrier density of $1 \times 10^{13}$ cm$^{-2}$ with an electron mobility of 2000 cm$^2$ (V.s)$^{-1}$ reported in the 2D-gas for the lateral AlGaN/GaN HEMT structures yields [67]

$$R_{ON}(\Omega.cm^2) = 3.577 \times 10^{-9} BV^{2.5} \qquad 2\text{-}36$$

The specific on-resistance for the lateral GaN HEMT structure is plotted in figure 2.14. The line corresponding to the lateral GaN HEMT devices is not parallel to the lines for the other vertical device structures shown in the figure. The above analysis indicates that the ideal specific on-resistance for lateral GaN HEMT devices is lower than that predicted for the vertical GaN FET devices, and consequently superior to 4H-SiC and Si devices as well. The lateral GaN HEMT structures are expected to have an ideal specific on-resistance that is 1.88, 2.76 and 4.05-times smaller than for the vertical GaN FET devices at breakdown voltages of 100, 1000 and 10 000 V, respectively.

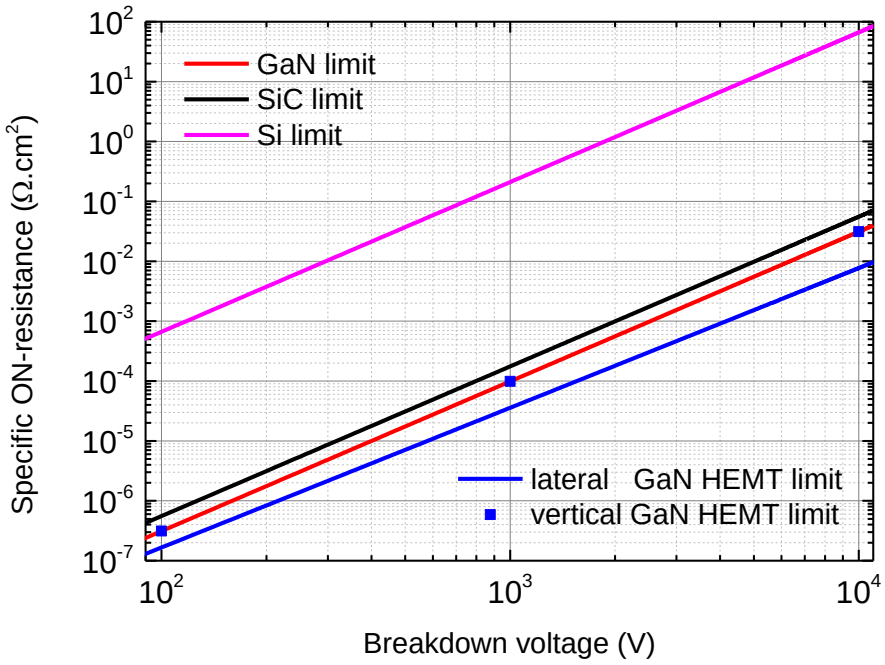


**Figure 2.14** Comparison of GaN ideal specific on-resistance with Si and SiC.

An example of the theoretical, total specific ON-resistance with contributions of drift region (Eq. 2–33, 2–34, 2–35 and 2–36) is presented in Figure 2.14 for Si, GaN and 4H-SiC. The main

advantage of the wide-bandgap materials GaN and SiC is clear: for the same breakdown voltage, they offer a significantly reduced ON-resistance and hence also reduced ON-state losses.

The theoretical total specific ON-resistance are used as theoretical limits along this work for benchmarking the results in this work with the state-of-the-art devices.

### 2.3.3 Breakdown Mechanisms of AlGaN/GaN Based HEMTs

In switching operation the transistors alternate between ON-state were the gate opens the channel and allow the carriers flow through the device and OFF-state were the gate closes the channel and blocks the current of carriers. At OFF-state the gate potential, $V_{GS}$, is lower than the device's threshold voltage, $V_{Th}$, and considered as subthreshold conditions. For efficient switching the OFF-state operation point conditions should be at high positive drain voltage and negligible drain current therefore a strong gate blocking capability is required. At very high positive drain voltage condition the blocking capability of the device degrades and gives rise to subthreshold leakage, (STL), current. The subthreshold leakage current will increase and become significant, thereby reducing the efficiency of the switching. A significant leakage current is considered as three orders of magnitude lower than the device's maximal output current. At high voltages, currents that are higher than this value may initiate destructive processes in the device therefore it is considered to be the starting point of the device breakdown. In most cases, the breakdown voltage is usually considered as the voltage where either the sub threshold drain leakage or the gate leakage increases above 1 mA/mm.

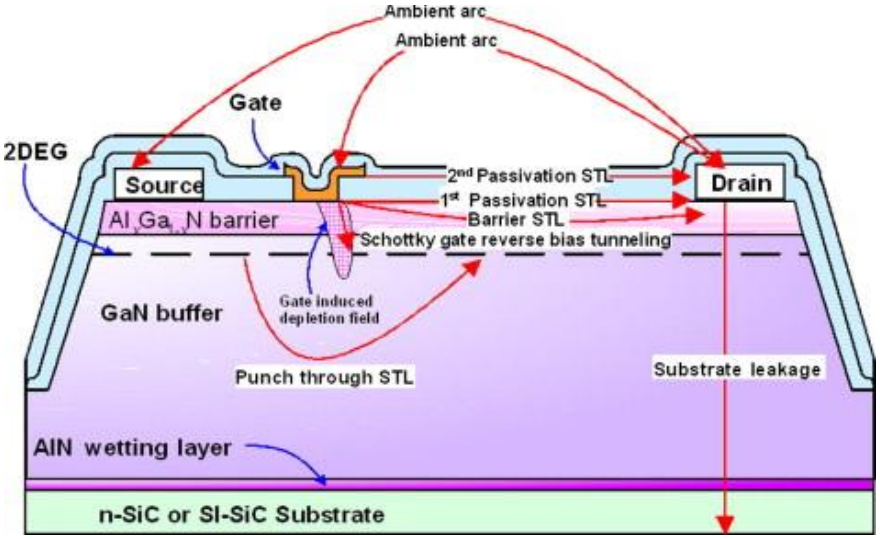


**Figure 2.14** Illustration of most important sub-threshold current leakages (STL) and breakdown paths might appear during high voltage in GaN-based HEMTs [65].

The main physical reasons for sub threshold leakage current increase at higher drain bias voltage are sketched in Fig. 2.14 and described in the following. They have to be taken into account for high voltage GaN device engineering:

- Electron punch through in the buffer underneath the gated channel region [66]: This effect depends on the magnitude of the vertical electric field in the gate region and the ability of the buffer structure to confine electrons to the channel. Therefore, any means to reduce high vertical electric fields and to confine electrons to the channel are efficient (potential barrier in buffer [5,67,68] and field plates [69,70]).
- Schottky gate reverse bias tunnelling: This originates from the drain side edge of the gate and is triggered by high electric fields present in this particular device region. Any means to reduce the peak electrical field there are of particular interest for high voltage devices. Usually field plates [69,70] and/or slanted gate constructions [71] are applied to mitigate these effects.
- Vertical device breakdown or substrate leakage across the epitaxial layers to conductive substrates such as n-SiC or Si: This is mainly an issue of the buffer technology and can be prevented by suitable epitaxial concepts [7,66,72,73]. High voltage GaN devices are placing very stringent demands on high voltage buffer structures since in most cases these devices are fabricated on conductive substrates (Si, n-SiC) which are usually connected to either the drain or the source terminal of the power devices.
- Surface related breakdown: This is mainly associated with the quality of device passivation itself and the interfaces between passivation layers or the semiconductor surface itself. Here both, passivation material and lateral device design have to be matched to each other in order to obtain optimum performance [74].
- Finally, ambient arcing between closely spaced device electrodes may also take place if the devices are operated in air. This has to be taken into account by device layout design, design and technology of passivation and device packaging.

# Chapter 3

# Simulation, Modeling and Physics-Based of AlGaN/GaN HEMTs

## 3.1 Introduction

This chapter will give overview on simulations which have been carried out relevant to this research. Device simulation and modelling are crucial in the development of any technology allowing designers to optimise device designs and process flows before putting them into fabrication. This is particularly important for GaN based devices when considering the large cost of the material. Our in-house 1D numerical Schrödinger-Poisson solver [75] and Silvaco's commercial component simulator ATLAS [76] were used as basic tools.

## 3.2 1D numerical Schrödinger-Poisson simulation

The simulation tool used for the one dimensional device simulations is our in-house 1D numerical Schrödinger-Poisson solver [75]. To calculate the free carrier distributions and band diagrams we employ the effective-mass approximation. Along the growth direction of GaN/AlGaN/GaN heterostructures (i.e., in the z direction), carriers are confined in deep and narrow quantum wells. This requires a self-consistent solution of the one-dimensional Schrödinger and Poisson equations.

Since both electrons and holes are considered, two Schrödinger equations – one for electrons and one for holes – have to be solved. In the present work, our in-house Schrödinger-Poisson solver, expanded by the Schrödinger equation for holes, is used [77]. The Schrödinger equation for electrons reads as

$$\left[ -\frac{\hbar^2}{2} \frac{d}{dz} \left( \frac{1}{m_{\|}^{*}(z)} \frac{d}{dz} \right) - q\,\phi(z) + \Delta E_C(z) \right] \psi_i(z) \quad = \quad E_i\, \psi_i(z) \qquad \text{3-1}$$

Here, $E_i$ and $\psi_i(z)$ are the energy level and wave function of the $i$th subband, $m_{\|}^{*}(z)$ is position dependent electron effective mass in the $z$-direction, $\phi(z)$ is the electrostatic potential, and $\Delta E_C(z)$ is equal to the conduction band offsets at a heterojunction and zero elsewhere in the structure.

To account for the quantization of the hole gas, the Schrödinger equation for holes is solved in analogy to the case for the electrons. For simplicity, instead of heavy-, light-, and split-off

valence bands we consider only one valence band with an effective mass equal to the density-of-states effective hole mass.

In general, the Poisson equation is given by

$$\frac{d}{dz}\left[-\varepsilon(z)\frac{d\phi(z)}{dz}+P_{tot}(z)\right] = q\left[N_D^+(z)-N_A^-+p(z)-n(z)\right] \qquad 3\text{-}2$$

where $P_{tot}(z)$ is the overall permanent polarization (i.e., the sum of spontaneous and piezoelectric polarization [9,10]), $N_D^+(z)$ and $N_A^-(z)$ are the ionized donor and acceptor concentrations, $\varepsilon(z)$ is the dielectric constant, and $n(z)$ and $p(z)$ are the position dependend electron and hole concentrations. Since in the present study we assume only n-type doping, $N_A^-(z)$ in Eq. (3-2) is set to zero.

For the relative dielectric constant $\varepsilon_r$, energy gap $E_G$, conduction and valence band offsets $\Delta E_C$ and $\Delta E_V$, spontaneous polarization $P^{SP}$, and piezoelectric polarization $P^{PZ}$ in GaN and AlGaN, the models from Ref. [10] have been used.

The electron effective masses $m^*_{\parallel}$ (in the z direction) and $m^*_{\perp}$ (normal to the z direction) for GaN and AlN are taken from Ref. [78] and the corresponding masses for AlGaN are obtained by linear interpolation. For the effective hole mass $m_h$, the density-of-states effective hole mass from Ref. [82] is used.

Table 3.1 summarizes important parameters for GaN and $Al_{0.3}Ga_{0.7}N$ used in the simulations. According to [10], the spontaneous and piezoelectroc polarizations result in a bound polarization charge density of $-1.39\times10^{13}$ cm$^{-2}$ at the cap/barrier interface and $1.39\times10^{13}$ cm$^{-2}$ at the barrier/bulk interface.

| Material | $\varepsilon_r$ | $m_{\parallel}^*$ | $m_{\perp}^*$ | $m_h$ | $E_G$ | $\Delta E_C$ | $P^{SP}$ | $P^{PZ}$ |
|---|---|---|---|---|---|---|---|---|
| GaN | 10.28 | 0.186 | 0.209 | 1.50 | 3.42 | 0 | -0.034 | 0 |
| $Al_{0.3}Ga_{0.7}N$ | 10.29 | 0.227 | 0.245 | 3.228 | 4.023 | 0.38 | -0.04639 | -0.00983 |

Tab. 3.1. Important material parameters of GaN and $Al_{0.3}Ga_{0.7}N$ used in this work. The effective masses are given in units of the electron rest mass $m_0$, the gap and the conduction band offset in eV, and the polarizations $P^{SP}$ and $P^{PZ}$ in C/m$^2$.

### 3.3 ATLAS Software

The simulation tool used for the two dimensional device simulations is ATLAS from Silvaco International's software package [76]. The software is capable of simulating numerically various semiconductor materials, including Si, GaN, GaAs and so on in 1D, 2D and 3D.

There are five groups of statements, which, if not correctly stated, will result in errors or erroneous simulations. The required groups and statements are described briefly in Figure 3.1 [76]:

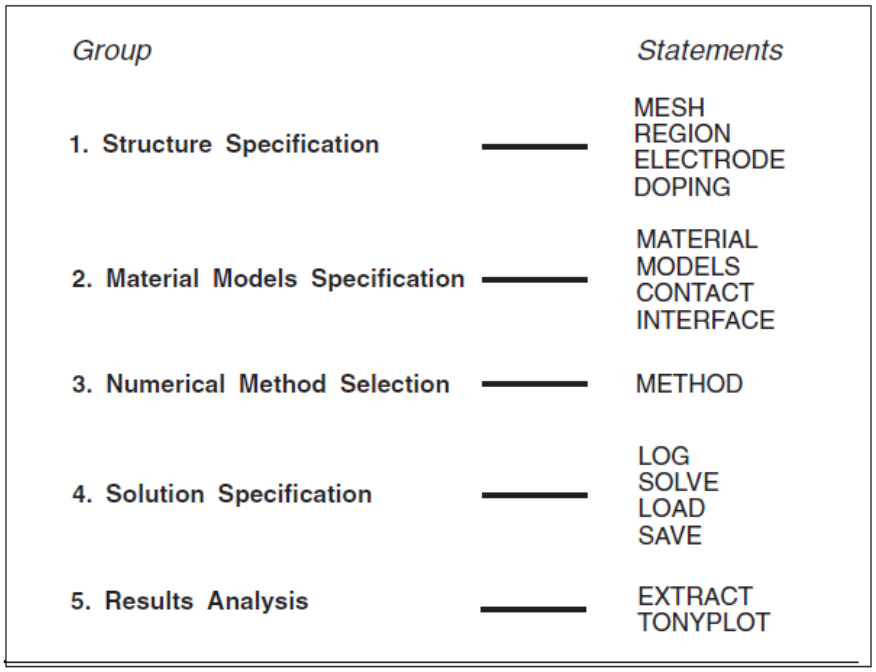


**Figure 3.1:** Atlas command groups with the primary statements [76]

In Fig. 3.1 command groups represent the entire structure definition and solution method. It is critical to have a firm understanding of the simulation variables prior to defining a structure. A small change in one variable or solution method can have undesirable consequences on device performance. Figure 3.2 depicts a flow chart of the device simulation utilizing Silvaco International's simulators and modules.

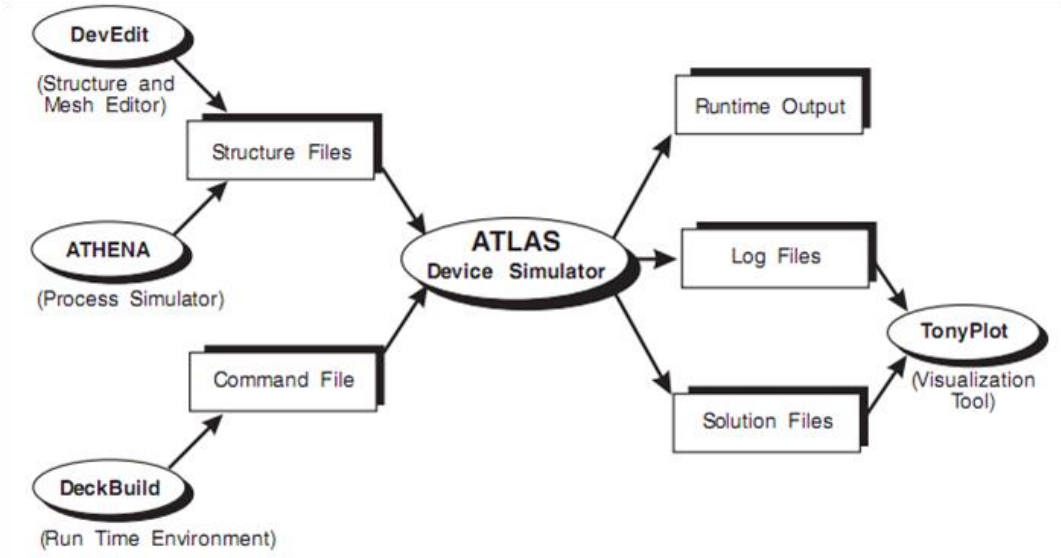


**Figure 3.2**: Silvaco Simulation Flowchart [76].

### 3.3.1. Silvaco Semiconductor Physics-Based Modeling Equations

The models developed to simulate the operation of semiconductor devices consist of a set of fundamental equations derived from Maxwell's laws, Poisson's equation, the continuity equations and the drift-diffusion transport equations [76]. Poisson's Equation relates variations in electrostatic potential to local charge densities. The continuity and the transport equations describe the way that the electron and hole densities evolve as a result of transport processes, generation processes, and recombination processes. The following sections discuss the equations in broad terms, and when necessary, a more detailed explanation of the equations will be presented.

The method in which the above equations will be solved is a prime consideration when developing a device model in ATLAS™. Several different numerical methods can be used for calculating the solutions to various device structures. The NEWTON algorithm solves all four equations in a coupled manner.

#### 3.3.1.1. Poisson's Equation

Poisson's equation is a well-known partial differential equation that has functions in electrostatics and theoretical physics. In semiconductor modeling it often serves as the starting point in obtaining quantitative solutions for electrostatic variables [79]. In electrostatics, Poisson's equation relates the electrostatic potential to the space charge density and is given by [76]:

$$div(\varepsilon \nabla \Psi) = -\rho \qquad 3\text{-}3$$

where Ψ is the electrostatic potential, ε is the local permittivity, and ρ is the local space charge density. The local space charge density is a function of all mobile and fixed charges including electrons, holes, and impurities. The electric field is obtained from the gradient of the potential and is given by [76]:

$$\vec{E} = -\nabla \Psi \qquad 3\text{-}4$$

### 3.3.1.2. Carrier Continuity Equations

The carrier continuity equations for electrons and holes are defined by [76]:

$$\frac{\partial n}{\partial t} = \frac{1}{q} div\overrightarrow{J_n} + G_n - R_n \qquad 3\text{-}5$$

$$\frac{\partial p}{\partial t} = -\frac{1}{q} div\overrightarrow{J_p} + G_p - R_p \qquad 3\text{-}6$$

where n and p are the electron and hole concentration, $\overrightarrow{J_n}$ and $\overrightarrow{J_p}$ are the electron and hole current densities, $G_n$ and $G_p$ are the generation rates for electrons and holes, $R_n$ and $R_p$ are the recombination rates for electrons and holes and q is the magnitude of the charge on the electron. It is possible to solve for only the holes or electrons in the equations, and the model presented in this thesis solves the equations for both electrons and holes [77].

However, in the case of GaN-based HEMTs it is possible to use electrons only as charge carriers due to their dominance in the device characteristics, where this will significantly speed up simulations.

### 3.3.1.3. Transport Equations

Electrons in thermal equilibrium at temperature $T_L$ (lattice temperature) within a semiconductor lattice obey Fermi-Dirac statistics. That is the probability $f(\varepsilon)$ that an available electron state with energy ε is occupied by an electron is given by [76]:

$$f(\varepsilon) = \frac{1}{1+\exp(\frac{\varepsilon - E_F}{KT_L})} \qquad 3\text{-}7$$

where $E_F$ is a spatially independent reference energy known as the Fermi level, $T_L$ is the lattice temperature and k is the Boltzmann's constant. If ε - $E_F$ >> $K.T_L$, equation 3-5 can be approximated as:

$$f(\varepsilon) = \exp(\frac{E_F - \varepsilon}{KT_L}) \qquad 3\text{-}8$$

Statistics based on equation 3.8 are known as the Boltzmann statistics and were utilized in the formulation of the HEMT model. The current density equations known as the charge transport models are obtained by applying simplifications to the Boltzmann transport equation. These assumptions can result in a number of different transport models such as the drift-diffusion model, the energy balance model or the hydrodynamic model [76]. The choice of charge transport model will then have a major influence on the choice of generation and recombination model. The following equations were derived in chapter three of [76], and show the conventional form of the drift-diffusion equation:

$$\overrightarrow{J_n} = qn\mu_n\vec{E}_n + qD_n\nabla n \qquad 3\text{-}9$$

$$\overrightarrow{J_n} = qp\mu_p\vec{E}_p + qD_p\nabla p \qquad 3\text{-}10$$

where $D_n$ and $D_p$, in the case of the Boltzmann statistics corresponds to:

$$D_n = \frac{KT_L}{q}\mu_n \qquad 3\text{-}11$$

$$D_p = \frac{KT_L}{q}\mu_p \qquad 3\text{-}12$$

### 3.3.1.4. Polarization Effects

Perhaps one of the most challenging aspects of modeling heterojunction devices in ATLAS™ is implementing the polarization effects present at the interface of the heterojunction. It has been widely published [81, 82] that surface donor like traps are the source of electrons in the channel and the polarization effects in AlGaN/GaN structures force the electrons into the channel. Previous modeling efforts have modeled the polarization effects as an interface charge of approximate $1x10^{13}$ q/cm$^3$ at the heterojunction interface. (section 2.1.2 above).

Recent upgrades to ATLAS™ include the ability to model polarization effects directly. The ATLAS™ polarization model was designed to simulate polarization in wurtzite materials and include spontaneous polarization and piezoelectric polarization.

The model allows the designer to input the piezoelectric constants $e_{31}$ and $e_{33}$ as well as the elastic constants $C_{13}$ and $C_{33}$

The polarization effects were modeled as an interface charge of approximately $1x10^{13}$ q/cm$^3$ on the GaN side of the heterojunction. Ambacher et al. [81] utilizes the lattice constant (a), the piezoelectric constants (e), and the elastic constants (C) to derive the sheet concentration density in wurtzite materials.

The sheet charge density σ (x) is given by:

$$|\sigma(x)| = |P_{PZ}(AlGaN) + P_{SP}(AlGaN) - P_{SP}(GaN)| \qquad 3\text{-}13$$

Substituting equation 2.9 for the $P_{Pz}$ variable gives:

$$|\sigma(x)| = \left|2\left(\frac{a(0)-a_0(x)}{a_0(x)}\right)\left(e_{11}(x) - e_{33}(x)\left(\frac{C_{13}(x)}{C_{33}(x)}\right)\right) + P_{SP}(x) - P_{SP}(0)\right| \qquad 3\text{-}14$$

When the sheet charge density σ is divided by e, the result is the polarization induced sheet charge density. Figure 3.3 illustrates the induced sheet charge as a function of alloy composition.

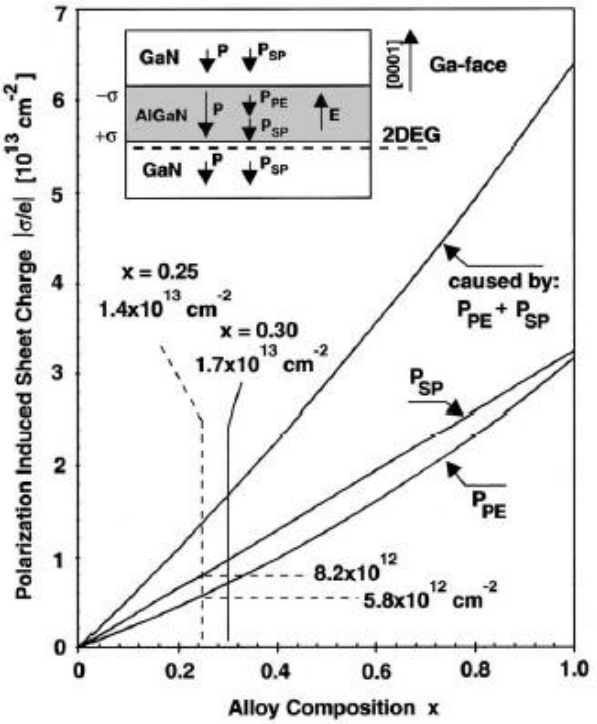


**Figure 3.3:** Sheet charge as a function of alloy composition [81].

### 3.3.2. Material Parameters and Silvaco Physical Models

The model developed in ATLAS™ is based on specific definitions and use of physical models that describe the material properties of nitride compounds. Silvaco "ATLAS" contains many build-in physical models and material properties that can be used to simulate such devices. Here are the models used by the simulation to define the physical properties of the materials presented by the order in the simulation's scripts.

#### 3.3.2.1. Nitride Material Properties: Band gap, Electron Affinity, Permittivity and Density of States Masses

The following sections describe the relationship between mole fraction, *x*, and the material parameters and various physical models specific to the $Al_xGa_{1-x}N$ system. By default, the bandgap for the nitrides is calculated in a two-step process. First, the bandgap(s) of the relevant binary compounds are computed as a function of temperature, *T*(K), using [83]:

$$E_g(GaN) = 3.507 - \frac{0.909\times10^{-3}T^2}{T+830.0} \quad \text{3-15}$$

$$E_g(AlN) = 1.994 - \frac{0.245\times10^{-3}T^2}{T-624} \quad \text{3-16}$$

Then, the dependence on composition fraction, *x*, is described [55]:

$$E_g(Al_xGa_{1-x}N) = E_g(AlN)x + E_g(GaN)(1-x) - 1.3x(1-x) \quad \text{3-17}$$

The electron affinity is calculated such that the band edge offset ratio is given by [84]:

$$\frac{\Delta E_C}{\Delta E_V} = \frac{0.7}{0.3} \quad \text{3-18}$$

The permittivity of the nitrides as a function of composition fraction, *x*, is given by linear interpolations of the values for the binary compounds [81].

$$\varepsilon(Al_xGa_{1-x}N) = -0.3x + 10.4 \quad \text{3-19}$$

The nitride density of states masses as a function of composition fraction, *x*, is given by linear interpolations of the values for the binary compounds [83]:

$$m_e^*(Al_xGa_{1-x}N)/m_0 = 0.314x + 0.2(1-x) \quad \text{3-20}$$

$$m_h^*(Al_xGa_{1-x}N)/m_0 = 0.417x + 1.0(1-x) \quad \text{3-21}$$

### 3.3.2.2. Carrier Mobility Definitions

A composition and temperature dependent low-field model is used and defined as the mobility model for the nitride Wurtzite phase materials system. The model is specified for electrons as the majority carriers. The Farahmand Modified Caughey Thomas (FMCT) model [40] was the result of fitting a Caughey Thomas [85] like model to Monte Carlo data: low field mobility:

$$\mu_0(T,N) = \mu_{min}\left(\frac{T}{300}\right)^{\beta_1} + \frac{(\mu_{max}-\mu_{min})\left(\frac{T}{300}\right)^{\beta_2}}{1+\left[N_{ref}\left(\frac{T}{300}\right)^{\beta_3}\right]^{\alpha\left(\frac{T}{300}\right)^{\beta_4}}} \qquad 3\text{-}22$$

Here, $T$ is the lattice temperature, $N_{ref}$ is the total doping density, and $\alpha$, $\beta_1$, $\beta_2$, $\beta_3$, $\beta_4$, $\mu_{min}$ and $\mu_{max}$ are parameters that are determined from Monte Carlo simulation [40]. A nitride specific field dependent mobility model for high field mobility could be specified using the following dependence (FMCT.N and GANSAT.N):

$$\mu_n(E) = \frac{\mu_0(T,N)+\vartheta_n^{sat}\frac{E^{n_1-1}}{E_c^{n_1}}}{1+a\left(\frac{E}{E_c}\right)^{n_2}+\left(\frac{E}{E_c}\right)^{n_1}} \qquad 3\text{-}23$$

where $\mu_0$(T, N) is the low field mobility as expressed in Eq. 3–22. The parameters in the model ($\vartheta_n^{sat}$, $E_c$, $a$, $n_1$ and $n_2$) are determined from Monte Carlo simulation [40].

### 3.3.2.3. Carrier Generation-Recombination Models [76]

Carrier generation-recombination is the process through which the semiconductor material attempts to return to equilibrium after being disturbed from it. If we consider a homogeneously doped semiconductor with carrier concentrations n and p to the equilibrium concentrations $n_0$ and $p_0$, then at equilibrium a steady state balance exists according to:

$$n_0 p_0 = n_i^2 \qquad 3\text{-}24$$

Semiconductors, however, are under continual excitation whereby n and p are disturbed from their equilibrium states: $n_0$ and $p_0$. For instance, light shining on the surface of a p-type semiconductor causes generation of electron-hole pairs, disturbing greatly the minority carrier concentration. A net recombination results which attempts to return the semiconductor to equilibrium. The processes responsible for generation-recombination are known to fall into six main categories: phonon transitions, photon transitions, Auger transitions, surface

recombination, impact ionization and tunneling. We focus in this study on phonon recombination. Photon effect, however, is important for narrow gap semiconductors and semiconductors whose specific band structure allows direct transitions [76].

### 3.3.2.4. Shockley-Read-Hall (SRH) Recombination

Phonon transitions occur in the presence of a trap (or defect) within the forbidden gap of the semiconductor. This is essentially a two step process, the theory of which was first derived by Shockley and Read [40] and then by Hall [85]. The Shockley-Read-Hall recombination is modeled as follows:

$$R_{SRH} = \frac{pn - n_{ie}^2}{\tau_{p0}\left[n + n_{ie} exp\left(\frac{E_{Trap}}{kT_L}\right)\right] + \tau_{n0}\left[p + n_{ie} exp\left(\frac{E_{Trap}}{kT_L}\right)\right]} \qquad 3\text{-}25$$

where $E_{TRAP}$ is the difference between the trap energy level and the intrinsic Fermi level, $T_L$ is the lattice temperature in degrees Kelvin and $\tau_{n0}$ and $\tau_{p0}$ are the electron and hole lifetimes. This model is activated by using the SRH parameter of the MODELS statement. The electron and hole lifetime parameters, $\tau_{n0}$ and $\tau_{p0}$, are user-definable in the MATERIAL statement [76].

In addition to the thermal generation provided by SRH, the *beam* statement is used to specify an optical source of carrier pair generation. This is generally a good strategy for analyzing breakdown especially in wide bandgap such materials as GaN or at low temperatures to improve convergence. This is not recommended when estimating sub-breakdown diode leakage currents though [86].

### 3.3.2.5. Impact Ionization Models [76]

In any space charge region with a sufficiently high reverse bias, the electric field will be high enough to accelerate free carriers up to a point where they will have acquired sufficient energy to generate more free carriers when in collision with the atoms of the crystal. In order to acquire sufficient energy, two principle conditions must be met.

First, the electric field must be sufficiently high. Then, the distance between the collisions of the free carrier must be enough to allow acceleration to a sufficiently high velocity

In other words, the carrier must gain the ionization energy $E_i$ between collisions. If the generation rate of these free carriers is sufficiently high this process will eventually lead to avalanche breakdown.

The general impact ionization process is described by the Equation 3-26.

$$G = a_n|\vec{J}|_n + a_p|\vec{J}|_p \qquad 3\text{-}26$$

Here, G is the local generation rate of electron-hole pairs, $\alpha_{n,p}$ are the ionization coefficient for electrons and holes and $J_{n,p}$ are their current densities. The ionization coefficient represents the number of electron-hole pairs generated by a carrier per unit distance travelled. The accurate calculation of this parameter has been researched because it is vital if the effects related to impact ionization, such as substrate current and device breakdown, are to be simulated. These models can be classified into two main types: local and non-local models.

We focus in this study on local models. Non-local models, however, perform a more rigorous approach by taking into account the energy that the carrier gains.

**Selberherr's Impact Ionization Model**

The ionization rate model proposed by Selberherr [87] is a variation of the classical Chynoweth model [88]. Activate this model by using the SELB parameter of the IMPACT statement, which is based upon the following expressions [89]:

$$a_n = ANexp\left[-\left(\frac{BN}{E}\right)^{BETAN}\right] \qquad 3\text{-}16$$

$$a_p = APexp\left[-\left(\frac{BP}{E}\right)^{BETAP}\right] \qquad 3\text{-}17$$

Here, E is the electric field in the direction of current flow at a particular position in the structure and the parameters AN, AP, critical field parameters BN and BP, BETAN, and BETAP are defined on the IMPACT statement. In the case of AN, AP, BN, and BP you can define a value of electric field, EGRAN V/cm, where for electric fields, >EGRAN V/cm, the parameters are: AN1, AP1, BN1, BP1, while for electric fields, <EGRAN V/cm, the parameters become AN2, AP2, BN2, and BP2. Table 5-19 from [76] shows the extracted default values for the Selberherr impact ionization model from [90] for GaN [76].

### 3.4. GaN-Based HEMTs Simulation Models and Parameters

The following section describes the methodology used in the physically based simulations of nitride based HEMTs devices. It is desired to match the simulation output characteristics to the actual electrical and physical performance of a typical manufactured device. The matching

process starts with the definition of the simulated structure, its fraction to fine elements by adequate progressive meshing and the materials building blocks. The simulation manual recommends models for use and has a build in material parameters tables based on the latest research results. Unfortunately, as could be seen in the following sections, it is not sufficient; the recommendations are not specific and does not include many of the required models for accurate description of a GaN-based HEMTs and other field effect devices. Therefore, additional models along with empirical modification in the existing models and parameters are required in order to achieve a useful tool for the device designer and researcher as a first order approximation.

### 3.4.1. Simulation Models and Parameter Modifications for an Empirical Matching

In Silvaco-"ATLAS" there are build-in models and nitride-based semiconductors physical parameters are in many cases based on Monte Carlo simulations and fit to physical properties measurements and not based on experimental device electrical measurements. Therefore in many cases the initial results of the simulation are by far to fit and describe a GaN based HEMTs measured electrical performance. Here some adjustments of the physical models parameters described above are needed. In addition Silvaco "ATLAS" does not specifically define the models and methods required to simulate a device such as GaN based HEMT but gives general guidelines and multiple freedom of choice to the user. The task of tuning the simulation to match the experimental measurements results requires turning large number of the simulation attempts and require from the user large number of time consuming iterations of trial-and-error to reach his goals.

## 3.5. Conclusions

The GaN-based device simulation is now a useful tool for design and physical insight-analysis that is require for development of such devices. Examples for device geometry design, epitaxial layers design and analysis of physical properties of GaN-based HEMTs during its operation using the physical based simulation is given throughout this work and detailed in each of the chapters.

# Chapter 4
# Investigation of GaN-based multiple-channel structures

## 4.1. Co-existence of two dimensional- electron and hole gases in GaN-based heterostructures

### 4.1.1. Introduction

Due to the lack of p-channel AlGaN/GaN HEMTs, new devices such as complementary GaN HEMTs cannot be implemented. It has been predicted by simulations that under certain conditions in GaN/AlGaN/GaN structures, a 2DHG (two-dimensional hole gas) may form at the upper GaN/AlGaN interface in addition to the 2DEG at the lower AlGaN/GaN interface [91,92]. The simultaneous appearance of 2DEGs and 2DHGs in GaN/AlGaN/GaN structures has recently been confirmed by experiments [92-94]. Coexisting electron and hole gases are highly undesirable for conventional n-channel HEMT operation and should be avoided. For other applications, however, they may be beneficial. Currently there is an intense interest in electron-hole-pair (exciton) condensation effects that may occur in closely spaced 2DEGs and 2DHGs separated by a thin barrier [95,96] and an interesting device concept, the BiSFET (bilayer pseudospin field-effect transistor) exploiting these effects has been proposed [97]. Another potential application for structures with coexisting 2DEGs and 2DHGs could be varactors with tailored capacitance-voltage capacitance. GaN-based varactor diodes are currently intensively studied [98,99]. Finally, 2DHGs alone, i.e., without coexisting 2DEGs, are useful for p-channel GaN-based HEMTs. In [100], for example, a p-channel GaN-based HEMT with GaN barrier and InGaN channel has been reported

In the present chapter, the formation of 2DEGs and 2DHGs and the conditions for the coexistence of two carrier gases in GaN/AlGaN/GaN structures are investigated in detail. Special emphasis is put on the effects of the layer design and the bias conditions on the electron and hole sheet densities. We focus on wurtzite Ga-face structures which are commonly used in GaN-based devices. The chapter is organized as follows. In Sec. 4.1.2 the simulation framework, basic device structure and results of numerical Schrödinger-Poisson simulations are presented. In Sec. 4.1.3, an analytical model that provides useful insights in the conditions for the formation of coexisting 2DEGs and 2DHGs is developed and results calculated with the new model are compared with those obtained from computationally more expensive Schrödinger-Poisson solutions. Finally, Sec. 4.1.4 concludes the Sec. 4.1.

### 4.1.2. Simulation Framework, Basic Device Structure and Results

#### 4.1.2.1. Simulation Framework and Basic Device Structure

To calculate the free carrier distributions and band diagrams we employ the effective-mass approximation, for more details see Sec. 3.2 above.

Figure 4.1 shows the basic design of the heterostructures investigated in the present work. It consists (from top to bottom) of a Schottky gate, an upper GaN layer serving as a cap and having a thickness $t_{cap}$, an $Al_{0.3}Ga_{0.7}N$ barrier with a thickness $t_{bar}$, and a thick GaN bulk having a grounded back-side contact. The GaN and AlGaN layers are assumed to be unintentionally n-type doped with a homogeneous donor concentration of $10^{16}$ $cm^{-3}$. The surface potential $E_{C0}$ is defined as the conduction band edge in the cap at the gate contact and is related to the applied gate voltage $V_G$ by

$$V_G = -(E_{C0} - \Phi_B)/q \qquad 4\text{-}1$$

where where $\Phi_B$ is the Schottky barrier height and $q$ is the elementary charge.

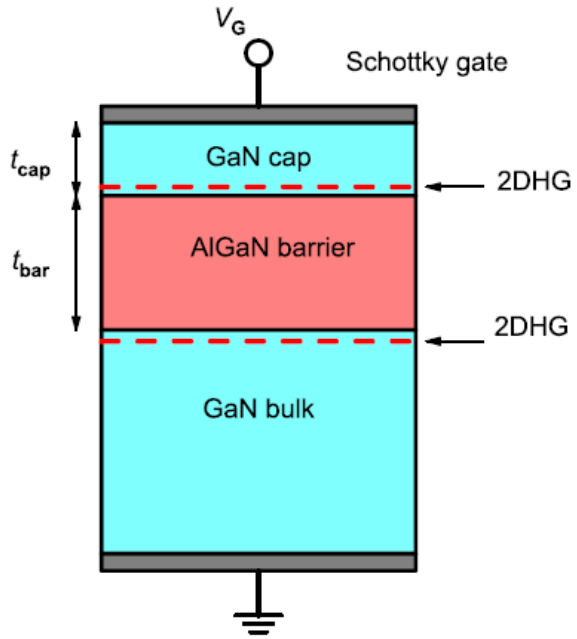


Figure **4.1.** Schematic of investigated GaN/AlGaN/GaN structures.

Table 4.1 summarizes important parameters for GaN and $Al_{0.3}Ga_{0.7}N$ used in the simulations. According to [10, 101], the spontaneous and piezoelectric polarizations result in a bound polarization charge density of $-1.39\times10^{13}$ $cm^{-2}$ at the upper GaN/AlGaN interface (cap/barrier) and $1.39\times10^{13}$ $cm^{-2}$ at the lower AlGaN/GaN (barrier/bulk) interface.

| Material | $\varepsilon_r$ | $m_{\parallel}^*$ | $m_{\perp}^*$ | $m_h$ | $E_G$ | $\Delta E_C$ | $P^{SP}$ | $P^{PZ}$ |
|---|---|---|---|---|---|---|---|---|
| GaN | 10.28 | 0.186 | 0.209 | 1.50 | 3.42 | 0 | -0.034 | 0 |
| $Al_{0.3}Ga_{0.7}N$ | 10.29 | 0.227 | 0.245 | 3.228 | 4.023 | 0.38 | -0.04639 | -0.00983 |

Tab. 4.1. Important material parameters of GaN and $Al_{0.3}Ga_{0.7}N$ used in this work. The effective masses are in units of the electron rest mann $m_0$, the gap and the conduction band offset in eV, and the polarizations $P^{SP}$ and $P^{PZ}$ in C/m$^2$.

### 4.1.2.2. Results

Figure 4.2 shows the calculated band diagram, together with the electron and hole distributions, in a GaN/AlGaN/GaN heterostructure with $t_{cap}$ = 10 nm and $t_{bar}$ = 30 nm for a surface potential of 2.5 eV. According to Equ. 4-1, such a surface potential corresponds to an applied gate voltage of -1.5 V when assuming a Schottky barrier height of 1 eV. As can clearly be seen, under these conditions a 2DEG is formed in the GaN bulk close to the barrier/bulk heterojunction, and additionally a 2DHG appears in the cap close to the cap/barrier interface.

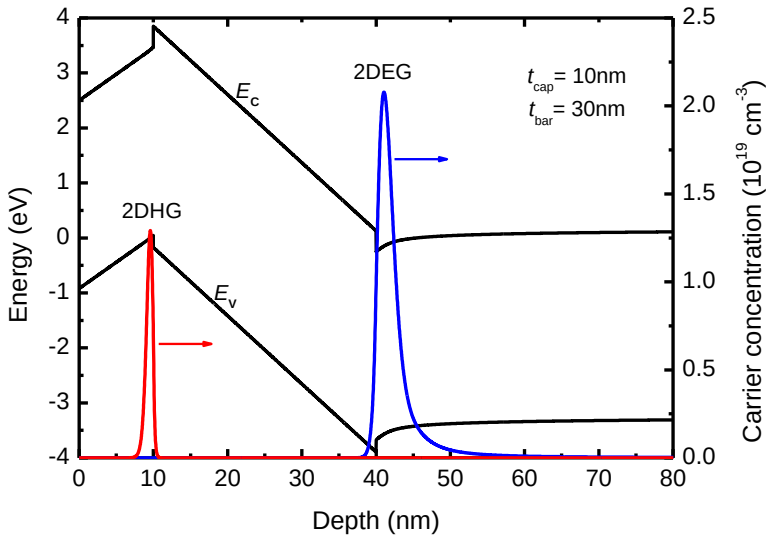


**Figure 4.2.** Calculated band diagram and free carrier distribution along the depth of a GaN/AlGaN/GaN structure with $t_{cap}$ = 10 nm and $t_{bar}$ = 30 nm for a surface potential of 2.5 eV. The reference energy is the Fermi level $E_F$.

Figure 4.3 shows the electron and hole distributions in the structure from Fig. 4.2 for different surface potentials. As expected, for increasing surface potential (i.e., for more negative gate voltages) the 2DEG becomes weaker and the peak electron concentration decreases from $3.4\times10^{19}$ cm$^{-3}$ for zero surface potential $E_{C0}$ down to $2\times10^{19}$ cm$^{-3}$ for $E_{C0}$ = 3 eV. The hole

density is affected by the surface potential as well. However, only for surface potentials significantly exceeding 2 eV a 2DHG will form in the GaN close to the barrier interface. For decreasing surface potential, the peak hole concentration rapidly drops from $3.35\times10^{19}$ cm$^{-3}$ for a surface potential of 3 eV down to $4\times10^{15}$ cm$^{-3}$ for $E_{C0}$ = 2 eV and $1.5\times10^{9}$ cm$^{-3}$ for $E_{C0}$ = 1.5 eV.

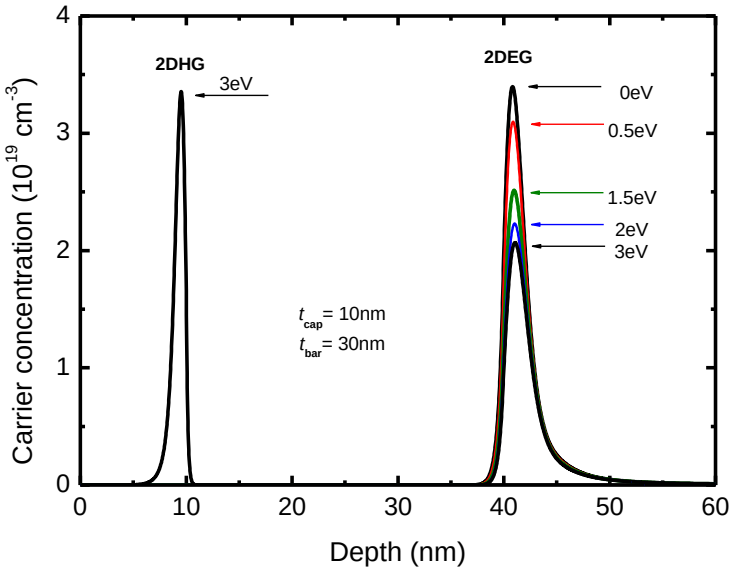


**Figure 4.3.** Electron and hole concentration profiles in the structure from Fig. 4.2 for different surface potentials.

Next we investigate the influence of the cap and barrier thicknesses on the formation of 2DEGs and 2DHGs. In a first simulation run, the cap thickness is varied while the barrier thickness is fixed to $t_{bar}$ = 20 nm. Figure 4.4 shows calculated 2DEG and 2DHG sheet densities of structures with different cap thicknesses as a function of the surface potential. As can be seen, increasing the cap thickness results in a lower 2DEG density and a higher 2DHG density for a given surface potential. Once a 2DHG starts to form (e.g., at $E_{C0} \approx 0.75$ eV for $t_{cap}$ = 40 nm), a further increase of the surface potential does no longer result in a decreasing 2DEG sheet density $n_S$. Instead, $n_S$ asymptotically approaches a saturation level while the 2DHG sheet density $p_S$ rises. The 2DHG is located closer to the surface (i.e., to gate) and therefore effectively shields the 2DEG located farther from the gate. As long as no 2DHG is yet formed, the slopes of the different $n_S(E_{C0})$ curves increase for decreasing cap thickness. The reason is the increasing gate capacitance for decreasing $t_{cap}$. Furthermore, the 2DEG sheet density becomes larger when the cap thickness is reduced.

Compared to the $n_S(E_{C0})$ curves, the corresponding $p_S(E_{C0})$ curves are much steeper, and a stronger dependence of the slope on $t_{cap}$ is observed. The reason is that the capacitive coupling between the gate and the 2DHG is stronger than that between the gate and the 2DEG since the distance gate-2DHG (i.e., $t_{cap}$) is smaller than the distance gate-2DEG (i.e., $t_{cap}+t_{bar}$). In the structures with the thinnest caps (2 nm and 5 nm), the 2DEG sheet density decreases continuously for increasing surface potential and no 2DHG is formed for surface potentials up to 3 eV.

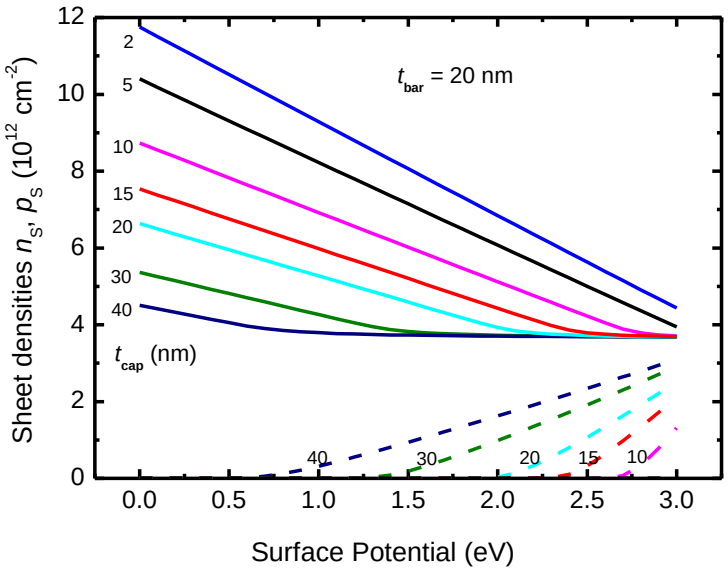


**Figure 4.4.** Calculated 2DEG and 2DHG sheet densities $n_S$ and $p_S$ as a function of the surface potential for GaN/AlGaN/GaN structures with a 20-nm barrier and different cap thicknesses. The numbers at the curves indicate the cap thickness in nm. Full lines: 2DEG sheet density. Dashed lines: 2DHG sheet density.

Next we keep the cap thickness constant ($t_{cap}$ = 10 nm) and vary the barrier thickness varied. The calculated 2DEG and 2DHG sheet densities are shown in figure 4.5. Regarding the effect of the barrier thickness on the sheet densities we observe a trend different from that related to the cap thickness. Thicker barriers lead to higher electron sheet densities and smaller slopes of the $n_S(E_{C0})$ curves for surface potentials where no 2DHG has yet formed. When for constant $t_{cap}$ the ratio $t_{bar}/t_{cap}$ becomes larger, the negative bound charge at the cap/barrier interface can less effectively reduce the 2DEG density. Furthermore, the enhanced gate capacitance leads to an increased slope of the $n_S(E_{C0})$ curves. Considering the $p_S(E_{C0})$ curves, the slope does not change with $t_{bar}$ since $t_{cap}$ is constant and the gate capacitance for the hole channel is constant as well. When the barrier is made thicker, the increase of $p_S$ is caused by a shift of the $p_S(E_{C0})$ curves towards smaller $E_{C0}$. In other words, in structures with thin barriers it is much more difficult to create a 2DHG even for large surface potentials.

As can be seen in figures 4.4 and 4.5, once a 2DHG starts to form, the 2DEG sheet density saturates and the gate voltage (and thus the surface potential) does no longer control the 2DEG sheet density. Obviously for each combination of cap and barrier thickness, a critical surface potential exists below which a 2DHG does not appear and above which a 2DHG with increasing sheet density and a saturated 2DEG coexist.

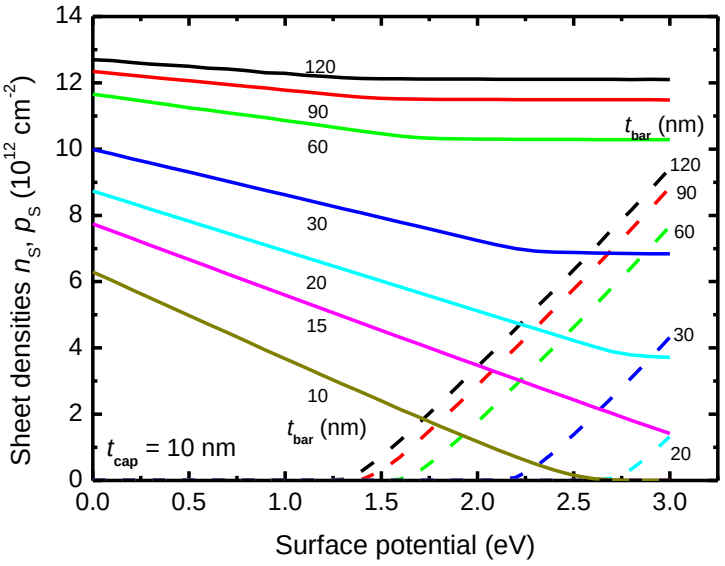


**Figure 4.5.** Calculated 2DEG and 2DHG sheet densities as a function of the surface potential for GaN/AlGaN/GaN structures with a 10-nm cap and different barrier thicknesses. The numbers at the curves indicate the barrier thickness in nm. Full lines: 2DEG sheet density. Dashed lines: 2DHG sheet density.

Furthermore we see from figures 4.4 and 4.5 that the saturation value of $n_S$ increases with increasing $t_{bar}$, but is independent of the cap thickness. Unfortunately, there is no simple explanation for this behaviour. We therefore have to consider the electrostatics of the GaN/AlGaN/GaN heterostructure in more detail with the model described in the next section.

### 4.1.3. Analytical Considerations

#### 4.1.3.1. Model

One can gain further insights into the conditions for the hole gas formation by considering the electrostatics of a GaN/AlGaN/GaN heterostructure with the help of simple first-order analytical considerations. Let us first take the simplified electrostatic arrangement of a GaN/AlGaN/GaN structure as shown in figure 4.6, where the GaN cap and the AlGaN barrier are assumed fully depleted from mobile carriers and a 2DEG is formed directly at the

barrier/bulk interface between barrier and bulk. In order to model the conditions for the formation of a 2DHG, the potential at the cap/barrier interface, $\varphi_{\text{cap}}$ (given in Volt), is considered. It can be modeled as the superposition of two separate contributions. The first contribution is the potential component $\varphi_{\text{cap}}^{\text{pol}}$ caused by the effect of the polarization charge and the second one is the potential component $\varphi_{\text{cap}}^{0}$ resulting from the effect of the applied surface potential:

$$\varphi_{\text{cap}} = \varphi_{\text{cap}}^{0} + \varphi_{\text{cap}}^{\text{pol}} \qquad 4\text{-}2$$

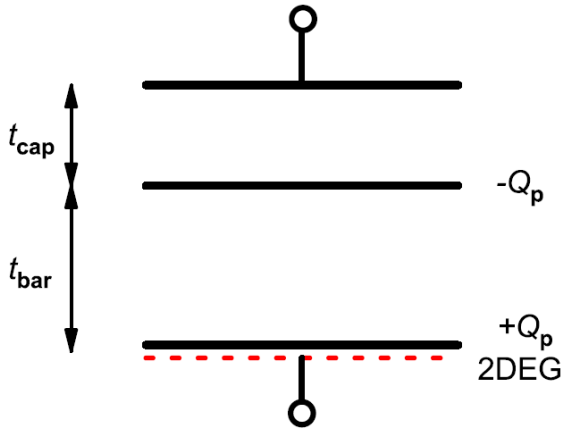


**Figure 4.6.** Simplified arrangement of the GaN/AlGaN/GaN structure.

In order to estimate $\varphi_{\text{cap}}^{\text{pol}}$, let us start with the case of zero applied surface potential, i.e. $E_{C0} = 0$. The appropriate equivalent circuit for this condition is shown in figure 4.7(a). The bound polarization charge $-Q_p$ at the cap/barrier interface induces the counter charges $Q_1$ at the gate and $Q_2$ in the 2DEG. From charge partitioning in parallel connected capacitances we find

$$Q_1 = -Q_p \frac{C_1}{C_1 + C_2} \quad \text{and} \quad Q_2 = -Q_p \frac{C_2}{C_1 + C_2} \qquad 4\text{-}3$$

where $C_1 = \varepsilon_{\text{cap}} / t_{\text{cap}}$ and $C_2 = \varepsilon_{\text{bar}} / t_{\text{bar}}$ are the depletion capacitances of the cap and the barrier per unit gate area. Knowing $Q_1$ and $Q_2$, the potential $\varphi_{\text{cap}}^{\text{pol}}$ can be easily obtained from

$$\varphi_{\text{cap}}^{\text{pol}} = \frac{Q_1}{C_1} = \frac{Q_2}{C_2} = \frac{-Q_p}{C_1 + C_2} \qquad 4\text{-}4$$

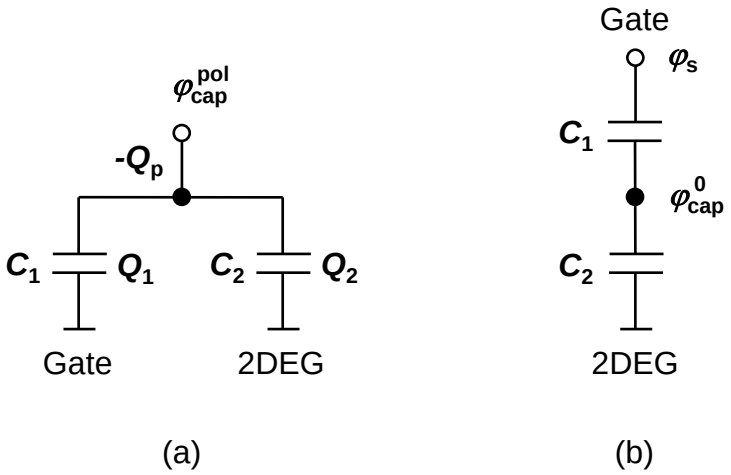


**Figure 4.7.** Equivalent circuit of a GaN/AlGaN/GaN structure for (a) zero surface potential applied and (b) a non-zero surface potential $E_{C0}$ applied (that corresponds to an applied gate voltage $V_G = -E_{C0}/q$).

Let us now consider the case $Q_p = 0$, where the potential $\varphi_{cap}^{0}$ is observed at the interface cap/barrier. From the equivalent circuit shown in Figure. 4.7(b), $\varphi_{cap}^{0}$ is easily found to be

$$\varphi_{cap}^{0} = \varphi_S \frac{C_1}{C_1 + C_2} = -\frac{E_{C0}}{q} \frac{C_1}{C_1 + C_2} \qquad 4\text{-}5$$

where $\varphi_S = -E_{C0}/q$ is the surface potential (given in Volt) and $E_{C0}$ is the conduction band edge at the surface (given in eV). Combining 4-2 with 4-4 and 4-5 leads to an expression for $\varphi_{cap}$ that reads as

$$\varphi_{cap} = \varphi_S \frac{C_1}{C_1 + C_2} - \frac{Q_p}{C_1 + C_2} \qquad 4\text{-}6$$

The electron sheet charge of the 2DEG consists of three components, namely the electron charge induced by the polarization charge $Q_p$ located at the interface barrier/bulk, the charge $Q_2$ induced by the negative polarization charge at the cap/barrier interface, and the charge induced by the applied surface potential given by $\varphi_S \times C_G$:

$$qn_S = Q_p + Q_2 + \varphi_S C_G \qquad 4\text{-}7$$

According to Figure 4.7(b), the gate capacitance $C_G$ is the given by

$$C_{\mathrm{G}} = \frac{C_1 C_2}{C_1 + C_2} \qquad \text{4-8}$$

Inserting 4-3 and 4-8 into 4-7, we get the following expression for the electron sheet charge

$$qn_{\mathrm{S}} = Q_{\mathrm{p}} \frac{C_1}{C_1 + C_2} + \varphi_{\mathrm{S}} \frac{C_1 C_2}{C_1 + C_2} \qquad \text{4-9}$$

A 2DHG is formed when the valence band edge at the cap/barrier interface touches the Fermi level $E_{\mathrm{F}}$ located at zero energy in Figure. 4.2. In other words, the condition for the formation of a 2DHG is

$$\varphi_{\mathrm{cap}} = -\frac{E_{\mathrm{G}}^{\mathrm{cap}}}{q} \qquad \text{4-10}$$

Equating 4-6 and 4-10, we find an expression for the critical surface potential at which a 2DHG just starts to form

$$\varphi_{\mathrm{S}}^{\mathrm{crit}} = -\frac{E_{\mathrm{C0}}^{\mathrm{crit}}}{q} = \frac{Q_{\mathrm{p}}}{C_1} - \frac{E_{\mathrm{G}}^{\mathrm{cap}}}{q} \frac{C_1 + C_2}{C_1} \qquad \text{4-11}$$

Assuming identical dielectric constants for GaN and AlGaN, which is a good approximation as can be seen from Tab. 4.1, eq. 4-11 can be simplified to

$$\frac{E_{\mathrm{C0}}^{\mathrm{crit}}}{q} = -Q_{\mathrm{p}} \frac{t_{\mathrm{cap}}}{\varepsilon_{\mathrm{cap}}} + \frac{E_{\mathrm{G}}^{\mathrm{cap}}}{q} \cdot \frac{t_{\mathrm{cap}} + t_{\mathrm{bar}}}{t_{\mathrm{bar}}} \qquad \text{4-12}$$

Using 4-12, for arbitrary cap and barrier thicknesses the critical surface potential (and thus the gate voltage) for the onset of the formation of a 2DHG can be estimated.

#### 4.1.3.2. Results

According to eq. 4-12, the critical surface potential $E_{\mathrm{C0}}^{\mathrm{crit}}$ (at which a 2DHG starts to form) depends linearly on the cap thickness. This is in excellent agreement with the results from Schrödinger-Poisson simulations, as can be seen in Figure 4.8. Moreover, Figure 4.9 shows that the nonlinear dependence of $E_{\mathrm{C0}}^{\mathrm{crit}}$ on the barrier thickness $t_{\mathrm{bar}}$ obtained from Schrödinger-Poisson simulations is well reproduced by eq. 4-12 as well.

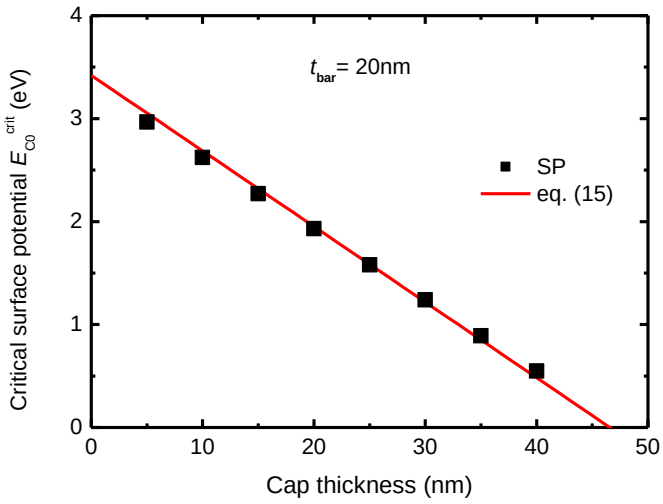


**Figure 4.8**. Critical surface potential as a function of cap thickness for a GaN/AlGaN/GaN structure with 20-nm barrier. Symbols: results from Schrödinger-Poisson (SP) simulations. Line: calculated from eq. 4-12.

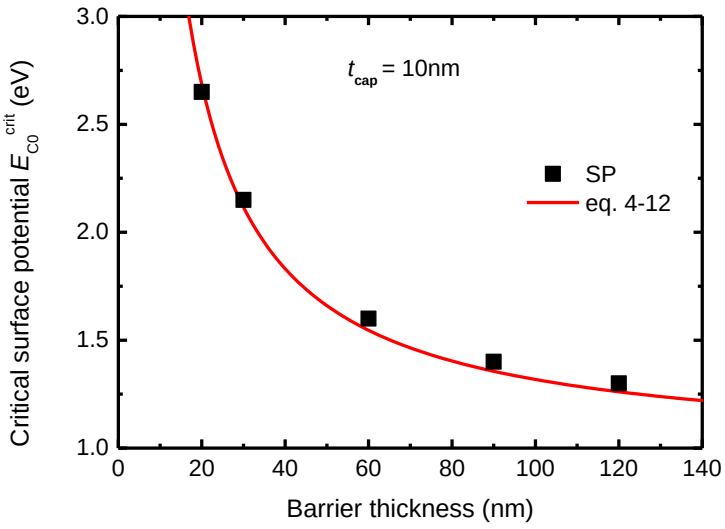


**Figure 4.9**. Critical surface potential as a function of barrier thickness for a GaN/AlGaN/GaN structure with 10-nm cap. Symbols: results from Schrödinger-Poisson simulations. Line: calculated from eq. 4-12.

From Figures 4.4 and 4.5 it turned out that $n_S$ saturates when a 2DHG starts to form. The saturation value $n_S^{sat}$ can be modeled with 4-9 using the value for $\varphi_S^{crit}$ from 4-11 as

$$n_S^{sat} = \frac{Q_p}{q} - \frac{E_G^{cap}}{q^2} C_2 = \frac{Q_p}{q} - \frac{E_G^{cap}}{q^2} \frac{\varepsilon_{bar}}{t_{bar}} \qquad 4\text{-}13$$

The saturation value $n_S^{sat}$ is independent of the cap thickness, which is in agreement with the Schrödinger-Poisson results shown in Figure 4.4. Figure 4.10 compares the 2DEG saturation sheet density $n_S^{sat}$ obtained from Schrödinger-Poisson simulations with those calculated using eq. 4-13. Again, the analytical model describes the dependence of the saturation electron density on barrier thickness very good.

As can be seen from Figure 4.10, $n_S^{sat}$ vanishes for a barrier thickness of 14 nm. For $t_{bar}$ < 14 nm, eq. 4-13 would yield negative values for $n_S^{sat}$, which do not have a physical meaning. In such cases, the electron density does not saturate at all since no 2DHG can be formed anymore. This is in good agreement with Figure 4.5, where no noteworthy hole density can be observed for $t_{bar}$ < 15nm. The minimum barrier thickness, for which it is possible to form simultaneously a 2DHG and a 2DEG, can be obtained from eq. 4-13 for $n_S^{sat} = 0$ as

$$t_{bar}^{min} = \frac{E_G^{cap}}{q}\frac{\varepsilon_{barrier}}{Q_p} \qquad 4\text{-}14$$

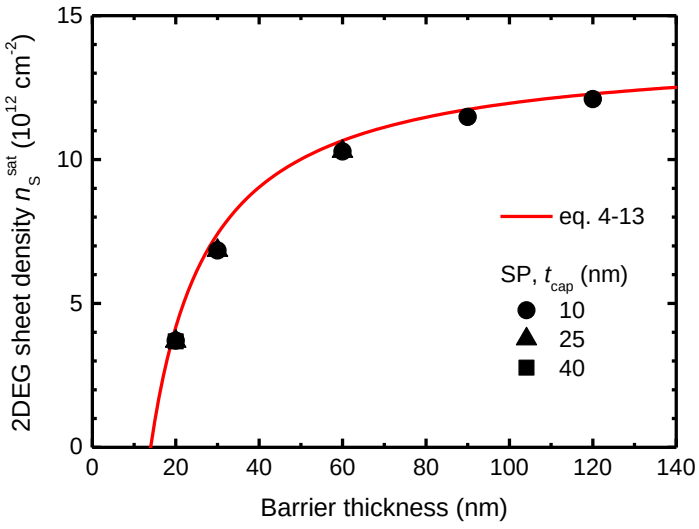


**Figure 4.10.** $n_S^{sat}$ obtained from Schrödinger-Poisson simulations (symbols) and calculated using eq. 4-13 (line) as a function of barrier thickness.

The above equation can be used to design appropriate heterostructures for certain applications. For instance, if a saturation of $n_S$ is undesirable, e.g. for HEMTs, $t_{bar}$ should be smaller than $t_{bar}^{min}$. In such cases one could increase $t_{bar}^{min}$ by reducing the polarization charge, i.e. by reducing

the Al content in the barrier. In BiSFET-like structures [97], coexisting electron and hole gases separated by a thin barrier (thin enough to allow tunnelling) are needed. In that case, a small $t_{\mathrm{bar}}^{\mathrm{min}}$ is necessary that can be achieved either by increasing $Q_{\mathrm{p}}$ (by raising the Al content of the barrier) or by moving to another material system with more narrow bandgaps, such as InN/InGaN.

### 4.1.4. Conclusion

The formation of 2DHGs in GaN/AlGaN/GaN heterostructures has been investigated theoretically by numerical simulation and a new analytical model developed in the present work. It has been shown that for certain combinations of bias conditions and layer design coexisting 2DEGs and 2DHG are formed in the structure where the 2DHG is located at the cap/barrier interface and the 2DEG is at the barrier/bulk interface. Once a 2DHG is created, the effect of the gate voltage on the 2DEG diminishes rapidly and a saturation of the 2DEG density is observed.

## 4.2. Theoretical investigation of enhancement/depletion-mode double channel AlGaN/GaN HEMTs logic, using a novel vertical design

Owing to the unique properties of GaN such as wide bandgap and good electron transport properties, GaN HEMTs are very promising for the construction of ICs to perform reliable operations at high temperature that have not be possible for silicon- or GaAs-based technologies [55,56,102]. The high-temperature digital ICs can provide the enabling technology for intelligent control and sensing units used in harsh environments such as high temperatures or abrasive chemicals [103]. It can be shown that by integrating Enhancement/Depletion-mode (E/D-mode) AlGaN/GaN HEMTs together, a major advantage for low dissipation power digital circuits can be achieved [56,57].

In this section, it will employ the 2DEG that occurs in AlGaN/GaN heterostructure in AlGaN/GaN/AlGaN/GaN multilayer to design a novel technique using double channel (vertical design) HEMTs where both channels work independently. Then this technique has been applied to achieve both E-mode and D-mode HEMTs and a logic device that uses the separation channels has been described. Finally, this work will attempt to characterize and model the properties of the two 2DEG layers at the interface of AlGaN and GaN to better understand this unique phenomenon in order to optimize devices design. Options to enhance the performance for proper Inverter operation are presented. Finally, the reported separation channel technology is potentially suitable for fabrication of low power and cost GaN logic circuits.

However, double channel devices made of the AlGaN/GaN/AlGaN/GaN multilayer have described in ref. [104] and show unique capabilities of achieving high current drive, low buffer leakage, and high cut-off frequencies.

The chapter is organized as follows. In Sec. 4.2.2, the studied structures, the simulation approach, and the used material parameters are presented. In Sec. 4.2.3, the simulated results are presented. In Sec. 4.2.4, considerations and results for AlGaN/GaN HEMTs Inverter are presented and discussed. And finally Sec. 4.2.5 summarizes the chapter.

### 4.2.1. Studied structures and modelling

Figure 4.11 shows the schematic cross-sectional view of the proposed channels separation technique. The main concept of this technique is sequences of channels and barriers. In this study we focus on two channels with four layers from bottom to top GaN as first channel, AlGaN as first barrier, GaN as second channel and AlGaN as second barrier. The calculation is

taking in an account Ga-face AlGaN/GAN polarisation induced charge, and GaN layers are considered fully relaxed and the others are considered fully strained and all layers are assumed to be undoped.

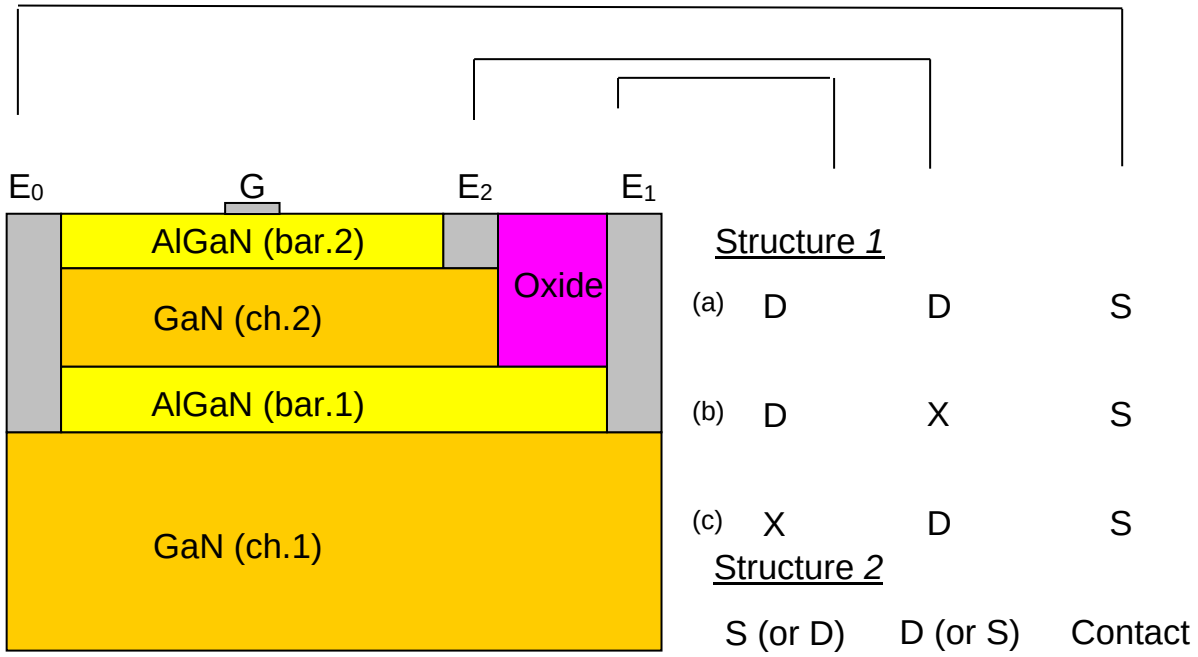


**Figure 4.11.** The 2D heterostructures considered in the ATLAS simulations. Structure 1: Three different cases of transistors are considered a) overall case $E_0$=S and $E_1$=$E_2$=$D_2$ b) $E_0$=S, $E_1$=D and $E_2$=off transistor are working at lower channel c) $E_0$=S, $E_2$=D and $E_1$=off transistor are working at upper channel and both channels respectively). Structure 2: two transistors in series, $E_0$=Contact, $E_2$=D (or S) and $E_1$=S (or D). Where, S= Source and D= Drain.

The polarization bound charges at the interfaces are calculated using the models from [10]. For Al- content x = 0.18, 0.27 and 0.35, the polarization bound charge density for AlGaN/GaN interfaces is $7.66\times10^{12}$q/cm$^2$, $1.22\times10^{13}$q/cm$^2$ and $1.67\times10^{13}$q/cm$^2$ respectively.

Table 4.2 summarizes important parameters for GaN and $Al_xGa_{1-x}N$ used in the simulations

| Material | $\varepsilon_r$ | $m_{\parallel}^*$ | $m_{\perp}^*$ | $E_G$ | $\Delta E_C$ | $P_{SP}$ | $P_{PZ}$ |
|---|---|---|---|---|---|---|---|
| GaN | 10.28 | 0.186 | 0.209 | 3.42 | 0 | -0.034 | 0 |
| $Al_{0.18}Ga_{0.82}N$ | 10.29 | 0.210 | 0.231 | 3.760 | 0.214 | -0.04098 | -0.00529 |
| $Al_{0.27}Ga_{0.73}N$ | 10.29 | 0.223 | 0.241 | 3.955 | 0.337 | -0.04498 | -0.00862 |
| $Al_{0.35}Ga_{0.65}N$ | 10.29 | 0.234 | 0.251 | 4.141 | 0.454 | -0.04882 | -0.01196 |

| Material | $\varepsilon_r$ | $m_{\parallel}^*$ | $m_{\perp}^*$ | $E_G$ | $\Delta E_C$ |
|---|---|---|---|---|---|
| $Al_2O_3$ | 10 | 0.400 | 0.500 | 8.8 | 2.8 |

Tab. 4.2. Important material parameters used in this work. The effective masses are given in units of the electron rest mass $m_0$, the gap and the conduction band offset in eV, and the polarizations $P_{SP}$ and $P_{PZ}$ in $C/m^2$. a) For GaN and AlGaN b) for $Al_2O_3$ [9,10].

As can be seen in Figure. 4.11, the procedure to separate every channel is by putting the electrodes $E_1$ and $E_2$ for every channel separately. This strategy gives possibility to,: 1) The source and the drain in the opposite side, or 2) The source and the drain in the same side compared to the gate. In the first structure 1), it will be take in our study three clear cases: (a) the overall case, where are the $E_1$ and $E_2$ at same voltage $V_D$ and called this contacts (drain contact) and $E_0$=S, (b) transistor operation on only lower channel, $E_1$=D and $E_2$ = open circuit, and (c) transistor operation on only upper channel, $E_1$ = open circuit and $E_2$=D. The second structure 2), where the channels combine together across a contact, i. e. from the Figure 4.11, $E_1$=S (or D) and $E_2$ = D (or S) and the source connects to drain across $E_0$ contact.

The characteristics of this technique are described with two dimensional ATLAS simulations. Physical based models that describe the properties of the materials and a detailed description of the specific channels separation technique GaN HEMT structure definition and geometries are written by the author in input ATLAS syntax.

### 4.2.2. Results and discussion

Figure. 4.12 shows simulated transfer characteristics of the channels separation technique GaN HEMTs for all cases of the structure (1) are $t_{bar.1}$= 20nm, $x_{bar.1}$=0.35, $t_{bar.2}$= 5nm and $x_{bar.2}$= 0.27 and drain-source voltage 3 volt and $L_{GD}$= 15µm.

As can be seen, the overall case with an unique current–voltage transfer characteristic is remarkable, where unlike conventional single-channel GaN HEMTs, drain current can be flow in two steps. We can introduce several characteristic parameters, the overall threshold voltage or the threshold voltage of the first step also ($V_{th1}$), the saturation voltage and the threshold voltage of the first step ($V_{th2}$). We linearly extrapolate the $I_D$(sat) level between these two steps and define the transition between saturation (between these two steps) and on-state of first step at the intersection of the two extrapolations as the saturation point of the HEMT. The gate voltage at this point is designated as $V_{G\text{-}sat}$ and the corresponding drain current as $I_{D\text{-}sat}$.

Using the parameters introduced above, we can define the following four distinct operating regions: (a) transistor off-state between extreme negative voltage and $V_{th1}$, in this case both lower and upper channels are in off-state (b) linear transistor operation between $V_{th1}$ and $V_{G,sat}$, in this case only the lower channel is in on-state (c) semi saturation region between $V_{G,sat}$ and $V_{th2}$, in this case the lower is saturate and upper channel is in off-state (d) linear transistor operation between $V_G > V_{th2}$, in this case the lower is saturate and upper channel is in on-state.

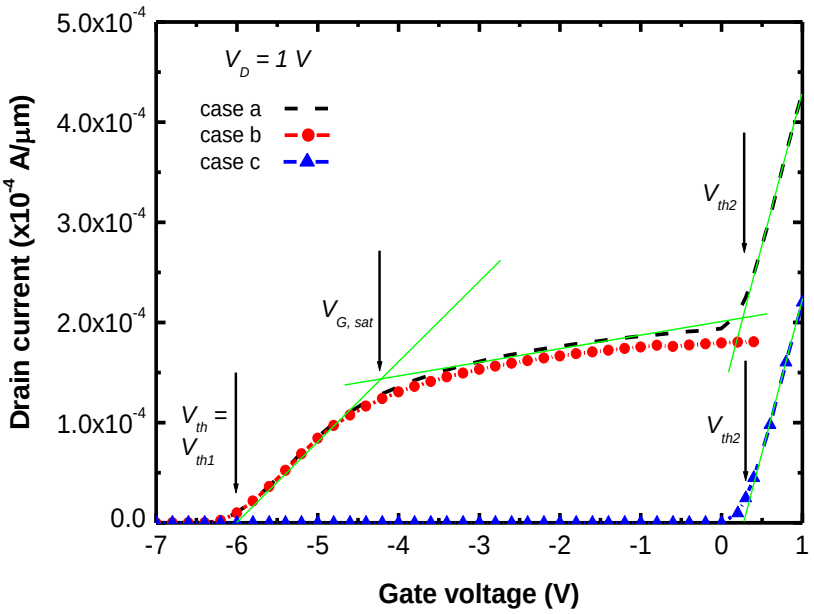


**Figure 4.12 .** Calculated transfer characteristics of structure 1 a) overall case, b) the transistor works on the lower channel and c) the transistor works on the upper and with 20 nm and $x_{bar1}$= 0.35 bar.1 layer, 5 nm and $x_{bar1}$= 0.27 bar.2 layer and 200nm ch.2 layer thickness.

By depends on these operating regions, we obvious in Figure 4.12: 1) Kind of saturation between these two steps. 2) The overall case has the threshold voltage of case (b) ($V_{th1}$). This means, that the lower channel determined the threshold voltage of overall case. Fortunately, the start value of the second step (case (c)) is determined the threshold voltage of upper channel ($V_{th2}$).

The reason of these observed two slops (jumps) is as a result of formation of additional channels at the interfaces upper the main channel. Figure 4.13 is the calculated band diagram, together with the electron and hole distributions, for the AlGaN/GaN/AlGaN/GaN heterostructure with $t_{bar1}$= 10nm (a) and 20nm (b) and $t_{ch2}$ and $t_{bar2}$ 40nm and 5nm respectively for gate voltages of 0eV and 1eV.

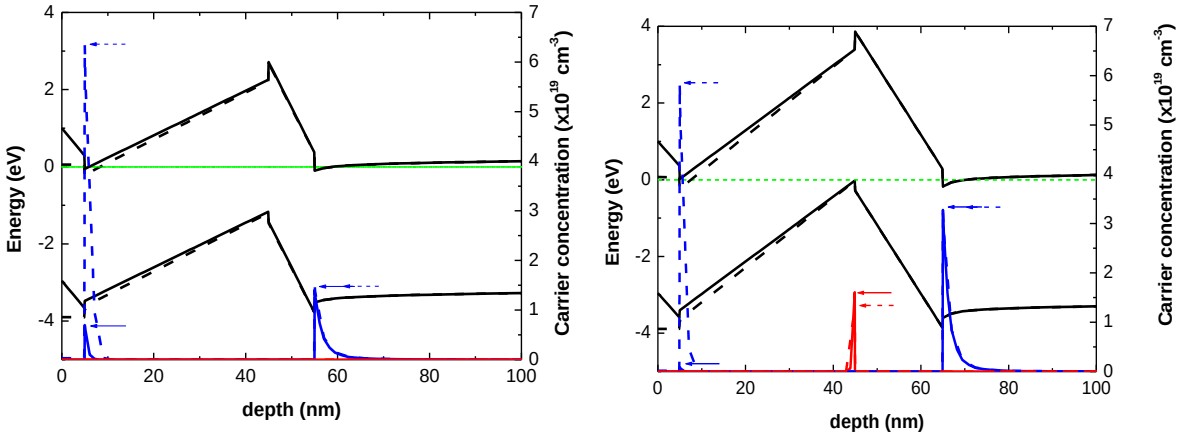


**(a)** **(b)**

**Figure 4.13.** Band Diagram and hole concentration of channels separation technique HEMT underneath the gate for structure 1(a) with $t_{ch2}$ =40nm, $t_{bar2}$ =3nm and $t_{bar1}$ = a) 10nm and b) 20nm, at $V_G$ = 0 Volt (without contact metal) and $V_G$ = 1 Volt (with contact metal).

As can be seen from the calculated band diagram in Figure 4.13, together with the electron distributions of the vertical cut under the gate, the conduction band (valance band) edge at the bar.1/ch1 and bar.2/ch2 (ch2/bar1) interface is in minimum (maximum) value in and close to the interface, and at considered surface potential becomes below (up) the Fermi level $E_F$. And where the interface is populated by positive ions $+Q_p$ ($-Q_p$), the negative electron (positive hole) charge in tends to compensate the positive charge (negative charge) of the ionized interface, which leads to the observed saturation of the 2DEG density $n_{S\text{-}2DEG}$ for the lower channel and awake these two slopes in $I_D(V_G)$-curves. Since the second electron channel is located closer to the gate electrode than the 2DEG at the barrier1/ch1 heterojunction, the gate capacitance, which is inversely proportional to the distance between gate and channel, becomes larger when the second electron channel is formed. This explains the visible increase of the slope of the overall $n_s$ ($E_{C0}$) curves in Figures. 4.12 once $n_{S\text{-}2DEG}$ saturates.

Moreover, a hole channel is formed approximately after critical bar.1 thickness. Such an effect has already been observed for hexagonal GaN/AlGaN/GaN heterostructures [77]. Due to the smaller thickness of bar1 (> 14 nm for the barrier with Al-content of 0.30), there is no chance to form a 2DHG.

It should be noted that, due to the additional AlGaN barrier , there is two regions with a kind of separation between them.

We can decrease this discontinuity or separation by using a proper lower AlGaN barrier layer, where small layer thickness and low Al composition was proven to be an effective approach to implement the double-channel HEMT with the second channel of high electron density and acceptable access resistance [104], or by decreasing source - drain distance to decrease spacing resistance.

To make a fair study to this considerable technique, let us take the effects of some geometric parameters on this unique transfer characteristic.

Figure 4.14 shows $I_D(V_G)$-curves for structure 1(a) with 20nm and 5nm bar.1 and bar.2 thicknesses respectively and with 0.35nm and 0.27 Al-content and the ch.2 thickness $t_{ch2}$ have been varied from 10nm (smaller than critical value to formation 2DHG) to 80nm (larger than critical value to formation 2DHG).

As shown in Figure 4.14, the slope of the $I_D(V_G)$-curves in region a is decrease by increasing the channel 2 thickness with the same threshold voltage $V_{th}$ and nearly the same efficient range of the channel 1, i.e. outside this range the lower channel become inefficient.

On the other hand, the slope of the $I_D(V_G)$-curves in region c is increased by decreasing the channel 2 thickness and with decrease the threshold voltage $V_{th2}$ and decrease the efficient range of the channel 2, i.e. outside this range the upper channel become inefficient.

It should be noted that the gate potential has better control of the upper channel (nearest to the gate contact), However, the observed saturation in the channel 1 layer leads to a degradation of the slope (transconductance), and hence to a significant deterioration of the channel 1. Thus, the usable operation range of the applied surface potential will be limited.

Another note is, there is a kind of saturation. We can make this saturation more flat by 1) increasing channel 2 layer thickness, where this leads to increasing in formation of 2DHG, that lead to a weak control of lower channel or 2) increasing source-drain distance, the main reason of saturation in the channel, where this leads to increase in source-drain resistance or a more flat slope.

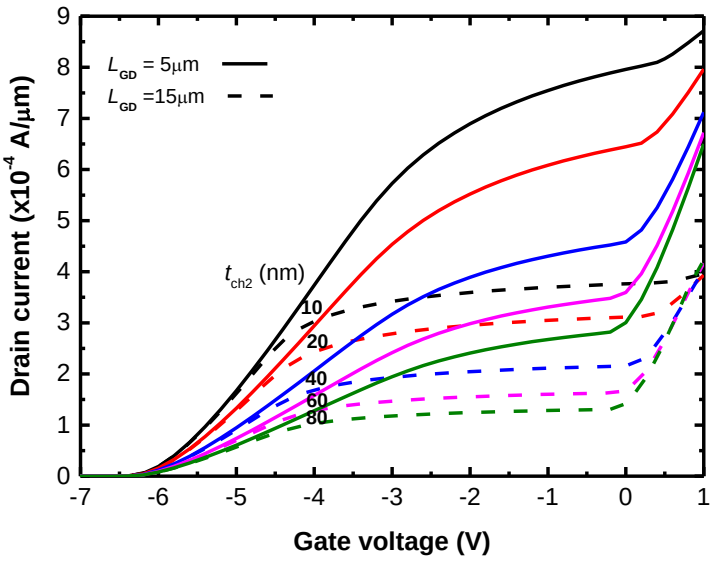


**Figure 4.14.** Calculated transfer characteristics of structure 1 (a) for two different gate-drain distance 5 and 15 μm and with 20 nm and $x_{bar1}$= 0.35 barrier 1 layer, 5 nm and $x_{bar1}$= 0.27 barrier 2 layer and different channel 2 layer. The numbers at the curves indicate the channel 2 thickness ($t_{ch2}$) in nm.

Another factor can be modified, the Al-content of bar.2. Figure 4.15 shows $I_D(V_G)$-curves for structure 4.11(a) with 20nm, 0.35 Al-content and 5nm bar.1 and bar.2 thicknesses respectively and with the ch.2 thickness 40nm and Al-content of bar.2 have been varied.

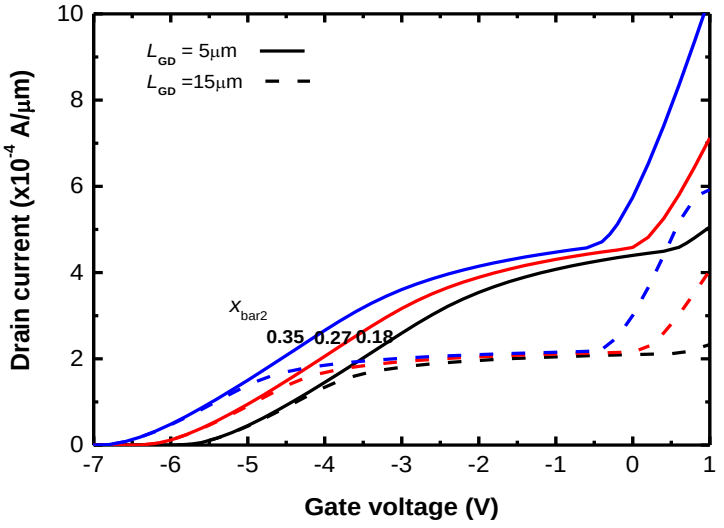


**Figure 4.15.** Calculated transfer characteristics of structure 1 (a) for two different gate-drain distance 5 and 15 μm and with 20 nm and $x_{bar1}$= 0.35 barrier 1 layer, 40nm channel 2 layer and different Al-content barrier 2 of 5nm thickness. The numbers at the curves indicate the barrier 2 Al-content ($x_{bar2}$).

As shown in Figure 4.15, the $I_D(V_G)$-curves are shifted towards more negative values by increasing the Al-content of barrier 2 with constant slope. On the other hand, the slope of the $I_D(V_G)$-curves in region c is decrease by increasing the Al-content of barrier 2 with decreasing threshold voltage $V_{th2}$.

Important parameter ought to be adjusted, the thickness of barrier 1 to vanishes or increase 2DHG the main reason of discontinuity of efficiency and to achieve a faster transistor (by vanishes 2DHG). Figure 4.16 shows $I_D(V_G)$ curves for structure 4.11(a) with 5nm and 0.27 Al-content of barrier 2, 40nm channel 2 and the barrier 1 thickness have been varied.

As shown in Figure 4.16, the $I_D(V_G)$-curves are shifted towards more negative values by increasing barrier 1 thickness with nearly conserved the slope and the efficient range of the region a and more negative threshold voltage. On the other hand, the slope of the $I_D(V_G)$-curves in region c is decreased by increasing the barrier 1 thickness with nearly same threshold voltage $V_{th2}$ and efficient range of the channel 2. I.e. the region b extends by increasing the barrier 1 thickness.

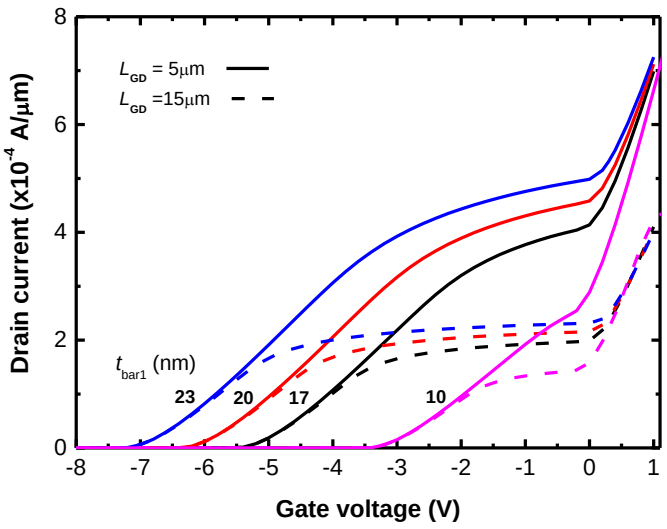


**Figure 4.16.** Calculated transfer characteristics of structure 1 (a) for two different gate-drain distance 5 and 15 µm and with 5 nm and $x_{bar2}$= 0.27 barrier 2 layer, 40nm channel 2 layer and different barrier 1 thickness of $x_{bar1}$=0.35 Al-content. The numbers at the curves indicate the barrier 1 thickness ($t_{bar1}$) in nm.

The change of the barrier 2 thickness has an effect on the both channel's threshold voltage with the same slopes and effective range of efficiency. Figure 4.17 shows $I_D(V_G)$-curves for structure 4.11(a) with 20nm and 0.35 Al-content of barrier 1, 40nm channel 2 and the barrier 2 thickness

have been varied. As shown in Figure 4.17, the smallest barrier 2 thickness has the largest threshold voltages.

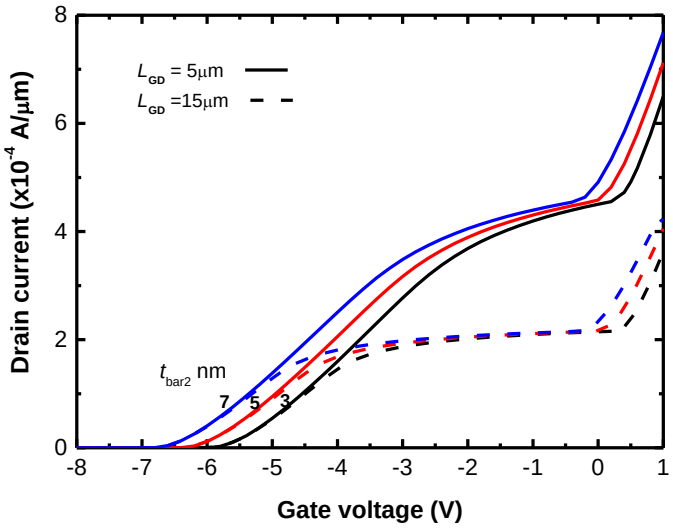


**Figure 4.17.** Calculated transfer characteristics of structure 1 (a) for two different gate-drain distance 5 and 15 μm and with 20 nm and $x_{bar1}$= 0.35 barrier 1 layer, 40nm channel 2 layer and different barrier 2 thickness of $x_{bar2}$=0.27 Al-content. The numbers at the curves indicate the barrier 2 thickness ($t_{bar2}$) in nm.

For all previous results, we can easily extract cases b and c for structure 4.11. The main obvious is the possibility to become normally-off mode for the upper channel by simply adjusting the thickness of the layers and Al-contents parameters.

### 4.2.3. Logic device, results and discussion

After we have presented our results for all cases of structure 4.11, we come now to the second structure, where the channels connected together across contact and the source and drain are at the same side compared to gate. It is easy to find that this configuration will work at the threshold voltage of the second channel and small slope of the $I_D(V_G)$-curves will be noted related to two resistance channels in series. Such design has the key to solve the integration problem of GaN-depended devices in logic circuits, where we have both cases, normally-on and normally-off in same design.

The first demonstration of enhancement/depletion (E/D)-mode integrated digital circuits in GaN technology has been reported by [56], where the publication describes low power digital devices and high power RF devices on the same chip. Figure 4.18 presents our structure (vertical structure) compare with equivalent horizontal structure. To get the horizontal structure,

we take the mirror of our structure, connect the contacts together. Now, we combine enhancement (structure 4.11(c)) transistor with depletion transistor (structure 4.11(b)) to become inverter characteristics. It is obvious, that our structure shows nearly the same characteristics. The advantage of our structure is using four terminal replace of six terminals in conventional GaN enhancement/depletion-mode FET logic i.e. simplest and lowest cost design.

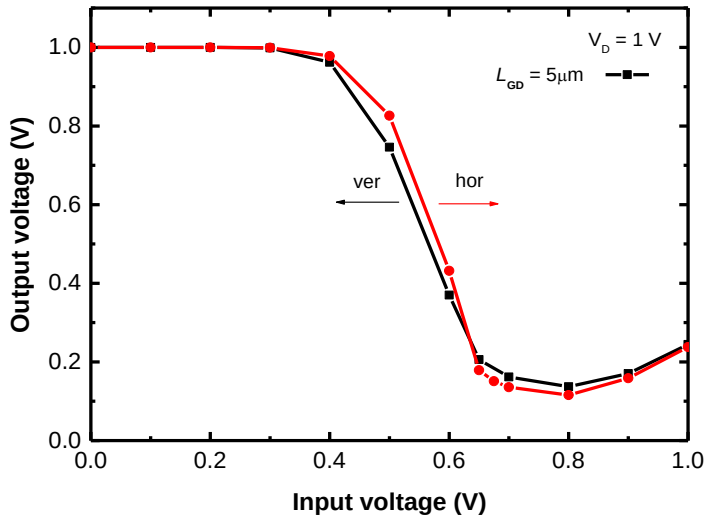


**Figure 4.18.** Calculated $V_{out}(V_{in})$-curves for a) our structure 2 and b) equivalent conventional E/D-mode inverter at drain-source voltage 1V with 7nm and $x_{bar1}$= 0.35 barrier 1 layer, 80nm channel 2 layer and 3nm and $x_{bar1}$= 0.18 barrier 2 layer.

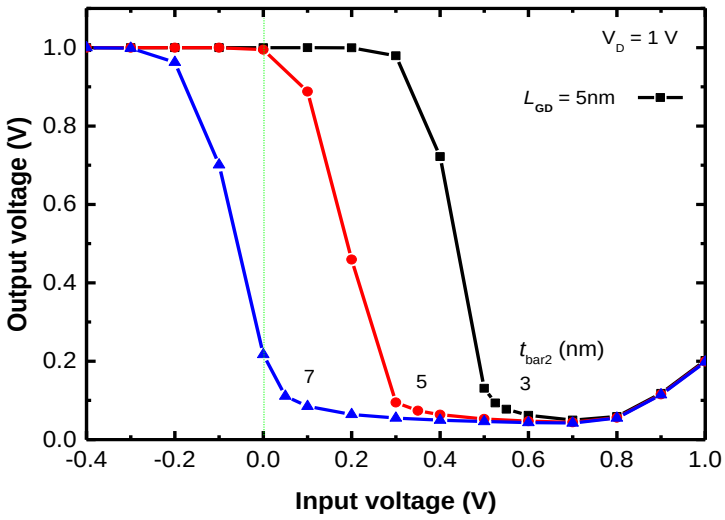


**Figure 4.19.** Calculated $V_{out}(V_{in})$-curves for our structure (structure 2) at drain-source voltage 1V with 7nm and $x_{bar1}$= 0.35 barrier 1 layer,200 channel 2 layer and $x_{bar1}$= 0.18 barrier 2 layer with varied thicknesses.

To make a fair study to this considerable technique, let us take the effects of some parameters on this novel inverter. Figure 4.19 shows $V_{out}(V_{in})$-curves for structure 4.12 with 7nm barrier 1 thickness with 0.35 Al-content and channel 2 thickness 200nm and 0.18 Al-content of barrier 2 thicknesses and the barrier 2 thickness $t_{bar2}$ have been varied from 3nm to 7nm.

As shown in Figure 4.19, the $V_{out}(V_{in})$-curves are shifted towards more positive values by increasing barrier 2 thickness with nearly constant both minimum output voltage (0.05V) and the slope of the curve between on/off.

To control the slope and the minimum output voltage of the *V*out(*V*in)-curves, we can change the thickness of channel 2. Figure 4.20 shows *V*out(*V*in)-curves for structure 4.12 with 7nm and 3nm barrier 1 and barrier 2 thicknesses respectively and with 0.35nm and 0.18 Al-content and the channel 2 thickness ($t_{ch2}$) have been varied from 40nm to 200nm.

As shown in Figure 4.20, the slope and the minimum output voltage of the $V_{out}(V_{in})$-curves is increase by increasing the channel 2 thickness, i.e. improvement features of the inverter. Fortunately, the increase in channel 2 thicknesses, give us advantage in manufacturing process to achieve the separation and do not have an effect on characteristics of transistor, while is the barrier 1 under the critical thickness

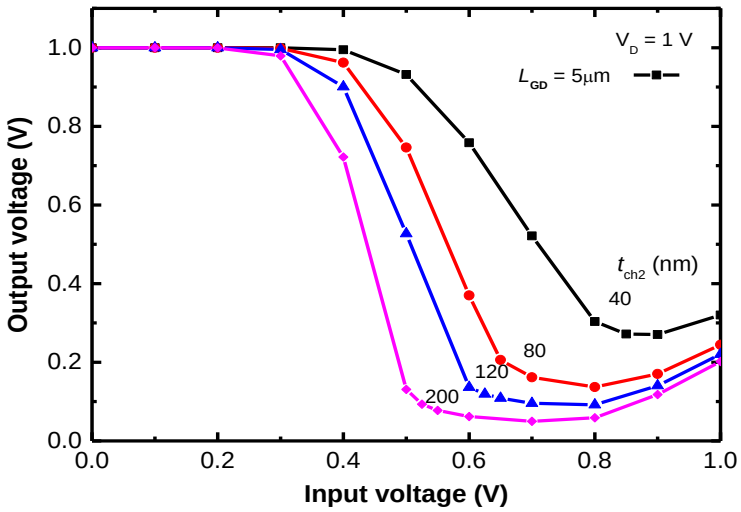


**Figure. 4.20.** Calculated $V_{out}(V_{in})$-curves for our structure (structure 2) at drain-source voltage 1V with 7nm and $x_{bar1}$= 0.35 barrier 1 layer, 3nm and $x_{bar2}$= 0.18 barrier 2 layer and channel 2 layer thicknesses from 40nm to 200nm are varied.

To decrease value of the minimum output voltage of the *V*out(*V*in)-curves, we can change the thickness of barrier. Figure 4.21 shows $V_{out}(V_{in})$-curves for structure 4.12 with 3nm barrier 2 thickness with 0.18 Al-content and channel 2 thickness 200nm and 0.35 Al-content of barrier 2 thicknesses and the barrier 2 thickness $t_{bar2}$ have been varied from 5nm to 7nm.

As shown in Figure 4.21, the minimum output voltage of the $V_{out}(V_{in})$-curves is decreased by decreasing the barrier 1 thickness, from 0.09V to 0.01V.

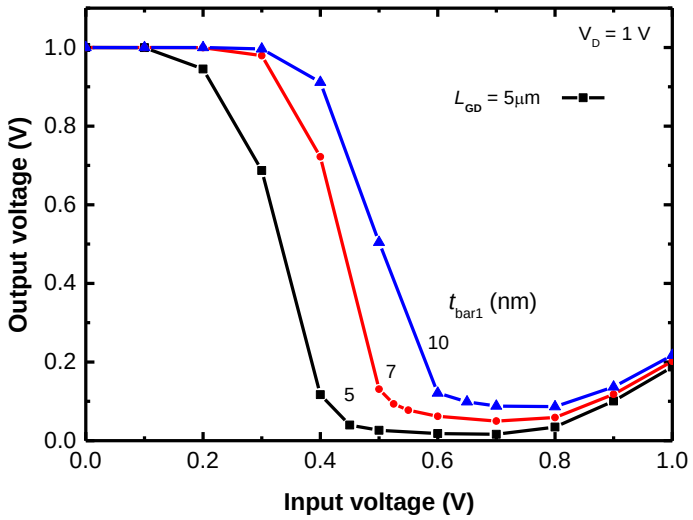


**Figure 4.21.** Calculated $V_{out}(V_{in})$-curves for our structure (structure 2) at drain-source voltage 1V with 3nm and $x_{bar1}$= 0.18 barrier 2 layer,200 channel 2 layer and $x_{bar1}$= 0.35 barrier 2 layer with varied thicknesses.

To avoid this undesirable arise in voltage, we put a thin cap to suppress the gate leakage the main reason of this phenomenon. Figure 4.22 shows $V_{out}(V_{in})$-curves for structure 2 with 7nm and 7nm barrier 1 and barrier 2 thicknesses respectively and with 0.35nm and 0.18 Al-content and 200nm channel 2 thickness and with and without cap.

As shown in Figure 4.19, the $V_{out}(V_{in})$-curves are shifted towards more positive values (inverter region) by putting the cap with nearly conserved the minimum output voltage (0.05V) and the slope of the curve between on/off, but without the undesirable awake up.

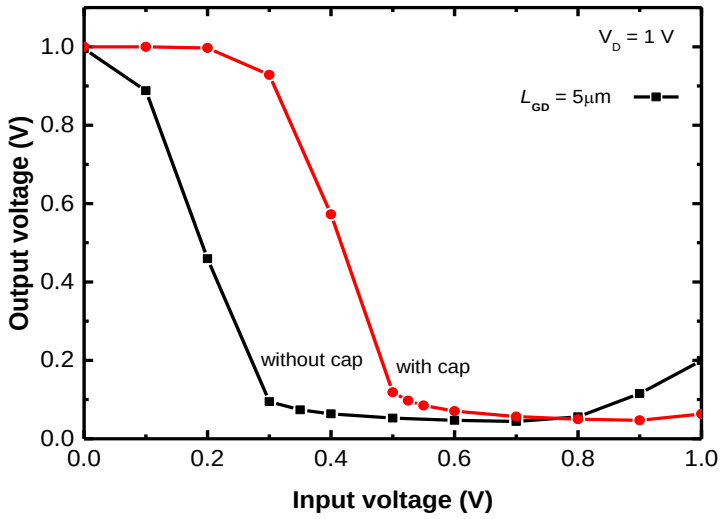


**Figure 4.22.** Calculated $V_{out}(V_{in})$-curves for our structure (structure 2) a) without cap and b) with GaN cape at drain-source voltage 1V with 7nm and $x_{bar1}$= 0.35 barrier 1 layer, 200nm channel 2 layer and 5nm and $x_{bar1}$= 0.18 barrier 2 layer.

### 4.2.4. Conclusion

The formation of second channel in AlGaN/GaN/AlGaN/GaN heterostructures has been investigated theoretically by numerical simulation. It has been shown that for certain combinations of bias conditions and layer design two coexisting channels can be formed in AlGaN/GaN/AlGaN/GaN structures where the both channels are located at the bar1/ch1 and bar2/ch2. Once a second channel is created, the effect of the gate voltage on the first 2DEG diminishes rapidly and a saturation of the drain current is observed. Special attention was paid to the structure 2 as a novel inverter.

# Chapter 5
# GaN MIS and GaN normally-off PNT HEMTs for power switches

## 5.1. Theoretical Investigations of AlGaN/GaN HEMT Structures for Power Switch Applications

### 5.1.1. Introduction

Group III-nitride based high electron mobility transistors (HEMTs) are suitable candidates for high-power electronics applications due to their high breakdown field, high-density and high-mobility two-dimensional electron gas (2DEG). The natural form of these GaN-based devices is a normally-on or depletion mode (D-mode) device. Despite these type of devices can be used in power semiconductor systems, however, normally-off operation is required to simplify the design of driving circuits. Several approaches or techniques have been proposed to obtained E-mode devices and they can be clustered in two main families: recessed gate MISHEMTs and p-GaN HEMTs [105-109]

The first approach (recessed gate MISHEMT) consists in (fully or partially) recessing the AlGaN barrier below the gate to interrupt the 2DEG thereby obtaining normally-off operation. This critical step is then followed by another key processing step that is the gate dielectric deposition.

The second approach (p-GaN HEMT) consists in growing a p-type layer on top of the AlGaN barrier, deposition and patterning of a gate metal and then selective recessing the p-GaN layer over the AlGaN barrier. This gate metal layer forms a Schottky or an ohmic contact with the p-GaN layer, and, as a consequence, the potential in the channel at the equilibrium is lifted-up therefore realizing e-mode operation.

Thus normally-off (enhancement-mode or E-mode) operation has been researched actively with threshold voltages ($V_{Th}$) up to ~2.5 V as shown in Figure 5.1 [108-116]. However, the threshold voltages of these HFETs are not high enough for power switching applications, where the threshold voltage above 3–5 V is preferred in order to prevent the misoperation caused by noise [117,118]. In contrast, GaN-based MISFETs exhibited normally-off operation with a threshold voltage higher than 3 V [118–121]. However, the ON state resistance of these MISFETs becomes higher than that of the HFETs because the MISFETs do not have the high mobility 2DEG at least between the gate and the drain.

In this chapter we focus on (i) the estimation of oxide interface charges in MIS HEMT structures and on two simulation studies dealing with alternative normally-off HEMT concepts, namely (ii) combine the effect of a p-type doped cap layer with that of a gate oxide, and (iii) the piezo neutralization technique (PNT).

The study on oxide interface charges is presented in Sec. 5.1.2. It is based on a comparison of measured and simulated threshold voltages of experimental HEMTs with and without an $Al_2O_3$ layer underneath the gate. We have brought measured and simulated threshold voltages for structures without an oxide into agreement assuming two different origins of the originally observed $V_{th}$ discrepancies. We find that in both cases the estimated oxide interface charge is the same. Moreover, we developed a simple analytical threshold voltage model for the MIS HEMT structure which can be used to estimate the interface charge with a pocket calculator. We propose also a new approach with combines the effect of a p-type doped cap layer with that of a gate oxide for designing and achieving normally-off HEMT.

In Sec. 5.1.3, our investigations on the piezo neutralization technique are discussed. We focus on the structures proposed by Ota et al. [122] using 1D Schrödinger-Poisson simulations and analytical models. In particular, our analytical model shows that the threshold voltage is independent on the thicknesses of both the PNT layer and the strained GaN channel layer. Additionally, we discuss options to increase the electron sheet density in the ungated device regions in order to reduce the source/drain resistances. Finally, Sec. 5.1.4 summarizes the report.

### 5.1.2. Oxide interface charges in MIS HEMT structures

The purpose of this study is to extract the oxide interface charges in experimental MIS HEMT structures by simply comparing measured and calculated threshold voltages. The experimental AlGaN/GaN HEMTs with and without an $Al_2O_3$ layer underneath the gate have been fabricated at Fraunhofer Institute for Applied Solid State Physics (IAF) in two batches. The main features of batches 1 and 2 are as follows:

| Batch 1: | Batch 2: |
|---|---|
| 24nm $Al_{0.18}Ga_{0.82}N$, 3nm GaN cap | 27nm $Al_{0.23}Ga_{0.77}N$, 3nm GaN cap |
| - W18 … Schottky gate (Ni/Au) | - W8 … Schottky gate (Ni/Au) |
| - W23 … 20nm $Al_2O_3$ + Ni/Au | - W37 … 20nm $Al_2O_3$ + Ni/Au |

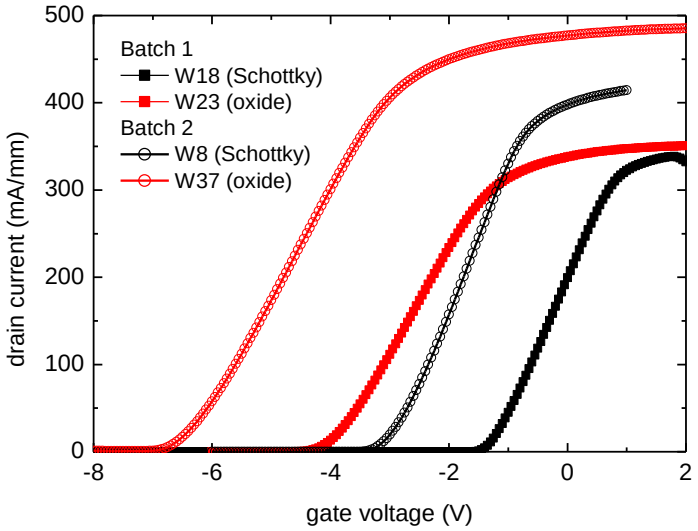


**Figure 5.1** Measured transfer characteristics of HEMTs with and without an oxide from two batches fabricated at IAF (with parameters above).

In Figure. 5.1 the measured transfer characteristics of the experimental HEMTs with and without an oxide from the two batches are compared. As can be seen, in both cases the threshold voltage $V_{th}$ is shifted towards more negative values when a gate oxide is used. In batch 1, the $V_{th}$ shift is approximately -2.7V, whereas in batch 2 the $V_{th}$ shift is -3.4V. This means, from the theoretical point of view, that there is a fixed charge at the oxide/semiconductor interface and if the actual value of this charge is known, it should be straightforward to calculate the measured $V_{th}$ with e.g. 1D numerical Schrödinger-Poisson simulations or an appropriate analytical model. In reverse, when varying the interface charge in the simulations, the correct value is achieved when the calculated threshold voltage agrees with the measured one. This is, in principle, our approach.

#### 5.1.2.1. 1D Schrödinger – Poisson simulations

Before we can start with a variation of the oxide interface charge, we have to make sure that the other important parameters of the simulation structures (see Figure 5.2) are appropriately chosen. This can be done by adjusting the parameters of the simulation structure with a Schottky gate (Figure 5.2a) to deliver the correct threshold voltage. This is illustrated in Figure 5.3, where simulated $n_S(V_G)$ curves are shown in comparison with the measured transfer characteristics of the HEMT without an oxide from batch 2. The three simulated curves have been obtained assuming different values for the bound polarization charges at the AlGaN/GaN interfaces, i.e. $\pm Q_p$ in Figure 5.2, and the Schottky barrier height of the metal/GaN contact $\Phi_B^{metal/GaN}$.

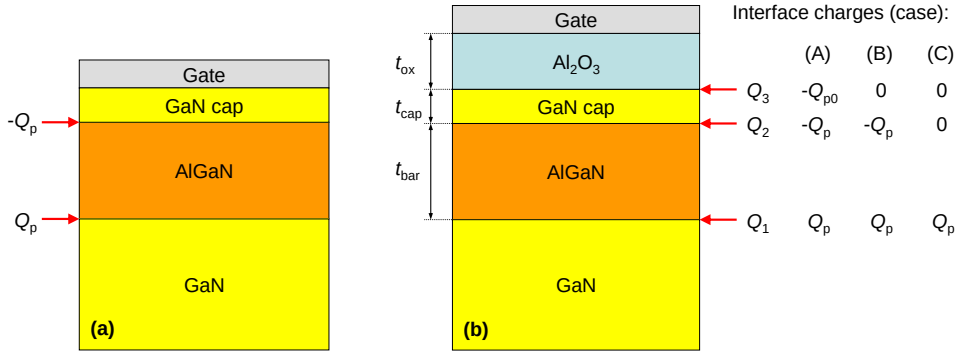


**Figure 5.2.** The 1D heterostructures considered in the Schrödinger-Poisson simulations. (a) Conventional HEMT and (b) MIS HEMT structure. In the MIS HEMT structure, three different cases of bound charges at the cap interfaces are considered ($Q_p$ is the bound charge at AlGaN/GaN heterojunctions caused by spontaneous and piezoelectric polarization, $Q_{p0}$ is fixed charge at the oxide/semiconductor interface.

For the $n_S(V_G)$ curve labeled with assumption (I) we used a $Q_p$ of $1.01\times10^{13}q/\mathrm{cm}^2$ ($q$ is the elementary charge) which has been calculated from the models given in [108] assuming a fully strained AlGaN barrier and a Schottky barrier height of 1eV – a typical value for Ni/Au contacts on n-type GaN [123]. As can be seen from Figure 5.3, these parameters result in a threshold voltage that is too negative compared to the measured characteristics. Such a discrepancy can have various origins, most likely a combination of several contributions. In this study we consider two extreme cases: the observed $V_{th}$ discrepancy is either completely attributed to the value of $\Phi_B^{metal/GaN}$ (assumption (II)), or to partial relaxation leading to a reduction of $Q_p$ (assumption (III)). For a correct threshold voltage, assumption (II) leads to a Schottky barrier height of 1.6eV, whereas with assumption (III) the calculated value for $Q_p$ has to be reduced by 12% to $8.89\times10^{12}q/\mathrm{cm}^2$. As can be seen from Figure 5.3, both assumptions lead to identical $n_S(V_G)$ curves which are in good agreement with the measured transfer characteristics.

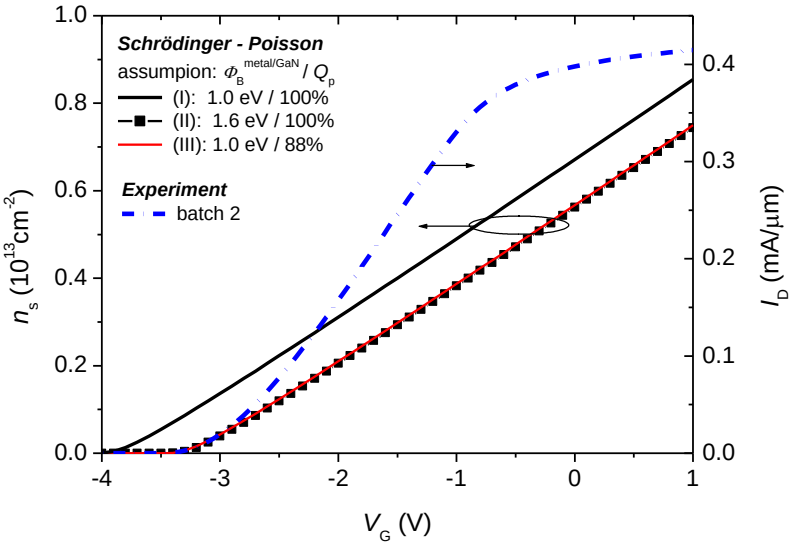


**Figure 5.3** Simulated $n_S(V_G)$ characteristics for the conventional HEMT structure of Figure. 5.2(a) assuming three different sets of the parameters polarization charge $Q$p and Schottky barrier height $\Phi_B^{metal/GaN}$. Also shown for comparison: the measured transfer characteristics of the conventional HEMT from batch 2 (W8 in Figure 5.1).

Let us now consider the MIS HEMT. Figure 5.4 shows simulated $n_S(V_G)$ curves for the three cases of bound charges at the oxide/cap and cap/AlGaN interfaces as described in Figure 5.2(b). In case A, the negative charge $-Q_{p0}$ caused by the spontaneous polarization in the GaN cap is assumed at the oxide/cap interface ($Q_3$), in case B this charge is assumed to be zero and in case C both interface charges of the cap layer ($Q_2$, $Q_3$) are set to zero. The latter case mimics an overall compensation of all charges close to the oxide interface. The values for $Q_p$ and the Schottky barrier height $\Phi_B$ of the gate/$Al_2O_3$ contact correspond to assumption (II), and $\Phi_B$ is calculated by

$$\Phi_B = \Phi_B^{metal/GaN} + \Delta E_{C1}, \qquad 5\text{-}1$$

where $\Delta E_{C1}$ is the conduction band offset between oxide and GaN. From Figure 5.4 it turns out that the actual charge at or close to the oxide interface defines whether the threshold voltage is more positive (case A), the same (case B), or more negative (case C) compared to the value of the conventional HEMT structure without an oxide. In comparison with the measured $I_D(V_G)$ curve for the MIS HEMT, case C shows the best agreement of the threshold voltage. In other words, the assumption of charge compensation at the oxide interface seems to be reasonable.

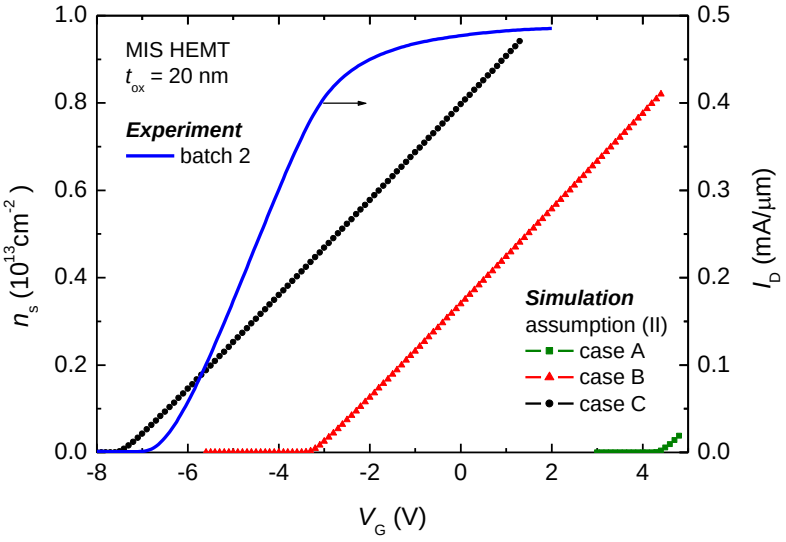


**Figure 5.4** Simulated $n_S(V_G)$ characteristics for the MIS HEMT structure of Figure 5.2(b) considering the three cases of bound interface charges as described in Figure 5.2(b). Also shown for comparison: the measured transfer characteristics of the MIS HEMT from batch 2 (W37 in Figure 5.1).

### 5.1.2.2. Analytical modeling

For a better understanding of the Schrödinger – Poisson results, an analytical threshold voltage model would be helpful. Such a model can be derived for the 1D electrostatic arrangement shown in Figure. 5. At threshold conditions, the whole structure can be assumed to be free from mobile carriers. Since the gate is the only electrode in the arrangement (the substrate is assumed to be infinitely thick), the counter charge for all the interface bound charges ($Q_1 \ldots Q_3$) can only be found at the gate. As we neglect any (unintentional) doping, the field in the GaN buffer $E_0$ must be zero. Knowing that $E_0 = 0$, we can calculate the electric field in every other layer applying Gauss's law at interfaces as

$$\begin{aligned} E_1 &= Q_1 / \varepsilon_{\text{bar}} \\ E_2 &= (Q_1 + Q_2) / \varepsilon_{\text{cap}} \\ E_3 &= (Q_1 + Q_2 + Q_3) / \varepsilon_{\text{ox}} \end{aligned} \qquad \text{5-2}$$

where $\varepsilon_{\text{bar}}$, $\varepsilon_{\text{cap}}$ and $\varepsilon_{\text{ox}}$ are the dielectric constants in the AlGaN barrier, GaN cap and the $Al_2O_3$ layers, respectively, and $Q_1 \ldots Q_3$ interface bound charges per Amp.s/cm$^2$. These fields are associated with the voltage drops

$$V_1 = -Q_1 \cdot t_{\mathrm{bar}} / \varepsilon_{\mathrm{bar}}$$
$$V_2 = -(Q_1 + Q_2) t_{\mathrm{cap}} / \varepsilon_{\mathrm{cap}} \qquad 5\text{-}3$$
$$V_3 = -(Q_1 + Q_2 + Q_3) t_{\mathrm{ox}} / \varepsilon_{\mathrm{ox}}$$

in the corresponding layers with the thicknesses $t_{\mathrm{bar}}$, $t_{\mathrm{cap}}$ and $t_{\mathrm{ox}}$. According to Figure 5.5, the threshold surface potential $\varphi_{\mathrm{th}}$ is then given by

$$\varphi_{\mathrm{th}} = V_1 + V_2 + V_3 + \varphi_0, \qquad 5\text{-}4$$

where $\varphi_0$ is the channel potential at threshold which is close to zero. The actual value of $\varphi_0$ depends on the threshold voltage definition and can be treated as a fitting parameter. The threshold voltage is related to $\varphi_{\mathrm{th}}$ as

$$V_{\mathrm{th}} = \varphi_{\mathrm{th}} - (\Delta E_{\mathrm{C1}} - \Phi_{\mathrm{B}}) / q = \varphi_{\mathrm{th}} + \Phi_{\mathrm{B}}^{\mathrm{metal/GaN}} / q. \qquad 5\text{-}5$$

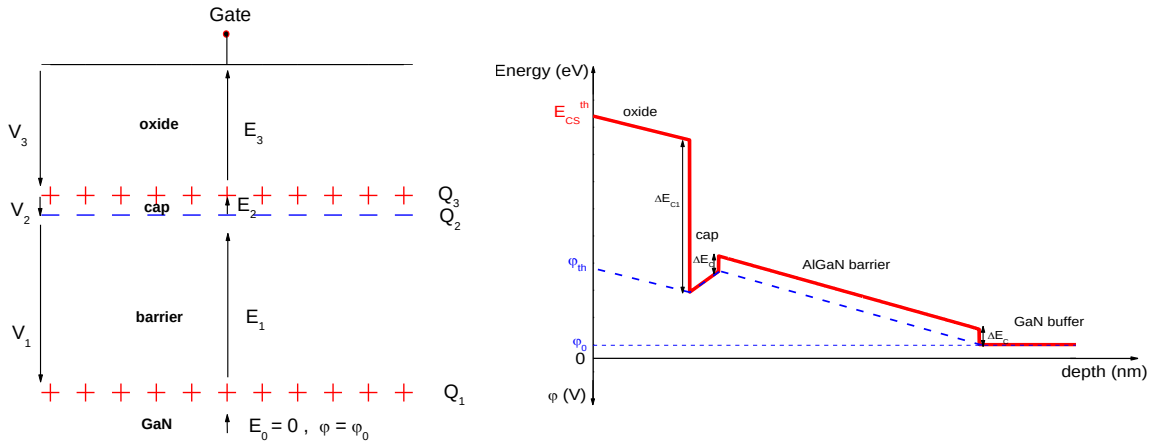


(a) (b)

**Figure 5.5** (a) Simplified 1D arrangement for which the analytical threshold voltage model has been derived. (b) The corresponding potential within the structure in comparison with the conduction band edge as obtained from Schrödinger – Poisson simulations.

Let us now test the analytical model by comparison with Schrödinger – Poisson results. Such a comparison can be seen in Figure. 6, where $V_{\mathrm{th}}$ for the cases A, B, C is shown as function of the oxide layer thickness using the parameter sets of both assumptions (II) and (III). The symbols represent the threshold voltages extracted from numerically simulated $n_S(V_G)$ curves using an

$n_{S,th}$ condition, i.e. $V_G = V_{th}$ where $n_S = n_{S,th} = 3\times10^{10}$cm$^{-2}$. The $V_{th}$ values from the analytical model (lines in Figure 5.6) have been calculated assuming $\varphi_0 = 0.1$V in all cases. As can be seen, the analytical results are in perfect agreement with the Schrödinger – Poisson values. Hence, we can use the model to interpret the observed trends.

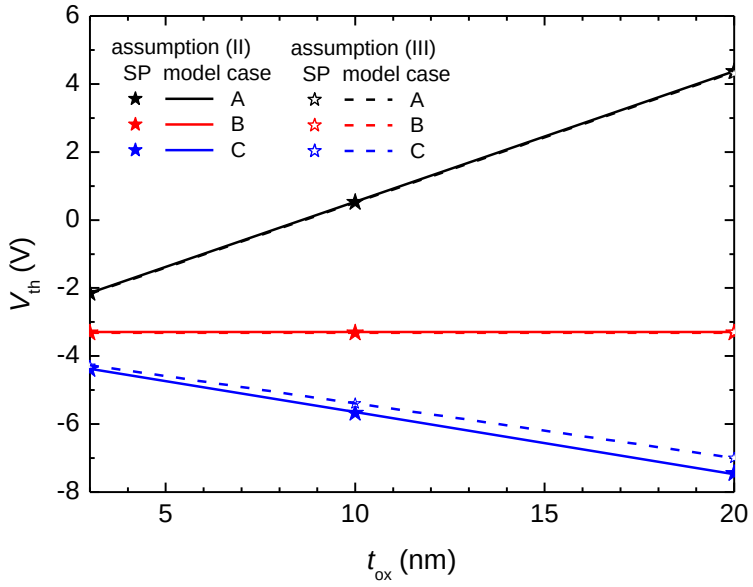


**Figure 5.6.** Threshold voltage of a MIS HEMT as function of the oxide thickness for the three cases of interface charges shown in Figure 5.2(b). Results from the analytical model (lines) are compared with Schrödinger – Poisson results (symbols) using the parameters of both assumption (II) and (III).

In case A, $Q_1 = -Q_2 = Q_p$ and $Q_3 = -Q_{p0}$. From eq. 5-3 we get $V_2 = 0$ and eq. 5-4 turns to

$$\varphi_{th} = -Q_p \cdot \frac{t_{bar}}{\varepsilon_{bar}} + Q_{p0} \cdot \frac{t_{ox}}{\varepsilon_{ox}} + \varphi_0 . \qquad 5\text{-}6$$

Since $Q_p$ and $Q_{p0}$ are positive charges, $\varphi_{th}$ and thus $V_{th}$ becomes more positive when $t_{ox}$ is increased. In case B, $Q_3 = 0$ and according to 5-3 $V_2 = V_3 = 0$. In this case eq. 5-4 reduces to

$$\varphi_{th} = -Q_p \cdot \frac{t_{bar}}{\varepsilon_{bar}} + \varphi_0 \qquad 5\text{-}7$$

which does not depend on the oxide thickness anymore. In other words, if the oxide/cap interface charge is zero and no other charge is in the cap except the nominal negative

polarization charge at the cap/AlGaN interface, the MIS HEMT has the same threshold voltage as the conventional HEMT without an oxide. In case C, $Q_1$ is the only fixed charge in the structure and from Equs. 5-3 and 5-4 we get

$$\varphi_{\mathrm{th}} = -Q_{\mathrm{p}}\left(\frac{t_{\mathrm{bar}}}{\varepsilon_{\mathrm{bar}}} + \frac{t_{\mathrm{cap}}}{\varepsilon_{\mathrm{cap}}} + \frac{t_{\mathrm{ox}}}{\varepsilon_{\mathrm{ox}}}\right) + \varphi_0 \,. \qquad 5\text{-}8$$

Accordingly, an increase of $t_{\mathrm{ox}}$ results in a more negative threshold voltage. Although case C can describe the experimental findings qualitatively correct, a quantitative discrepancy to the experiment remains as can be seen from Figure 5.4. Obviously, the assumption of zero charge in the cap is too simple. A more realistic approach is to take the negative polarization charge $-Q_{\mathrm{p}}$ at the cap/AlGaN interface into account while assuming a positive charge $Q_3$ at the oxide/cap interface.

### 5.1.2.3. Extraction of the oxide interface charge

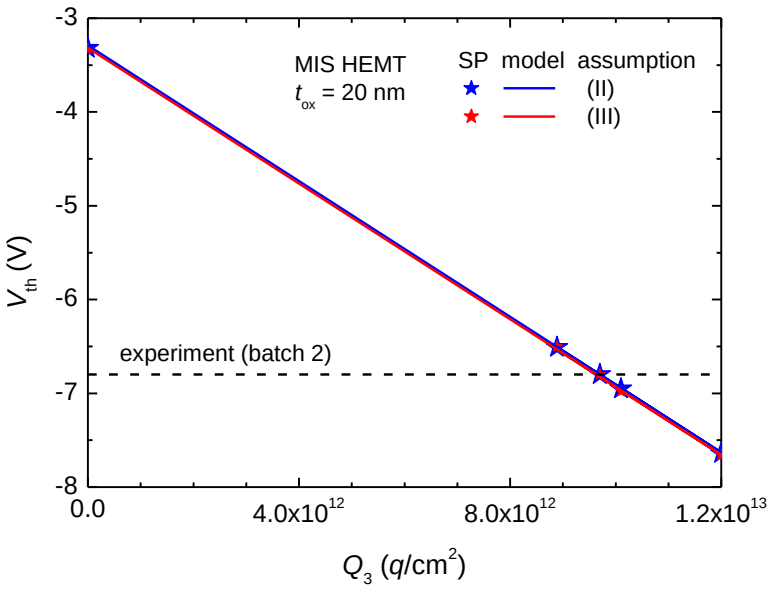


**Figure 5.7.** Threshold voltage as function of the oxide interface charge $Q_3$. Results from the analytical model (lines) are shown together with Schrödinger – Poisson results (symbols) using the parameters of both assumption (II) and (III). Horizontal line: threshold voltage of the experimental MIS HEMT from batch 2.

A simple graphical approach to find the correct value of $Q_3$ is demonstrated in Figure 5.7. Here, the calculated threshold voltages are plotted as function of $Q_3$ whereas the horizontal line represents the experimental $V_{\mathrm{th}}$. The latter has been taken from the measured transfer characteristics at a drain current of 3µA/µm. Now, the correct value for $Q_3$ can be read from the

*x* axis at the point where the theoretical function $V_{th}(Q_3)$ crosses the horizontal line. We find $Q_3 = 9.7\times10^{12}q/cm^{-2}$, which is almost identical to $Q_p$ when assuming a fully strained barrier. This is also the case for batch 1, where we find $Q_3 = Q_p = 7.66\times10^{12}q/cm^{-2}$. Note that both assumptions (II) and (III) lead to identical results, which is surprising as in case C a slight deviation has been observed between both assumptions (see Figure. 6).

As can be seen from Figure 5.7, again the analytically calculated $V_{th}(Q_3)$ functions are in perfect agreement with the Schrödinger – Poisson results. Hence, $Q_3$ can be calculated directly from our model after a few rearrangements.

$$Q_3 = -C_{ox}\left(V_{th}^{MIS} + Q_p / C_{bar} - \varphi_0 - \Phi_B^{metal/GaN} / q\right) \qquad 5\text{-}9$$

Here $V_{th}^{MIS}$ is the measured threshold voltage of the MIS HEMT, whereas $C_{ox} = \varepsilon_{ox} / t_{ox}$ and $C_{bar} = \varepsilon_{bar} / t_{bar}$. When, as is the case discussed here, the threshold voltage of the HEMT without the oxide is known as well, $Q_3$ can simply be calculated from the observed threshold voltage difference as

$$Q_3 = -C_{ox}\left(V_{th}^{MIS} - V_{th}\right), \qquad 5\text{-}10$$

where $V_{th}$ is the threshold voltage of the conventional HEMT. Note that eq. 5-10 does not depend on uncertain/unknown quantities like $\Phi_B^{metal/GaN}$, $Q_p$ or $\varphi_0$ anymore. Instead, it is based on the assumptions that $Q_p$ is identical in both structures and that eq. 5-1 holds.

#### 5.1.2.4. Design options for a normally-off MIS HEMT

Although the experiments at IAF with $Al_2O_3$ discussed so far do not really support the idea of a normally-off MIS HEMT without recessed MIS-gate consideration, we think that there are still feasible design options that can lead to normally-off operation when using $Al_2O_3$. One idea is for instance, to combine the effect of a p-type doped cap layer with that of a gate oxide. The potential of a p-doped GaN-cap layer for the design of a normally-off HEMT (without an oxide) has already been investigated theoretically at IAF by Vladimir Polyakov and the results look very promising [115, 124]. Now the idea is simply, to put an $Al_2O_3$ layer between the p-doped GaN-cap and the gate electrode to suppress gate leakage currents.

We performed simulations of structures with various cap thicknesses and acceptor concentrations. The interface charges at the cap interfaces were set to the values found from the

comparison with experiments, as explained in paragraph 2.2 (i.e. the negative polarization charge at the cap/AlGaN interface and the same value but positive at the oxide/cap interface).

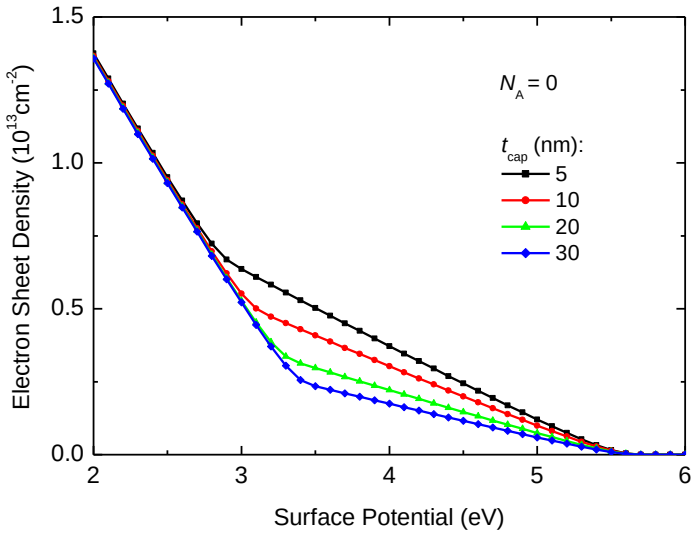


(a)

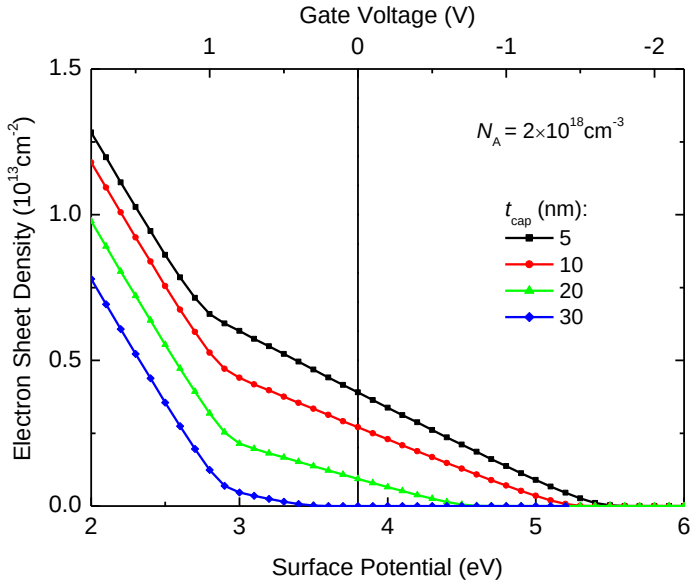


(b)

**Figure 5.8** Simulated $n_S(E_{CS})$ curves for structures with different $t_{cap}$ where (a) the cap is undoped and (b) the cap is doped with $N_A = 2\times10^{18}$cm$^{-3}$. The Al-content is assumed to be 0.23.

In order to avoid structures with very small transconductances (or small gate capacitances) we reduced the AlGaN thicknesses to 10nm and the oxide thickness to 5nm. Figure 5.8 shows simulated $n_S(E_{CS})$ curves for structures with different $t_{cap}$ where (a) the cap is undoped and (b) the cap is doped with $N_A = 2\times10^{18}$cm$^{-3}$. The Al-content is considered to be 0.23 here. As can be

seen, in the case of an undoped cap, the cap thickness has no effect on the threshold voltage. When, on the other hand, the cap is highly p-type doped, the threshold voltage can be shifted toward positive values when $t_{cap}$ is increased. With a doping level of $N_A = 2\times10^{18}cm^{-3}$ that is the case for a cap thickness larger than 20nm, as can be seen from Figure 5.8(b).

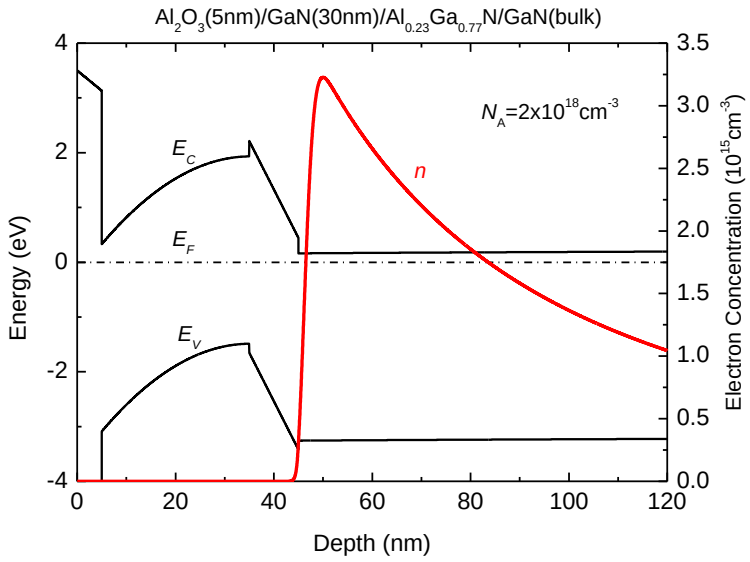


(a)

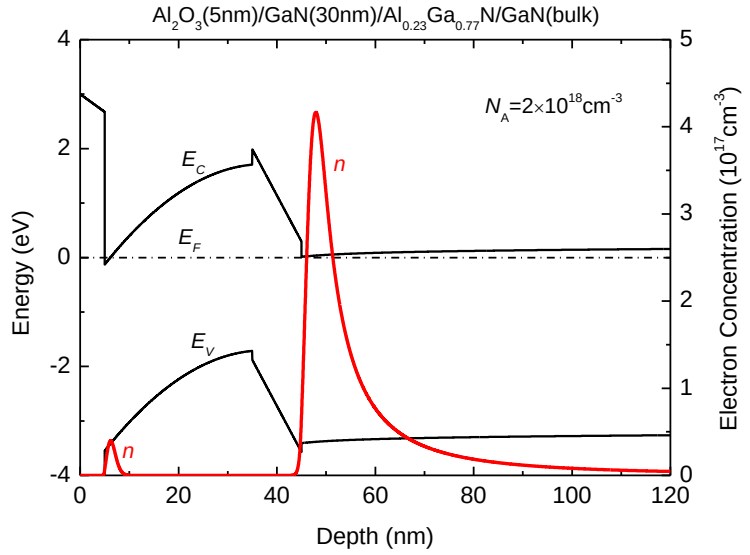


(b)

**Figure 5.9** Band diagram and the electron distribution of a MIS heterostructure with a 30nm thick p-type GaN cap for a surface potential of (a) 3.5eV and (b) 3.0eV.

However, from the $n_S(E_{CS})$ curves in Figure 5.8 we can clearly distinct two regions of operation. In the first region the curves have a moderate slope, which depends on the cap thickness. As can be seen from Figure 5.9(a), this is the region with proper HEMT operation, i.e. with a 2DEG at the AlGaN/GaN-buffer interface and with all the other layers fully depleted from mobile carriers. In the region of operation with the steeper slope, for which the band diagram and the electron distribution is shown in Figure 5.9(b), a second electron channel is formed in the cap, which basically shields the 2DEG at the AlGaN/GaN interface. The second channel is formed in GaN-cap and controlled via the oxide layer and thus the steeper slopes of the $n_S(E_{CS})$ curves in Figure 5.8 are independent of the cap thickness.

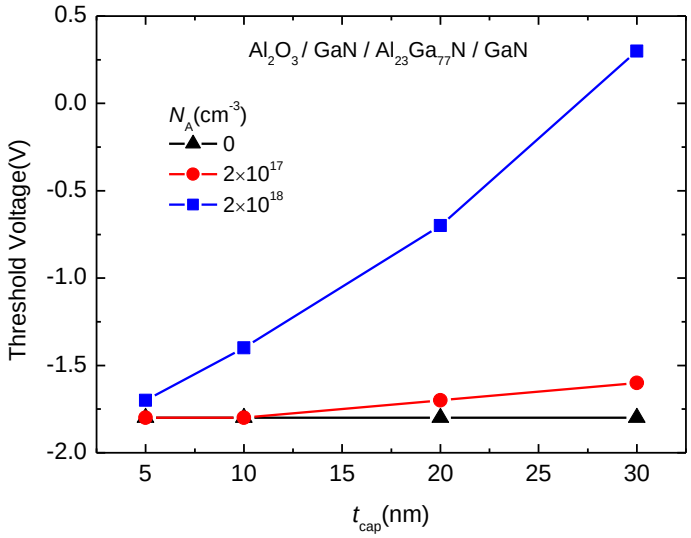


**Figure 5.10** Threshold voltage of MIS heterostructures as function of $t_{cap}$ for three different cap doping levels.

Figure 5.10 shows the threshold voltage as function of $t_{cap}$ for three different cap doping levels. From this plot it is obvious that the acceptor concentration must be in the order of $10^{18}cm^{-3}$ to get a positive threshold voltage. For smaller doping levels, the cap would have to be made much too thick to be considered for a realistic device.

However, the best solution would be the ability to fabricate an oxide/cap interface with a negative interface charge. That would bring us to the case A shown in Figure 5.5, where we simply have to increase the oxide thickness to get a positive $V_{th}$. According to CV measurements, the electron sheet density strongly depends on the surface treatment before the deposition of $Al_2O_3$. For certain samples the sheet density decreased after $Al_2O_3$ was deposited. It seems that in these samples the positive interface charge is strongly reduced.

#### 5.1.2.5. Simulating tunneling at Schottky contacts

Gate leakage currents are generally a serious issue in AlGaN/GaN HEMTs. Although the detailed mechanisms that lead to the observed gate leakage may be strongly related to the specific fabrication process of the devices, it seems that tunneling through the Schottky contact plays a crucial role in any case. One aim of the activities our group at TU Ilmenau is to support the understanding of the mechanisms responsible for the gate currents of the AlGaN/GaN HEMTs fabricated at IAF by device simulations. As a first step, we tested several models of the device simulator ATLAS that describe tunneling at Schottky contacts.

Let us start with a brief overview over the Schottky tunneling models available in ATLAS [76].

*A. Standard Schottky tunneling model (SST)*

- Describes direct tunneling (DT) through the Schottky barrier (field emission) and
- Thermionic emission over the barrier.
- Assumes a triangular potential barrier, i.e. only the electric field directly at the contact is taken into account.

*B. Universal Schottky tunneling model (UST) [4]*

- Describes direct tunneling through the Schottky barrier.
- Considers an arbitrarily shaped barrier, i.e. localized tunneling rates.

*C. Parabolic field emission model [126]*

- Was especially developed for SiC Schottky diodes with a thick n-type SiC body.
- Describes direct tunneling through the Schottky barrier.
- Considers a parabolic potential barrier, i.e. the tunneling rate depends directly on both, doping and applied voltage.

*D. Phonon-assisted tunneling model (Pipinys model) [127]*

- Describes phonon-assisted tunneling from traps located near the metal/semiconductor interface.

- All traps are assumed to be occupied by an electron.

- Only the electric field directly at the contact is taken into account.

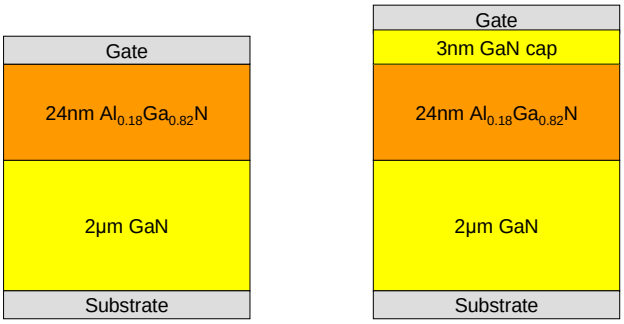


-

**Figure 5.11.** AlGaN/GaN heterostructures with (right) and without (left) a GaN cap used in ATLAS simulations to test various Schottky tunneling models.

The models A, B and D have been tested on 1D AlGaN/GaN heterostructures with and without a GaN cap as shown in Figure 5.11. The parabolic field emission model (model C) is considered to be too specifically related to Schottky diodes with a thick semiconductor bulk and has therefore not been tested here.

Figure 5.12 shows the simulated gate leakage currents as function of the applied reverse voltage. Also shown for comparison are measured gate currents of an experimental AlGaN/GaN HEMT fabricated at IAF. As can be seen from Figure 5.12(a), the tested ATLAS models give reasonable results for the structure without a cap: direct tunneling (DT) currents from the SST and UST models are smaller than trap-assisted tunneling (TAT) currents obtained from the Pipinys model. The measured gate currents lay in-between the simulated DT and TAT currents. That suggests that tunneling via traps could be an important mechanism for the gate leakage in the experimental devices.

In Figure 5.12(b) the results for the structure with a cap are shown. It turns out that ATLAS models which only consider the electric Field at the contact (SST, Pipinys) have serious problems to handle the cap. Using these models without modification, the simulated currents almost vanish completely. Nevertheless, the Pipinys model can give correct currents for large negative gate voltages, if the trap energy is adjusted. Currents calculated by the UST model drop by two orders of magnitude, which sounds reasonable. However, the absolute values from UST are much too small when compared with measured currents.

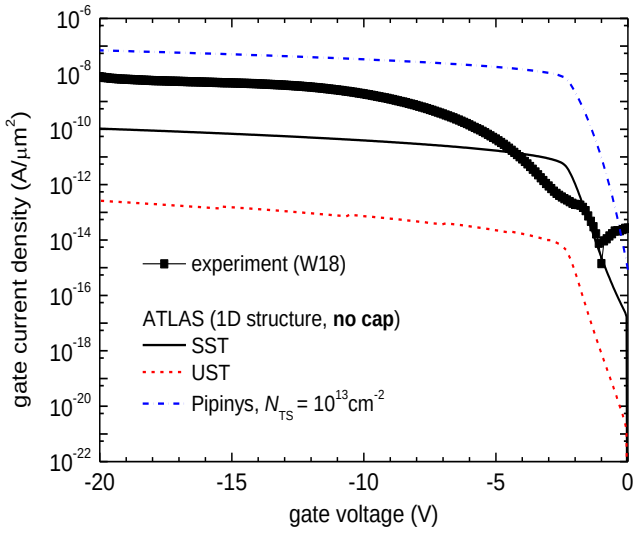


(a)

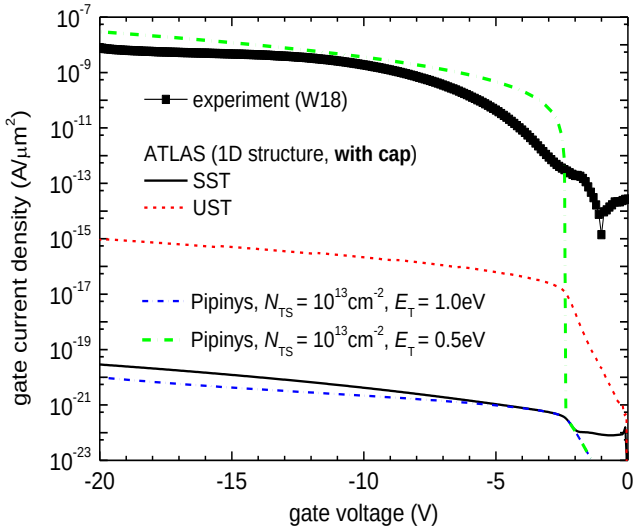


(b)

**Figure 5.12.** Simulated gate leakage currents as function of the applied reverse voltage using different Schottky tunneling models of ATLAS. Also shown for comparison are measured gate currents of an experimental AlGaN/GaN HEMT fabricated at IAF. (a) heterostructure without and (b) with a GaN cap. For the Pipinys model a surface trap density of $N_{TS} = 10^{13}\text{cm}^{-2}$ is assumed, whereas the trap energy level $E_T$ has been varied.

Figure 5.13 illustrates the problem that the ATLAS models have with cap layer. The standard Schottky model and the Pipinys model can only describe the Schottky contact directly, but not the heterojunction between the GaN cap and the AlGaN layer. Both models only depend on the electric field at the Schottky contact and at negative gate bias, the electric field in the cap layer (i.e. at the Schottky contact) is much smaller than that in the AlGaN. The UST model, on the other hand, is in principle able to describe the situation, but it does not account for trap-assisted

tunneling. In other words, we need a model which is able to describe TAT at a Schottky contakt on a heterostructure with a cap layer.

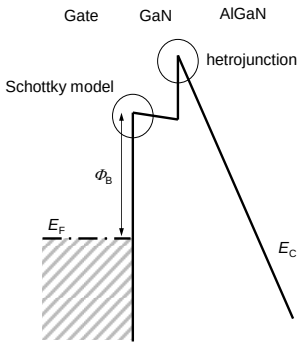


**Figure 5.13.** Schematic conduction band profile at the Schottky contact on a heterostructure with a cap layer.

A promising workaround could be the use of the ATLAS band-to-band tunneling (BBT) model to mimic tunneling from the Schottky contact. The BBT model introduces a field-dependent generation rate given by

$$G = \alpha E^{\gamma} exp(-\beta/E), \qquad 5\text{-}11$$

where $E$ is the local electric Field. The model parameters $\alpha$, $\beta$ and $\gamma$ make the BBT model very flexible and can be adjusted to model the field dependence of various leakage mechanisms. This is demonstrated in Figure 5.14(a), where the model is fitted to describe the field dependence of DT or TAT [128]. In our simulation structure, we can now define a thin layer within the AlGaN close to the Schottky contact in which the fitted BBT model is switched on. The simulated leakage currents for the structures with and without a cap are shown in Figure 5.14(b). As can be seen, for gate voltages smaller than -2V, the adjusted BBT model gives the same currents for both structures, with and without a cap respectively, independent of the used parameter set (DT or TAT). That shows that in principal, the BBT model parameters can be adjusted to simulate the measured gate currents. Moreover, with this method we can emulate various tunneling models derived from first-order principles, which are not explicitly incorporated in ATLAS.

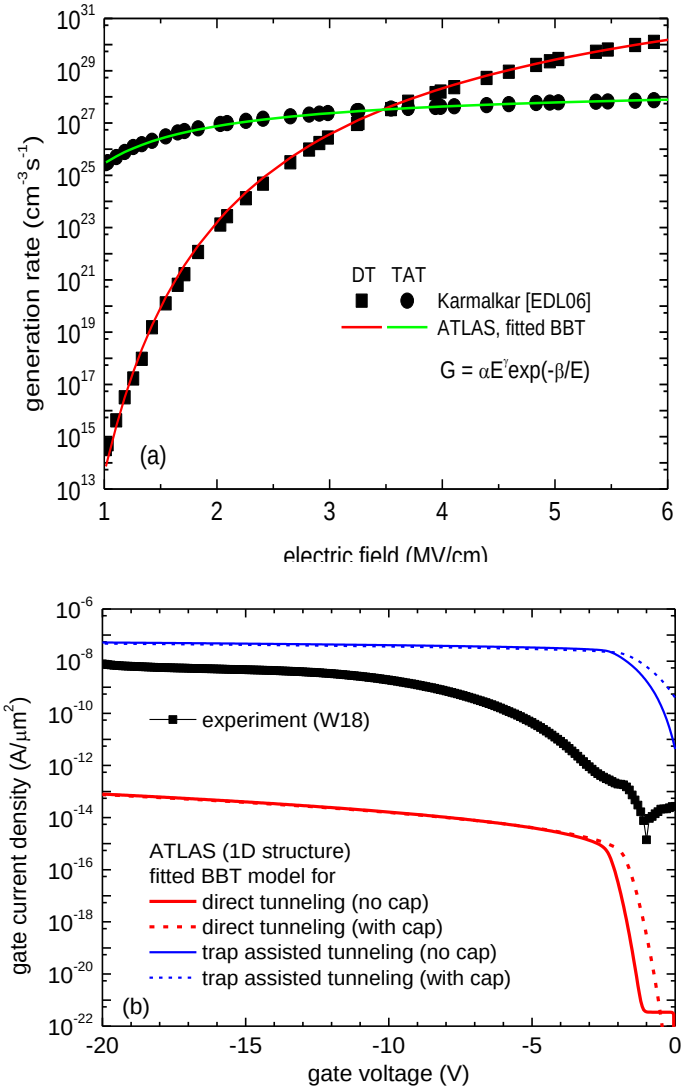


**Figure 5.14.** (a) Generation rates for trap-assisted tunneling (TAT) and direct tunneling (DT) at a Schottky contact as function of the electric field [110]. The lines are fits of the ATLAS band-to-band tunneling (BBT) model. (b) Simulated leakage currents for the structures with and without a cap using the fitted BBT model.

### 5.1.2.6. Summary

The effect of an oxide layer on the threshold voltage strongly depends on the actual charge in the GaN-cap layer. The comparison of measured and simulated threshold voltages suggests that the negative bound polarization charge at the GaN-cap/AlGaN interface is compensated by a positive charge at the $Al_2O_3$/GaN-cap interface. The net charge in the cap layer is approximately zero. Thus the threshold voltages of experimental MIS HEMTs with 20nm $Al_2O_3$ between gate and cap are more negative than those of standard HEMTs without an oxide.

In case it is not possible to reduce the positive charge at the oxide/GaN interface, it is still possible to get a normally-off MIS HEMT when using a ~25nm thick p-doped GaN cap between

the oxide and the AlGaN barrier. However, according to the electron sheet density from CV measurements strongly depends on the surface treatment before the deposition of $Al_2O_3$. For certain samples the sheet density decreased after $Al_2O_3$ was deposited. It seems that in these samples the positive interface charge is strongly reduced.

The test of the ATLAS models to simulate tunneling through Schottky contacts was successful. All tested models deliver reasonable results. However, none of the Schottky models can describe trap-assisted tunneling at a structure with a GaN-cap. A promising workaround could be the use of the ATLAS band-to-band tunneling model with modified parameters. This approach is very flexible and can be used to emulate tunneling models derived from first-order principles, which are not explicitly incorporated in ATLAS.

### 5.1.3. Normally-off HEMTs using a piezo neutralization technique

As we have seen in the above discussion, the idea of putting an oxide underneath the gate of an otherwise conventional HEMT structure does not necessarily result in a normally-off device. Therefore, alternative concepts for normally-off operation should be taken into consideration. One of these concepts is the so-called piezo neutralization technique (PNT) that has been introduced by Ota et al. [122]. The device structure is shown in Figure 5.15 and features a thin strained GaN channel layer on top of an $Al_{0.07}Ga_{0.93}N$ buffer and a recessed gate which is in contact to the so-called PNT layer having the same Al-content as the buffer. Ota et al. have shown that this layer sequence exhibits normally-off behavior without (simulation) and with (experiment) a thin oxide between the gate electrode and the PNT layer shown in Figure 5.15. In the ungated device regions, a second supply layer with a larger Al-content is placed on top of the PNT layer to minimize the source/drain series resistances.

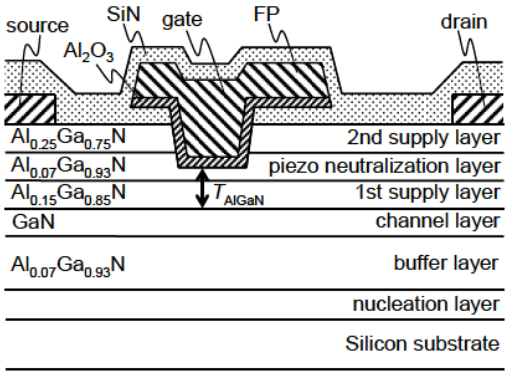


**Figure 5.15.** The normally-off GaN MIS HEMT with a piezo neutralization (PNT) structure as introduced by Ota et al. [122].

To get a deeper understanding of this concept, we performed 1D Schrödinger – Poisson simulations of both the gated and the ungated regions of the PNT device. The simulation structures are shown in Figure 5.16 and the corresponding interface charges can be found from Figure 5.17. The latter have been calculated from the models given in [129]. Note that the bound charges for relaxed layers are shown for comparison only as we consider strained layers in this study.

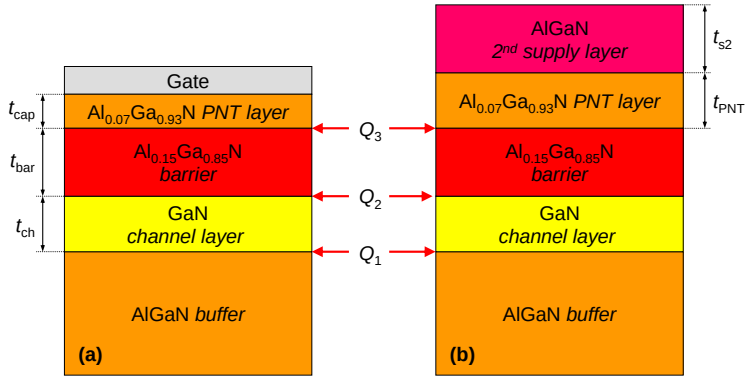


**Figure 5.16.** The 1D heterostructures considered in the Schrödinger-Poisson simulations to describe (a) the gated and (b) the ungated regions of a normally-off PNT HEMT.

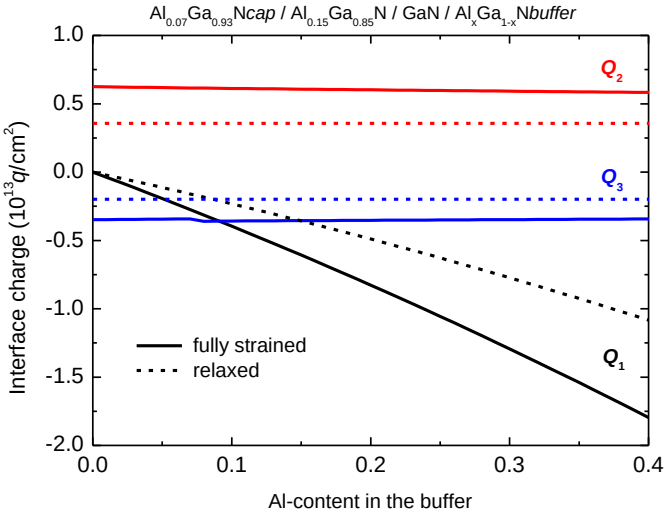


**Figure 5.17** The interface charges (compare Figure 5.16) considered in this study.

Let us start with the gated PNT structure. From Figure 5.18 the effect of the Al content in the buffer on the $n_S(V_G)$ characteristics can be seen. An increase of $x$ increases the strain in the channel and the threshold voltage is shifted in positive direction. For $x$ = 0.05, normally off-operation is achieved. A remarkable property of this structure is the fact, that $V_{th}$ does not depend on the GaN layer thickness as can be seen from Figure 5.19(a). Moreover, in case that

both the buffer and the PNT layer have the same Al-content, the threshold voltage is also

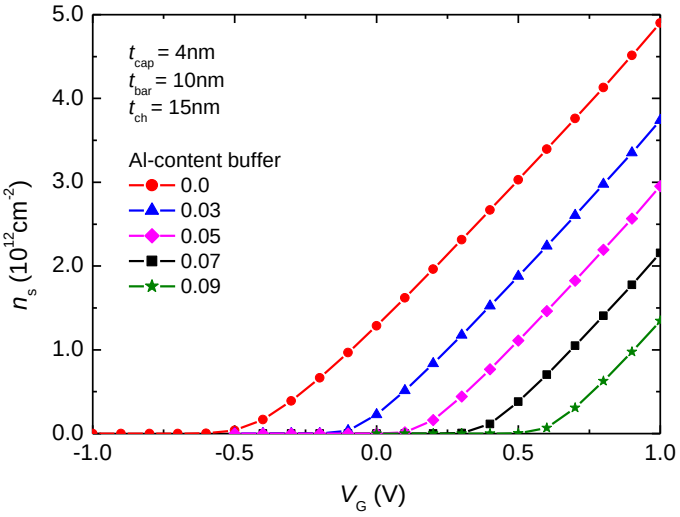


**Figure 5.18.** Simulated $n_S(V_G)$ characteristics for the gated PNT structure of Figure 5.16(a) considering various Al-contents in the buffer. A Schottky barrier height of 1eV is assumed.

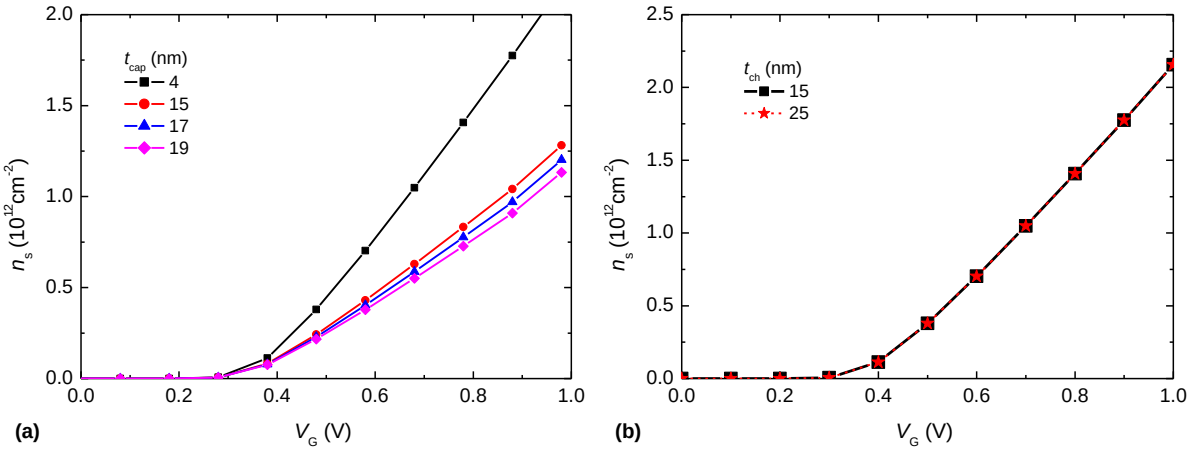


**Figure 5.19.** Influence of (a) the PNT layer and (b) the channel layer thicknesses, $t_{cap}$ and $t_{ch}$ respectively, on the $n_S(V_G)$ characteristics of the gated PNT structure.

independent of the gate recess depth, as long as the contact is within the PNT layer (Figure 5.19(b)). This makes the technology very robust regarding $V_{th}$ control.

An analytical $V_{th}$ model for the PNT structure can be helpful to understand these properties. A similar ansatz as for the MIS HEMT leads to an equation equivalent to equ. 5-4, i.e.

$$\varphi_{th} = V_1 + V_2 + V_3 + \varphi_0, \qquad 5\text{-}12$$

where

$$
\begin{aligned}
V_1 &= -Q_1 \cdot t_{ch} / \varepsilon_{ch} \\
V_2 &= -(Q_1 + Q_2) t_{bar} / \varepsilon_{bar} \\
V_3 &= -(Q_1 + Q_2 + Q_3) t_{cap} / \varepsilon_{cap}
\end{aligned}
\quad . \qquad 5\text{-}13
$$

The parameter $\varphi_0$ now has a different meaning, i.e. it is the potential in the buffer at threshold rather than the channel potential. As illustrated in Figure 5.20, $\varphi_0$ is given by

$$\varphi_0 = Q_1 \cdot t_{ch} / \varepsilon_{ch} = -V_1, \qquad 5\text{-}14$$

when assuming that the conduction band edge in the channel touches the Fermi level. Hence, $\varphi_{th}$ and thus $V_{th}$ do not depend on the channel layer thickness $t_{ch}$. Moreover, in the case of the same Al-content in both the buffer and the PNT layer the condition

$$Q_1 + Q_2 + Q_3 = 0 \qquad 5\text{-}15$$

holds, i.e. $V_3 = 0$. In this case equ. 5-12 reduces to

$$\varphi_{th} = V_2 = Q_3 \cdot t_{bar} / \varepsilon_{bar} \qquad 5\text{-}16$$

which does not depend on the PNT layer thickness $t_{cap}$. The relation between $V_{th}$ and $\varphi_{th}$ is given by

$$V_{th} = \varphi_{th} - (\Delta E_{C1} - \Phi_B) / q, \qquad 5\text{-}17$$

where $\Delta E_{C1}$ is the (effective) conduction band offset between the PNT and channel materials.

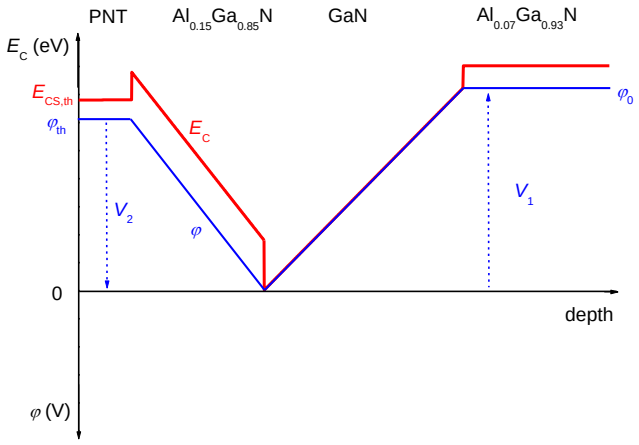


**Figure 5.20.** Conduction band edge and potential in the gated PNT structure at threshold conditions.

In Figure 5.21 the threshold voltages calculated from equ. 5-17 are compared with Schrödinger – Poisson results for various buffer compositions. The model results are in good agreement with the Schrödinger – Poisson values, although the latter show a slightly stronger dependence on *x*. This can be attributed to quantum effects as follows: From Figure 5.20 it is obvious that the conduction band edge in the channel forms a triangularly shaped potential well at the barrier/channel interface. Note that this is not the case in a conventional HEMT, where the channel potential is almost flat at threshold conditions. In the PNT structure on the other hand, quantum confinement causes the formation of subbands whose energies strongly depend on the slope of $E_C$, i.e. on the electric field caused by $Q_1$. The larger this interface charge is, the higher are the subband energies and the threshold voltage is shifted further towards positive values. However, this is a second order effect since the overall trend is correctly described by our model.

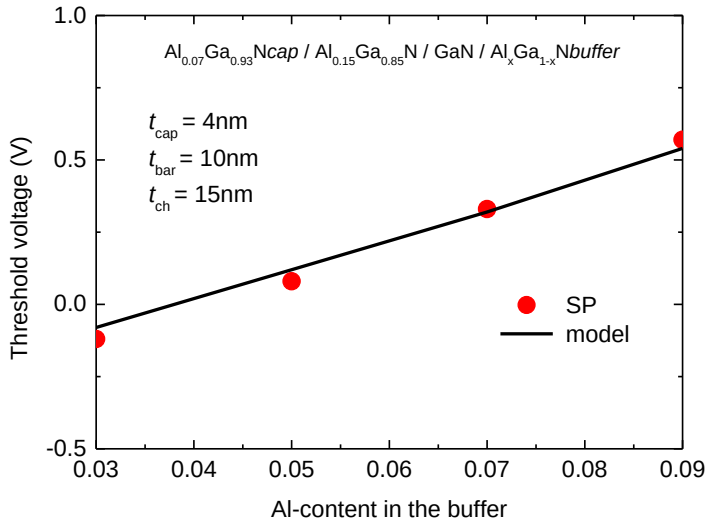


**Figure 5.21.** Threshold voltage as function of the Al-content in the buffer. Results from the analytical model (line) are compared with Schrödinger – Poisson results (symbols).

In general, the 2DEG density in the ungated parts of a HEMT has to be sufficiently high to provide a good connection of the gated channel region to the source/drain contacts. In a normally-on design, this is inherently guarantied by the layer structure throughout the device. In a normally-off device, on the other hand, the layer design in the ungated regions has to be different from the design underneath the gate as in the gated part the 2DEG is supposed to vanish at $V_G = 0$. It is therefore interesting to take a look on the 2DEG density in the ungated parts of the PNT device. It is clear that the electron density depends on the surface potential in this region, i.e. the conduction band edge at the surface of the 2$^{nd}$ supply layer $E_{CS}$. In Figure

5.22 the influence of the surface potential on the electron distribution in the structure can be seen. Figure 5.22(a) shows the band diagram and the electron density distribution for a surface potential of 1.2eV. The PNT layer is assumed to have the same Al-content as the buffer ($x$ = 0.07), whereas in the 2nd supply layer $x$ = 0.25. As can be seen, two electron channels are formed, one at the AlGaN/GaN interface, i.e. the actual channel, and another parasitic channel at the interface PNT/2nd supply layer where the electron density is even higher than in the actual channel. In Figure 5.15(b) both the overall electron sheet density $n_S$ and the sheet density of the actual channel $n_{S,ch}$ are plotted as function of the surface potential. As can be seen, $n_{S,ch}$ saturates when the overall $n_S(E_{CS})$ becomes steeper. The saturation occurs when the 2nd channel is starts to form. The parasitic channel then shields the actual channel from the surface potential. The question now is which surface potential can be assumed. From basic considerations it is clear that at the surface, the Fermi level has to be located somewhere within the band gap. In other words, the maximum possible value for $E_{CS}$ is the gap energy of the 2nd supply layer, whereas the minimum $E_{CS}$ is zero. In our case, $E_{CS,max} = E_G$ = 3.91eV which is the worst case for the 2DEG density. At this surface potential $n_{S,ch}$ is much smaller than its saturation value of about $1.5\times10^{12}$cm$^{-2}$. Apart from the worst case, even the saturation value of $n_{S,ch}$ is rather too small for a low resistivity. Hence it is desirable to find design options for an optimization of both the saturation value of $n_{S,ch}$ and the $E_{CS}$ range for this maximum sheet density. In other words both the threshold surface potential for the actual channel and its saturation density should be as high as possible.

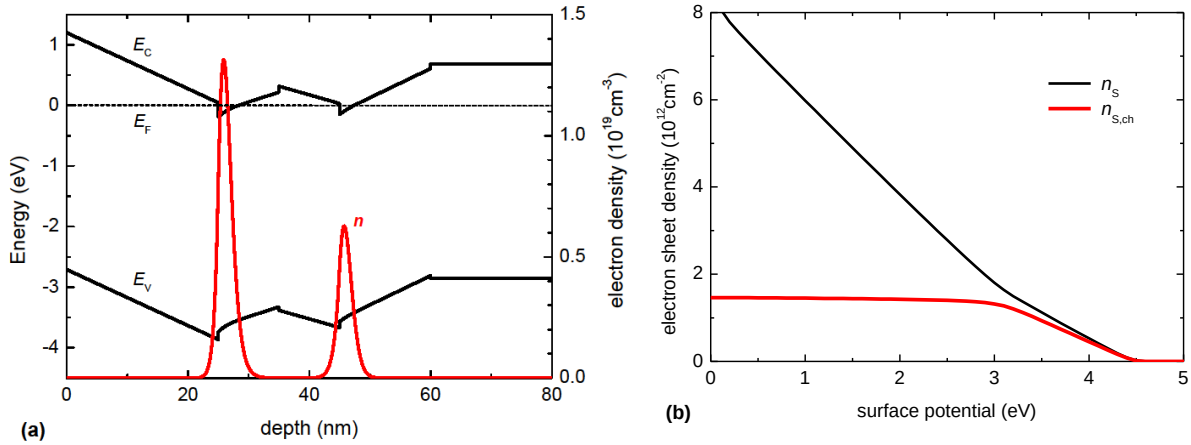


**Figure 5.22.** (a) Band diagram and the electron density distribution in the ungated PNT structure for a surface potential of 1.2eV. (b) Overall electron sheet density $n_S$ in the ungated PNT structure and sheet density of the actual channel $n_{S,ch}$ as function of the surface potential.

On the other hand, such an optimization should not affect the $n_S(V_G)$ characteristics of the gated region of the device. Hence, only the 2nd supply layer or the PNT layer should be considered.

Figure 5.23 shows the effect of (a) the PNT layer thickness $t_{PNT}$, (b) the thickness $t_{s2}$ and (c) the Al-content of the 2nd supply layer on the $n_{S,ch}(E_{CS})$ characteristics. Obviously, a reduction of $t_{PNT}$ leads to an increase of the saturation $n_{S,ch}$, whereas an increase of either the thickness or the Al-content of the 2nd supply layer primarily extents the $E_{CS}$ range for saturation with little effect on the maximum $n_{S,ch}$ value. From Figure 5.23(a) it turns out that $n_{S,ch}$ cannot be made larger than ~$2\times10^{12}$cm$^{-2}$ by just reducing $t_{PNT}$, in particular as the PNT layer must not be too thin for a good $V_{th}$ control. An optimization of the 2nd supply layer does not seem that critical; partial relaxation, however, should be avoided.

To summarize, the piezo neutralization technique is an interesting concept for a normally-off HEMT technology. As a critical point partial relaxation could be addressed since the strain in the channel and the barrier layers are essential for normally-off operation, whereas a fully strained 2nd supply layer guaranties low series resistances.

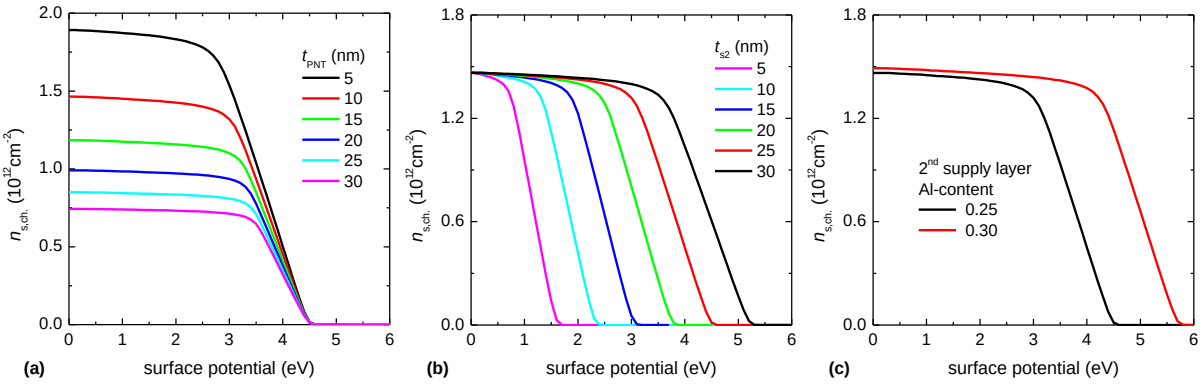


**Figure 5.23.** The effect of (a) the PNT layer thickness $t_{PNT}$, (b) the thickness $t_{s2}$ and (c) the Al-content of the 2nd supply layer on the $n_{S,ch}(E_{CS})$ characteristics.

### 5.1.4. Conclusion

We have theoretically investigated three possible options for a normally-off GaN HEMT technology, i.e. the MIS HEMT and two alternatives, the so-called piezo neutralization technique (PNT) and p-type doped cap layer GaN MIS HEMT.

We find that the threshold voltage of the MIS HEMT strongly depends on the oxide/semiconductor interface charge in the device. This can be explained by an analytical threshold voltage model that we have developed for the MIS HEMT structure. The model can

be used to extract the oxide interface charge from measured threshold voltages. For the experimental MIS HEMTs fabricated at IAF, this charge is found to be positive having the same value as the bound polarization charge at the AlGaN/GaN interface. This positive charge compensates the negative bound charge at the GaN cap/AlGaN interface leading to the observed negative threshold voltage of the experimental devices.

The two alternative normally-off concepts are more stable regarding threshold voltage adjustment. In particular the PNT concept turns out to be very robust against process fluctuations. Its main advantage is that the threshold voltage does not depend on critical parameters like the PNT layer and the channel layer thicknesses. These properties can be explained by the analytical $V_{th}$ model we have derived for this structure. This model can be helpful to design appropriate PNT devices for a desired threshold voltage.

The p-type doped cap layer GaN MIS HEMT is an interesting new approach toward normally-off HEMTs. Here the threshold voltage strongly depends on the thickness and on the doping amount of the cap in the device.

# Chapter 6
# Proposed new designs of III-nitride HEMTs

## 6.1. Design of Cubic InGaN/InN Heterostructures for InN-Based High Electron Mobility Field Effect Transistors

### 6.1.1. Introduction

In recent years, intensive research has been conducted on III-nitride high electron mobility transistors (HEMTs). While most of the work has been focused on hexagonal GaN HEMTs [4-6], InN is another interesting III-nitride with potential for transistor applications. For hexagonal InN, excellent electron transport properties, such as mobilities up to 14,000 $cm^2/Vs$ and peak velocities up to $5\times10^7$ cm/s, have been predicted [130,130]. This makes InN a promising material for fast transistors. The growth of high-quality InN layers has been demonstrated by several groups [132,133] and theoretical studies on the layer design for hexagonal InGaN/InN HEMT structures can be found in the literature [134-137]. On the other hand, so far only a single paper reports on the fabrication and characterization of a hexagonal InN HEMT [138]. Possible reasons for the lack of experimental InN HEMTs are the still relatively immature InN technology, the high n-type background doping of epitaxial InN layers, and the pronounced surface accumulation in InN due to the location of the branch point energy (frequently called Fermi stabilization level) above the conduction band minimum [139,140] which makes it difficult to deplete the two-dimensional electron gas (2DEG) in the channels of hexagonal InN heterostructures. As has been shown in [137], either unacceptably large negative gate voltages or very thin InN channels are required to switch hexagonal InN HEMTs off. Moreover, the formation of an undesirable two-dimensional hole gas (2DHG) channel may deteriorate transistor operation. Therefore, the contribution of holes needs to be taken into account when simulating InN heterostructures.

As has been shown already for GaN, using cubic (zincblende) material instead of its hexagonal (wurtzite) counterpart is a viable option to realize HEMTs [141, 142]. While the electron transport properties in cubic InN are not as exciting as in hexagonal material, the predicted mobility of 6,000 $cm^2/Vs$ and peak velocity exceeding $3\times10^7$ cm/s [143, 144] are still very promising. Moreover, recently the epitaxial growth of cubic InN on different substrates has successfully been demonstrated [145]. These efforts have motivated us to perform the theoretical study of heterostructures based on cubic InN for application in HEMTs. We compare the behaviour of hexagonal and cubic InGaN/GaN structures and investigate how the layer

design influences the 2DEG sheet concentration, the formation of a parasitic channel in the InGaN barrier, and the formation of a 2DHG in cubic structures.

In this chapter, gated cubic InGaN/InN heterostructures for application in InN-based high electron mobility transistors are investigated theoretically. For the calculations, a Schrödinger-Poisson solver that considers both electrons and holes was used. With this tool, the formation of two-dimensional carrier gases in InGaN/InN structures is studied in detail and design issues for the InGaN barrier are investigated. The surface potentials and gate voltages at which the two-dimensional electron gas disappears (transistor off-state) and those where a two-dimensional hole gas is formed are extracted. It is shown that for certain surface potentials an undesirable saturation of the sheet density of the electron gas in the InN channel layer may occur. Options to enhance the electron sheet density in the channel and surface potential ranges for proper transistor operation are presented. Finally it is shown that because of the high unintentional n-type doping in InN buffer layer, cubic materials instead of hexagonal materials are useful for suited transistor operation.

The chapter is organized as follows. In Sec. 6.1.2, the simulated structures, the simulation approach, and the used material parameters are presented. In Sec. 6.1.3, the simulated results are presented. In Sec. 6.1.4, processing considerations for InGaN/InN HEMTs are presented and results for cubic and hexagonal HEMT structures are discussed. And finally Sec. 6.1.5 summarizes the chapter.

### 6.1.2. Studied structures and simulation approach

Figure 6.1 shows the InGaN/InN heterostructures considered in this work. Structure (a) on the left is a typical HEMT layer sequence having a homogeneous barrier with a thickness $t_{bar}$ and has been investigated for both cubic and hexagonal material. Due to pronounced spontaneous and piezoelectric polarization effects occurring in hexagonal InN heterostructures, high-density 2DEGs are formed without any doping. Therefore we assumed the barrier of the hexagonal version of structure (a) to be undoped. Since, on the other hand, such polarization effects are absent in cubic material, a homogeneous barrier doping has been considered for the cubic variant of structure (a).

Structure (b) on the right, in turn, has the layer design typical for delta-layer doped HEMTs, features a three-part $In_xGa_{1-x}N$ barrier with an overall thickness $t_{bar}$ and In-content $x$, and consists of cubic material. The delta-layer doped barrier portion with thickness $t_2$ is sandwiched

between two $In_xGa_{1-x}N$ layers of thickness $t_1$ and $t_3$. Except the barrier in the cubic variant of structure (a) and the delta-layer in structure (b), all other layers in the investigated heterostructures are assumed to be undoped and unintentional background doping is neglected.

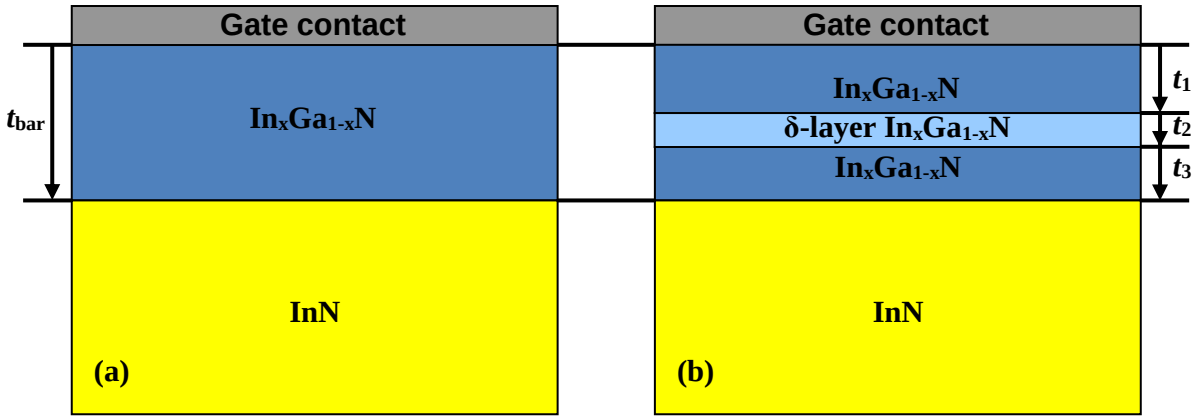


**Figure 6.1.** Layer structures investigated in the present work. Structure (a), the conventional structure (on the left) has been simulated for both cubic and hexagonal material. And structure (b), The delta-doped structure (on the right) consists of cubic InGaN and InN materials.

The present study is based on our in-house Schrödinger-Poisson solver that solves the Schrödinger and Poisson equations self-consistently in one dimension [75]. Although the study is focused on heterostructures for n-channel transistors, because of the narrow bandgap of InN the formation of a 2DHG may occur. Therefore the Schrödinger equation is solved for both electrons and holes [77].

The material parameters for the cubic and hexagonal phases of InN and $In_xGa_{1-x}N$ are taken from [78, 147]. To calculate the bandgap, a quadratic interpolation model has been used while all other needed parameters for $In_xGa_{1-x}N$ have been obtained by linear interpolation from the binary compounds InN and GaN. For the hexagonal structures, the InN layer is considered fully relaxed, and the barrier layers is assumed to be fully strained. The calculated polarization bound charge at the InGaN/GaN heterojunction for barrier In-contents of 0.10, 0.30, and 0.50 are $5.84\times10^{13}$q/cm$^2$, $4.46\times10^{13}$q/cm$^2$ and $3.13\times10^{13}$ $q$/cm$^2$ ($q$ is the elementary charge), respectively.

Table 6.1 summarizes important material parameters from [78, 147] used in the simulations exemplarily for cubic and hexagonal InN and $In_xGa_{1-x}N$ materials.

Tab. 6.1. Important material parameters used in this work. The effective masses are given in units of the electron rest mass $m_0$, the gap and the conduction band offset in eV, and the polarizations $P_{SP}$ and $P_{PZ}$ in q/cm$^2$.

| Material | | $\varepsilon_r$ | $m_{\parallel}^*$ | $m_{\perp}^*$ | $E_G$ | $\Delta E_C$ | $P_{SP}$ | $P_{PZ}$ |
|---|---|---|---|---|---|---|---|---|
| **InN** | **cub.** | 14.61 | 0.054 | 0.054 | 0.53 | 0 | 0 | 0 |
| | **hex.** | | 0.065 | 0.068 | 0.69 | 0 | -0.042 | 0 |
| **$In_{0.10}Ga_{0.90}N$** | **cub.** | 10.71 | 0.179 | 0.199 | 2.591 | 1.298 | 0 | 0 |
| | **hex.** | | 0.174 | 0.195 | 2.760 | 1.304 | -0.03147 | -0.10418 |
| **$In_{0.30}Ga_{0.70}N$** | **cub.** | 11.58 | 0.151 | 0.167 | 1.783 | 0.789 | 0 | 0 |
| | **hex** | | 0.150 | 0.167 | 1.950 | 0.794 | -0.02863 | -0.0849 |
| **$In_{0.50}Ga_{0.50}N$** | **cub.** | 12.46 | 0.123 | 0.135 | 1.175 | 0.406 | 0 | 0 |
| | **hex** | | 0.126 | 0.139 | 1.340 | 0.409 | -0.02875 | -0.0634 |

## 6.1.3. Results and discussion

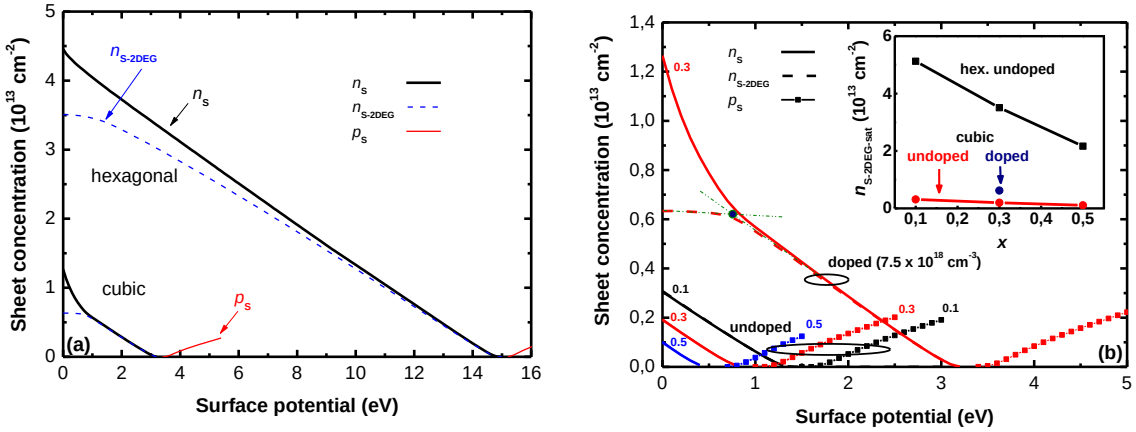


**Figure. 6.2.** Calculated carrier sheet densities as a function of the surface potential for InGaN (20 nm)/InN heterostructures of Figure. 1a with (a) In contents in the barrier 0.3 and homogeneously barrier doped cubic and undoed hexagonal (b) undoped cubic and different In contents in the barrier and homogeneously barrier doped cubic. For each case three curves are shown: Overall electron and hole sheet density (full lines and full lines with symbols respectively) and 2DEG sheet density (dashed lines). Inset (b) is 2DEG sheet concentration corresponding to start saturation point ($n_{S\text{-}2DEG\text{-}sat}$) as a function of the barrier In content with undoped cubic (the $n_{S\text{-}2DEG\text{-}sat}$ at zero surface potential have been taken) and hexagonal heterostructures.

We start the discussion by considering the hexagonal and cubic InGaN/InN heterostructures of a 20 nm and 0.3 In-content InGaN barrier (Figure 6.1(a)). Figure 6.2(a) shows the calculated carrier sheet concentrations of such heterostructure of an undoped InGaN barrier hexagonal and a homogeneously doped (with $7.5\times10^{18}$ $cm^{-3}$) barrier cubic InGaN/InN structure as a function of surface potential $E_{C0}$, i.e., the position of the conduction band edge at the gate contact. The applied gate voltage $V_G$ is related to the surface potential by

$$V_G = -(E_{C0} - \Phi_B)/q \qquad 6\text{-}1$$

where $\Phi_B$ is the Schottky barrier height and $q$ is the elementary charge. For each structure, three curves are shown, the overall electron sheet concentrations $n_S$ (thick full lines), the concentration of the 2DEG electrons $n_{S\text{-}2DEG}$ and the overall hole concentration $p_S$. While most of the electrons are located in the 2DEG in the InN layer, in particular at low surface potentials a sizeable portion of $n_S$ occurs in the barrier and the 2DEG sheet concentration shows saturation. As can be seen, both $n_S$ and $n_{S\text{-}2DEG}$ are much higher in the hexagonal structure, in spite of the undoped barrier, due to the strong polarization in hexagonal InN-based heterostructures. Thereby a much higher surface potential (i.e., a more negative gate voltage) is needed to deplete the 2DEG in the hexagonal structure (around 14.5 eV) compared to the cubic structure (3 eV). The disappearance of the 2DEG corresponds to the HEMT's off-state. For further increasing surface potentials, the structures remain off initially, while for $E_{C0}$ above 3.6 eV in the cubic and above 15.3 eV in the hexagonal structure a hole channel with a hole sheet concentration $p_S$ (thin full lines) is formed.

Figure 6.2(b) shows the carrier sheet densities for three cubic structures with undoped barrier (thickness 20 nm, varying In-content x in the barrier) and for the doped cubic structure from Figure 6.2(a). Without doping, obviously the 2DEG sheet density and the surface potential for switch off are significantly lower for the undoped structures. Moreover, an increasing In-content x in the barrier leads to a decreasing 2DEG sheet density due to the decreasing conduction band offset for increasing x. However, $V_G$ ($V_{th}$) would not be changed, although the Schottky barrier height decreases with increasing In-content.

At this point we introduce several characteristic parameters for the transistor operation and use the results of the doped cubic structure from Figure 6.2(b) for the explanation. At low surface potentials, the 2DEG sheet density in the channel $n_{S\text{-}2DEG}$ is saturated and shows only a very

weak dependence on $E_{C0}$ while between $E_{C0}$ = 1eV and 3 eV, i.e., in the on-state, a linear slope of the curve $n_{S\text{-}2DEG}$ ($E_{C0}$) is observed. We linearly extrapolate the $n_{S\text{-}2DEG}$ curve of these two regions (thin dash-double dot lines in Figure 6.2(b)) and define the transition between saturation and on-state at the intersection of the two extrapolations (hollow dot in Figure 6.2(b)) as the saturation point of the HEMT. The surface potential at this point is designated as $E_{C0\text{-}sat}$ and the corresponding 2DEG sheet concentration as $n_{S\text{-}2DEG\text{-}sat}$. The surface potential where the 2DEG disappears (the condition is $n_{S\text{-}2DEG} = 10^{10}$ cm$^{-2}$) is designated as threshold potential for the n-channel $E_{C0\text{-}th\text{-}n}$ and the surface potential where the hole channel start to form (condition $p_S = 10^{10}$ cm$^{-2}$) is defined as $E_{C0\text{-}th\text{-}p}$.

Using the parameters introduced above, we can define the following four distinct operating regions for the cubic InN HEMT structure: (a) 2DEG saturation region for $E_{C0}$ between zero and $E_{C0\text{-}sat}$, (b) transistor operation on-state between $E_{C0\text{-}sat}$ and $E_{C0\text{-}th\text{-}n}$, (c) transistor off-state between $E_{C0\text{-}th\text{-}n}$ and $E_{C0\text{-}th\text{-}p}$, and (d) p-channel operation for $E_{C0} > E_{C0\text{-}th\text{-}p}$. It should be noted that the p-channel operation is not point of our interest in this study, where we concentrated on n-channel HEMTs.

Another obvious in Figure 6.2(b) for undoped structure is no difference between electron sheet density for whole device $n_S$ and 2DEG sheet density $n_{S\text{-}2DEG}$ i.e. there is not any kind of saturation in the barrier till at very small surface potential. Moreover, a hole channel is formed approximately after 0.4eV from deplete the electron channel. Such an effect has already been observed for hexagonal InN-based heterostructures in [142]. Due to the smaller gap of cubic InN (0.53eV for cubic InN compared to 0.69eV for hexagonal InN), the surface potential range between the disappearance of the 2DEG and the formation of the 2DHG ($\Delta E_{C0\text{-}th}$) is smaller for the cubic structures compared to that mentioned for GaN heterostructure (0.7eV) in [142]. Although, this small range is enough to become clear separate between on- and off-states in the n-channel HEMT.

The clear difference between undoped hexageonal and cubic InGaN/InN (inset of Figure 6.2(b)) is, due to the missing polarization in cubic heterostructures, the electron densities $n_S$ and $n_{S\text{-}2DEG}$ for the undoped cubic structures are significantly lower of one order of magnitude than in the hexagonal structures. This deficiency in $n_S$ or $n_{S\text{-}2DEG}$ can at least partially be compensated by doping the barrier of cubic structures. As can be seen in (Figure 6.2(b)), the doping of the barrier leads to a significantly increased electron sheet density and a much higher surface potential needed to deplete the 2DEG. In addition, the on-state of the homogeneously doped $n_{S\text{-}}$

$_{2DEG}$ ($E_{C0}$) curve (dashed line) shows two clearly distinguishable regions, first a linear increase of the 2DEG sheet density decreasing $E_{C0}$, followed by the saturation region at small $E_{C0}$ where the 2DEG sheet density remains almost constant ($E_{C0\text{-}2DEG\text{-}sat}$ = 0.8 eV separates this two regions). As an example, for cubic structure $In_{0.3}GaN_{0.7}$/InN with barrier thickness 20nm, the overall electron sheet density $n_S$ is $7.9\times10^{12}$ cm$^{-2}$ for the $N_D$ = 7.5x10$^{18}$ cm$^{-3}$ homogenously doped structure compared to $1.1\times10^{12}$ cm$^{-2}$ for the undoped barrier at the same surface potential of 0.5 eV. Unfortunately, however, at low surface potentials not all electrons of the doped structure are located in the 2DEG. Instead, the 2DEG sheet density (dashed line) tends to saturate and a conductive region with high electron concentration forms in the barrier. At 0.5 eV surface potential (previous example), the 2DEG sheet density $n_{S\text{-}2DEG}$ is $6.3\times10^{12}$ cm$^{-2}$, i.e., $1.6\times10^{12}$ electrons/cm$^2$ are located in the barrier and form an undesirable parasitic channel in the barrier (such saturation is described in [148] for AlGaAs/GaAs).

Finally, a Figure of merit for the control of the 2DEG sheet density by the surface potential designated as gate capacitance and defined as

$$C_G = \frac{\Delta n_{S-2DEG}}{\left|E_{C0-th\text{-}n} - E_{C0\text{-}2DEG-sat}\right|} \qquad 6\text{-}2$$

is introduced.

Where, $\Delta n_{S-2DEG} = n_{S-2DEG\text{-}sat} - n_{S-th\text{-}n} \approx n_{S-2DEG\text{-}sat}$, here $n_{S-th\text{-}n} = 10^{10}\,\text{cm}^{-2}$ is negligible compared to $n_{S-2DEG\text{-}sat}$. For fast transistor operation, high $g_m$ is recommended. This can be easily achieved by increasing $\Delta n_{S-2DEG}$ or decreasing the difference of surface potential of the on-state region $\left|E_{C0-th\text{-}n} - E_{C0\text{-}2DEG-sat}\right|$.

By depends on this definition, the results of Figure 6.2 show nearly the same $C_G$ for on-state region for hexagoenal and cubic structures (about $2.5\times10^{12}$ cm$^{-2}$eV$^{-1}$). That is clear, since $t_{bar}$ and $\varepsilon_{bar}$ are the same.

Another possibility to achieve doping in the barrier is by using delta-doped layers instead of homogeneous barrier doping. Figure 6.3(a) shows the results for different cubic structures with a 20 nm $In_{0.3}Ga_{0.7}N$ barrier, 5 nm doped δ-layer and a fixed spacers thickness $t_1$ = 12 nm and $t_3$ = 3 nm for varying the doping concentration $N_D$ of the delta-layer from 0.5x10$^{19}$ cm$^{-3}$ to 5x 10$^{19}$ cm$^{-3}$. As can be seen in Figure 6.3(a), with increasing doping levels, $n_S$ can be increased as well as $E_{C0\text{-}2DEG\text{-}sat}$ and $E_{C0\text{-}th\text{-}n}$ values.

To make a fair comparison, let us take the curves of the homogeneously doped and δ-doped structures with the same number of dopants in the barrier ($7.5\times10^{18}$ $cm^{-3}$ and $3\times10^{19}$ $cm^{-3}$ respectively) as shown in Figure 6.3(b) as an example. In both structures, the slope of the $n_{S\text{-}2DEG}$ ($E_{C0}$) curves is nearly the same between $E_{C0\text{-}2DEG\text{-}sat}$ and $E_{C0\text{-}th\text{-}n}$ ($2.5\times10^{12}$ $cm^{-2}eV^{-1}$), merely for the delta-doped structure, the values of saturation and threshold surface potentials are about 1 eV higher and the 2DEG sheet density at $E_{C0\text{-}2DEG\text{-}sat}$ is slightly larger. In general, for the Δ-doped structure, the slope of the $n_S$ ($E_{C0}$) curves in saturation region and between $E_{C0\text{-}2DEG\text{-}sat}$ and $E_{C0\text{-}th\text{-}n}$ is nearly the same (about $2.5\times10^{12}$ $cm^{-2}eV^{-1}$) for $N_D$ >$1x10^{19}$ $cm^{-3}$. However, for the homogeneous doped structure, is observed for surface potentials below the saturation point $E_{C0\text{-}2DEG\text{-}sat}$, , a larger slope than that in on-state region (about $4\times10^{12}$ $cm^{-2}eV^{-1}$).

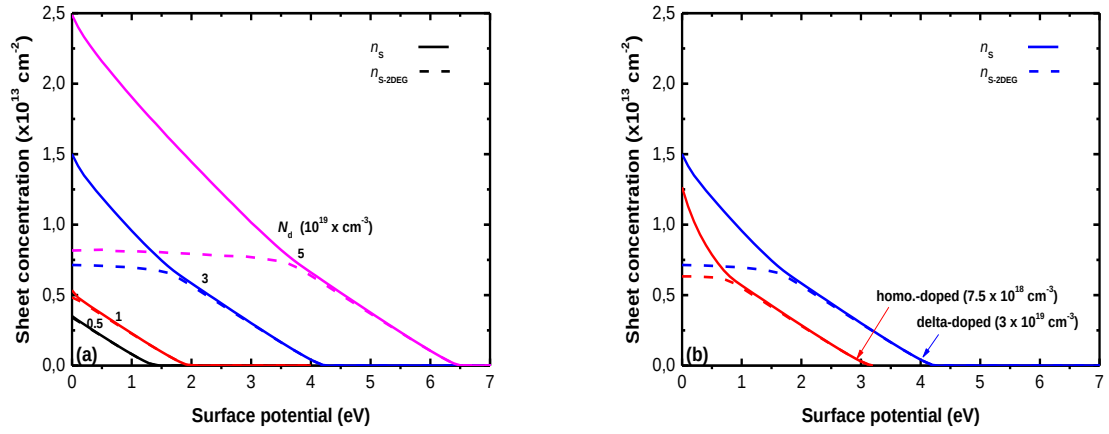


**Figure 6.3.** Calculated carrier sheet densities as a function of the applied surface potential for cubic $In_{0.3}Ga_{0.7}N$/InN heterostructures of Figure. 1b with barrier's parts $t_1$ = 12 nm, $t_2$ = 5 nm, and $t_3$ = 3 nm and different delta-layer doping levels. The numbers at the curves indicate the doping concentration in $cm^{-3}$. For each case three curves are shown: Overall electron and 2DEG sheet density (full and dashed lines respectively).

The reason of this observed saturation is as a result of formation of a parasitic channel in the barrier. As can be seen from the calculated band diagram (Figure 6.4), together with the electron distributions, for both kinds of the barrier doping (homogeneous, delta-layer) in the cubic InGaN/InN heterostructure, the conduction band edge in the barrier shows a minimum value within the doped layer, and at considered surface potential becomes below the Fermi level $E_F$. And where the conduction band in (and close to) the n-type layer is populated by electrons, the negative electron charge in the barrier tends to compensate the positive charge of the ionized donors, which leads to the observed saturation of the 2DEG density $n_{S\text{-}2DEG}$ and these two slopes in $n_s$ ($E_{C0}$) curves. Since the parasitic channel is located closer to the gate electrode than the 2DEG at the InGaN/InN heterojunction, the gate capacitance, which is inversely proportional

to the distance between gate and channel, becomes larger when the parasitic channel is formed. This explains the visible increase of the slope of the overall $n_s$ ($E_{C0}$) curves in Figures 6.2 and 6.3 once $n_{S\text{-}2DEG}$ saturates.

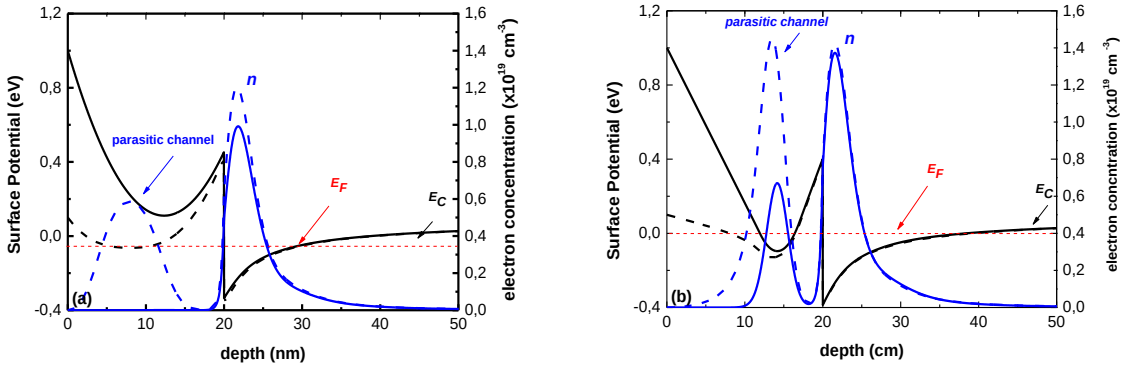


**Figure 6.4.** Calculated band diagram and free carrier distribution along the depth of a fully ionization doped cubic InGaN/InN heterstructure at 0.1 eV (dashed line) and 1 eV (full line) with (a) homogeneous doping concentration $N_D$ = 7.5 x $10^{18}$ $cm^{-3}$ and (b) delta-layer doping concentration $N_D$ = 3 x $10^{19}$ $cm^{-3}$.

Another factor can be modified, the position of delta-doped layer in the barrier. Figure 6.5 shows $n_s(E_{C0})$-curves for cubic $In_{0.3}Ga_{0.7}N$/InN heterstructures with a 20nm barrier thicknesses and a 5nm delta-layer with doped 3x$10^{19}$ $cm^{-3}$ and the spacer thicknesses $t_3$ have been varied from 1nm (near InGaN/InN heterojunction) to 10nm (near gate metal).

It is obvious, that there is a kind of redistributing of the carries in the layers, where is all $n_s(E_{C0})$-curves meeting nearly at one point 1.5 eV, i.e. independent from the position of the delta-layer. On the other hand, the shift of this layer towards the gate contact gives a decrease in $n_{S\text{-}2DEG\text{-}sat}$ and $E_{C0\text{-}th\text{-}n}$ and a steeper slope of overall $n_S$ above $E_{C0\text{-}sat}$. If we put every slope under the scope, we find two different linear trends related to the difference between saturation and on-state regions. As an example, the curves $n_s$ ($E_{C0}$) for the extreme cases $t_3$ = 1nm and $t_3$ = 10nm curves have for saturation region the values $g_m$ about 2.5×$10^{12}$ $cm^{-2}eV^{-1}$ and 7.7×$10^{12}$ $cm^{-2}eV^{-1}$ respectively, but for on-state the same slope 2.5×$10^{12}$ $cm^{-2}eV^{-1}$. It should be noted that the gate potential has better control of the overall $n_S$, However, the observed saturation of the electron sheet densities at $E_{C0,2DEG\text{-}sat}$ in the InN layer is undesirable for transistor application since it leads to a degradation of the transconductance, and hence to a significant deterioration of the device performance. The reason is the considerable lower mobility in the doped barrier layer compared to that within the 2DEG. Thus, the usable operation range of the applied surface potential will be limited.

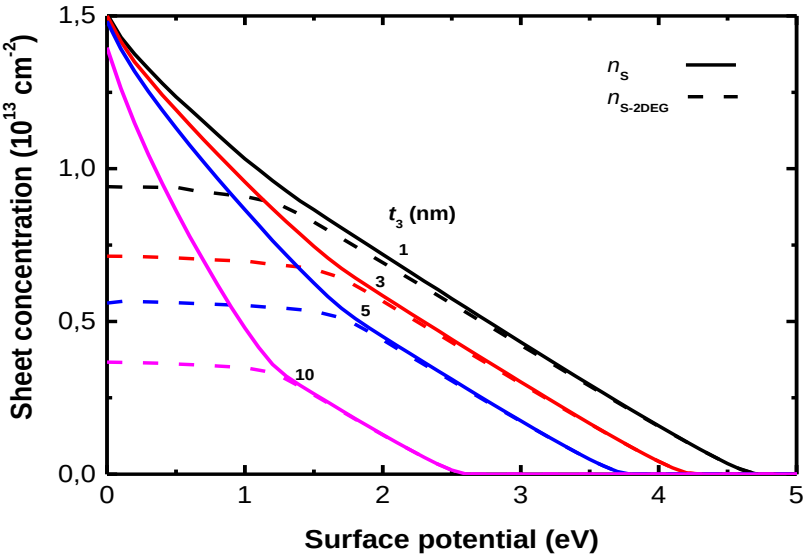


**Figure 6.5.** Calculated carrier sheet densities as a function of the applied surface potential for cubic $In_{0.3}Ga_{0.7}N$ (20 nm)/InN heterostructures of Figure. 1b with 5 nm n-type delta-doped barrier layer and doping level $N_D$ = $3x10^{19}$ $cm^{-3}$and different spacer thickness of the delta-layer to the heterojunction. The numbers at the curves indicate the spacer thickness ($t_3$) in nm. For each case three curves are shown: Overall electron and 2DEG sheet density (full lines dashed lines respectively).

Finally, for simulated study, Figure 6.6 summarized $\Delta n_{S\text{-}2DEG}$ (or $n_{S\text{-}2DEG\text{-}sat}$) and $\left|E_{C0-th\text{-}n} - E_{C0\text{-}2DEG-sat}\right|$ values of all cubic and hexagonal InGaN/InN heterostructures results considered in this work. As can be seen, the most important result is that the changing of several design parameters (doping, position, …) for cubic as well as for hexagonal heterostructures shows the similar slope fitting of all points with a linear function (dashed line), when conserved barrier thickness to a constant value of 20 nm, due to the gate capacitance is dominated by the electrostatic capacitance of the barrier layer. This means, with decreasing $\Delta n_{S\text{-}2DEG}$, the usable operation range $\Delta E_{C0}$ becomes lower in the same degree. Possible design option to increase gate capacitance and then transconductance is varying barrier thickness as shown in Figure 6.6. When decreasing whole barrier thickness, by decreasing $t_1$ only, from 20nm to 8nm (at $t_2$ = 5 nm and $t_3$ = 3 nm), the gate capacitance shifts from $2.5\times10^{12}$ $cm^{-2}eV^{-1}$ to $5\times10^{12}$ $cm^{-2}eV^{-1}$. Figure 6 indicate that cubic structures can be an alternative to hexagonal InGaN/InN heterostructures at low voltage operation points under the same design conditions of In-content, doping levels, barrier thicknesses. We recommended for operation surface potential the value $\left|E_{C0-th\text{-}n} - E_{C0\text{-}2DEG-sat}\right|/2$ to stay in normal transistor operation region.

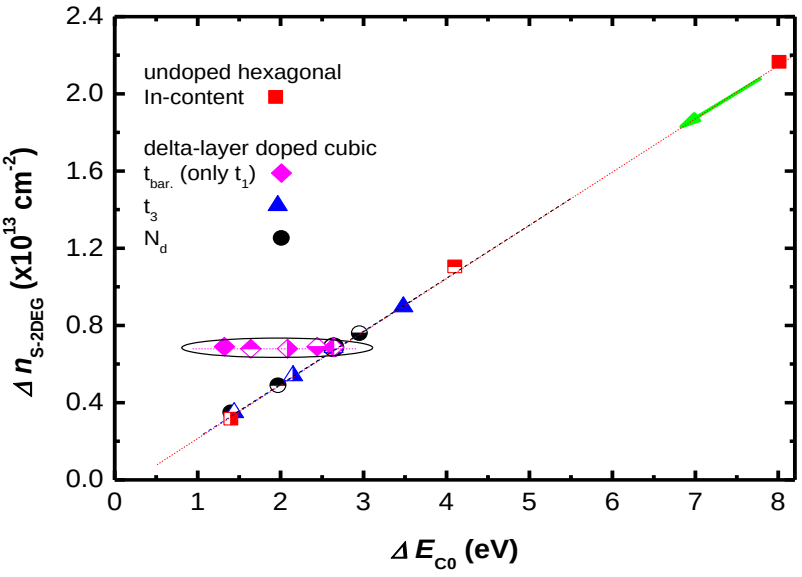


**Figure 6.6.** Extracted 2DEG electron sheet densities $\Delta n_{S\text{-}2DEG}$ as a function of applied surface potential between $E_{C0\text{-}sat}$ and $E_{C0\text{-}th\text{-}n}$ for different delta-layer doped cubic and fully undoped hexagonal InGaN/InN heterostructures. For every case, in the direct direction of the green arrow, is shown: a) undoed hexagonal with In-contents x in the barrier 0.5, 0.7 and 0.9 respectively (rectangle), b) delta-layer doped barrier cubic $In_{0.3}Ga_{0.7}N$/InN heterostructures with doping level $N_D = 3x10^{19}$ cm$^{-3}$ and barrier's parts $t_1 = 12$ nm, $t_2 = 5$ nm and a different spacer thickness $t_3$ of the delta-layer to the heterojunction 1, 3, 5 and 10 nm respectively (triangle), c) with barrier's parts $t_1 = 12$ nm, $t_2 = 5$ nm, and $t_3 = 3$ nm and different delta-layer doping levels 5, 3, 1 and 0.5 x$10^{19}$ cm$^{-3}$ respectively (circle) and d) doping level $N_D = 3x10^{19}$ cm$^{-3}$ and barrier's parts $t_2 = 5$ nm, and $t_3 = 3$ nm and a different overall barrier 8, 11, 15, 18 and 20 nm respectively from extreme link point to extreme right point (rhombus).

Now the question, which material has advantage on the other, cubic or hexagonal? To answer this, processing considerations ought to take into account.

### 6.1.4. Processing Considerations

It should be noted that unintentional doping introduced in InN buffer in experimental devices may lead to undesirable results. For that, it is useful to find an approach for processing or manufacturing considerations by assuming the InN buffer layer to be n-type doped with $N_D$ = $1\times10^{18}$ cm$^{-3}$, a concentration typical for epitaxial InN layers, due to this consideration, we suggest additional structure Figure 6.7(b) on Figure 6.1 and the In-content was 0.3 in all InGaN layers considered here.

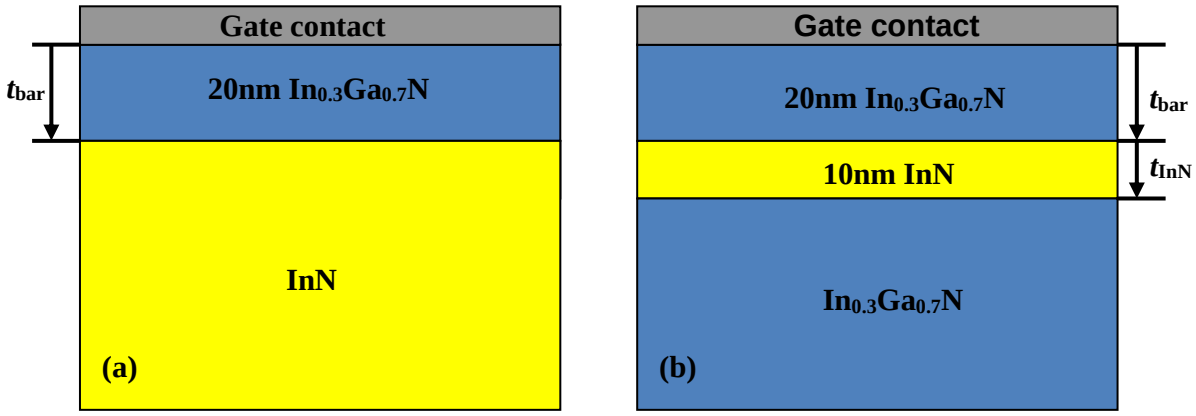


**Figure 6.7.** Layer structures investigated in this work: (a) A 20nm thin strained $In_xGa_{1-x}N$ barrier on bulk InN and (b) structures using thin InN layers on $In_xGa_{1-x}N$ buffers. The gate is modeled by Dirichlet boundary conditions.

Due to the doping, the picture of previous studies changes dramatically: for hexagonal structures, the electron concentration cannot fully be controlled by the gate anymore (Figure 6.8(a)). For the considered structures, $n_S$ saturates at a very high value. A device with a similar transfer characteristic would not be suited for transistors, because it does not switch off.

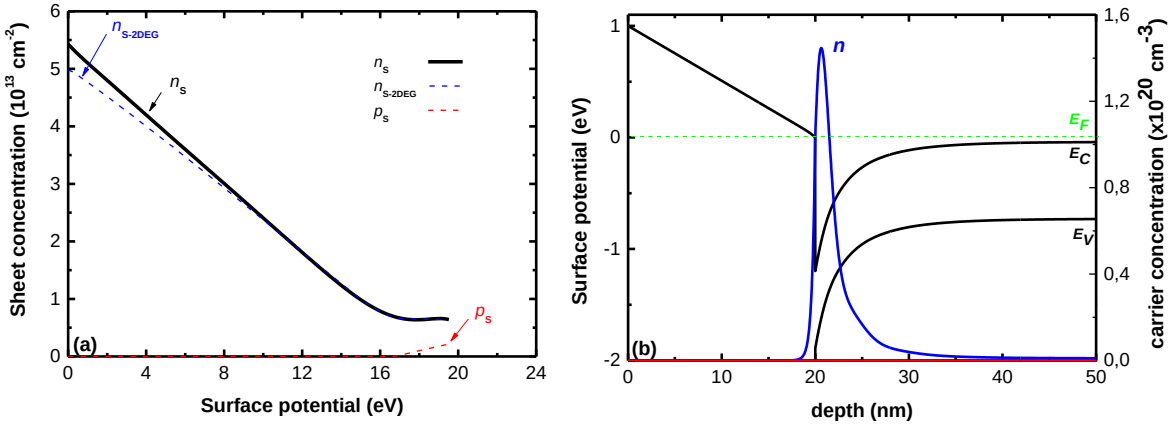


**Figure 6.8.** a) calculated electron and hole densities as function of the applied surface potential for structure of Figure 6.7(a) with $10^{18}$ $cm^{-3}$ n-type doped InN. b) band diagram and electron and hole distributions in the on-state.

Figure 6.9(a) shows $n_S(E_{C0})$ curves for a structure with 10nm InN thickness and was calculated assuming fully relaxed InN layers. It can be seen that $t_{InN}$ ought to be reduced to ~10nm to avoid the negative bound charge at the back interface, which creates a hole channel to guarantee good switch-off behaviour [137]. Figure 6.9(b) shows the band diagram and the electron distribution. Although the InN-layer is very thin, one can clearly see two peaks in the electron density related

to each interface. The second electron channel at the bulk interface can only be controlled by the gate if the InN layer is thin enough.

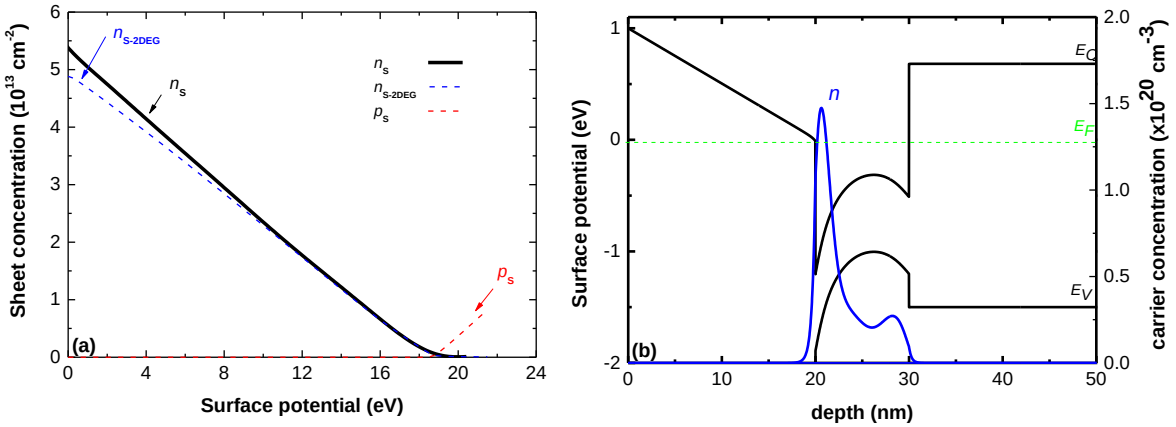


**Figure 6.9.** Hexagonal InGaN/InN/InGaN structures with relaxed InN layers. a) calculated electron and hole densities as function of the applied surface potential for structure of Figure 6.7(b) with $10^{18}$ $cm^{-3}$ n-type doped InN. b) band diagram and electron and hole distributions in the on-state.

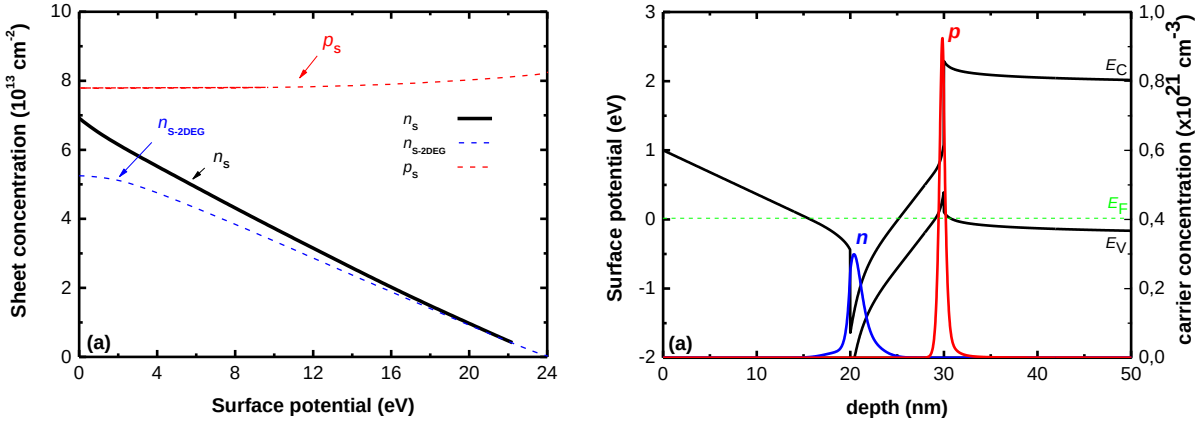


**Figure. 6.10.** Hexagonal InGaN/InN/InGaN structures with strained InN layers. a) calculated electron and hole densities as function of the applied surface potential for structure of Figure 6.7(b) with $10^{18}$ $cm^{-3}$ n-type doped InN. b) band diagram and electron and hole distributions in the on-state.

This thinner in InN-layer makes to float on the surface the strained issue. Which is the bound charge at the back interface is dominated by piezoelectric polarization which is much stronger than spontaneous polarization and it has the opposite sign. Figure 6.10(a) shows $n_S(E_{C0})$ curves for structures with 10nm InN thickness were calculated assuming fully strained InN layers. It can be seen that the piezoelectric polarization leads to large $p_S$, which can be larger than $n_S$ even

in the on-state. In Figure 6.10(b) it can be seen, that a 2DEG and 2DHG are formed at the top interface and the back interface respectively.

Such a layer structure is not suited for transistors since a persistent hole channel always exists between source and drain. Therefore it will be impossible to switch off the drain current. However, the InN layer must be extremely thin, to switch off the hole channel with small $n_S$ in the order of $10^{12}cm^{-2}$ and smaller [137]. One of a good option to avoid this disadvantage, extremely thin barrier, is use a cubic material as a barrier. Where there is no polarization effect, which is the main reason of this disadvantage of hexagonal materials. The Figures 6.11(a) and 6.12(a) by replacing hexagonal materials by cubic materials for homogeneously and δ-layer barrier doped respectively are showing a clear switch off case. The related band diagram and electron distribution for both structures Figures. 11(b) and 12(b) biased in the on-state shows a desirable carrier distribution for transistor operation, since neither a second electron channel nor a 2DHG is created at the back interface, and the 2DEG is closely confined at the InGaN/InN interface.

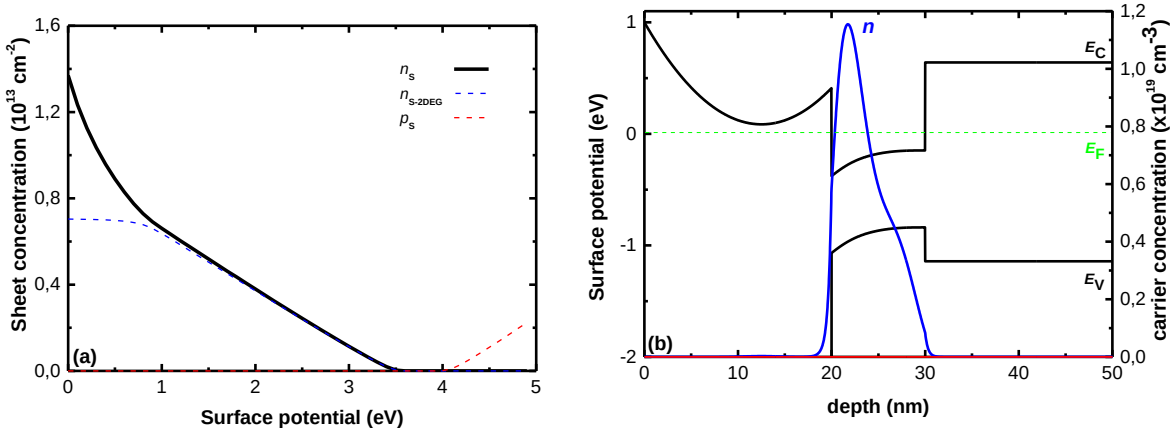


**Figure 6.11.** a) calculated electron and hole densities as function of the applied surface potential for homogeneous-doped barrier layer of cubic structure of Figure 6.7(b) with $10^{18}$ cm$^{-3}$ n-type doped InN. b) band diagram and electron and hole distributions in the on-state.

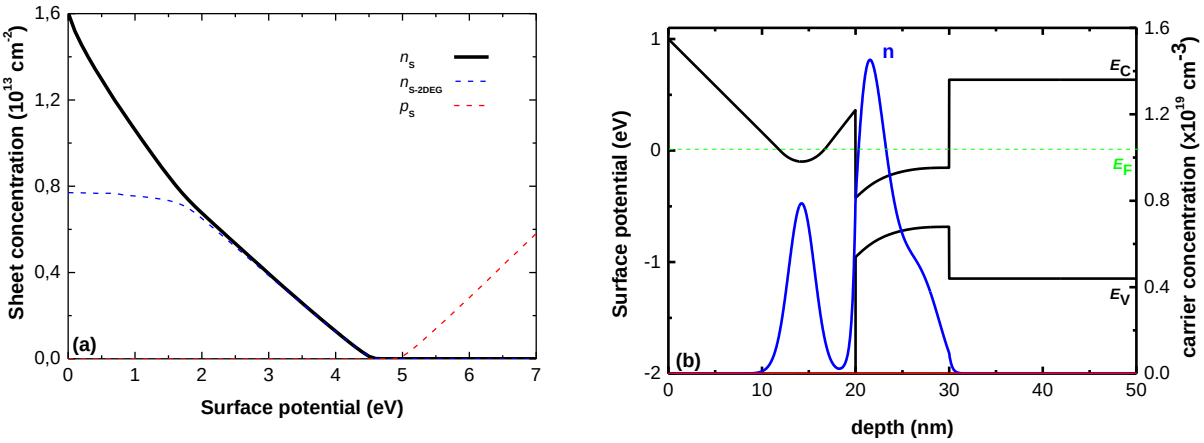


**Figure 6.12.** a) calculated electron and hole densities as function of the applied surface potential for delta-doped barrier layer of cubic structure of Figure 6.7(b) with $10^{18}$ $cm^{-3}$ n-type doped InN. b) band diagram and electron and hole distributions in the on-state.

The advantage of use the cubic material stead of hexagonal appears clearly for undoped InGaN barrier structure. This is illustrated in Figure 6.13 for the structure (b) in Figure 6.7 with $10^{18}$ $cm^{-3}$ n-type doped InN, where carrier distribution is shown a clear switch off with one electron channel in whole InN buffer.

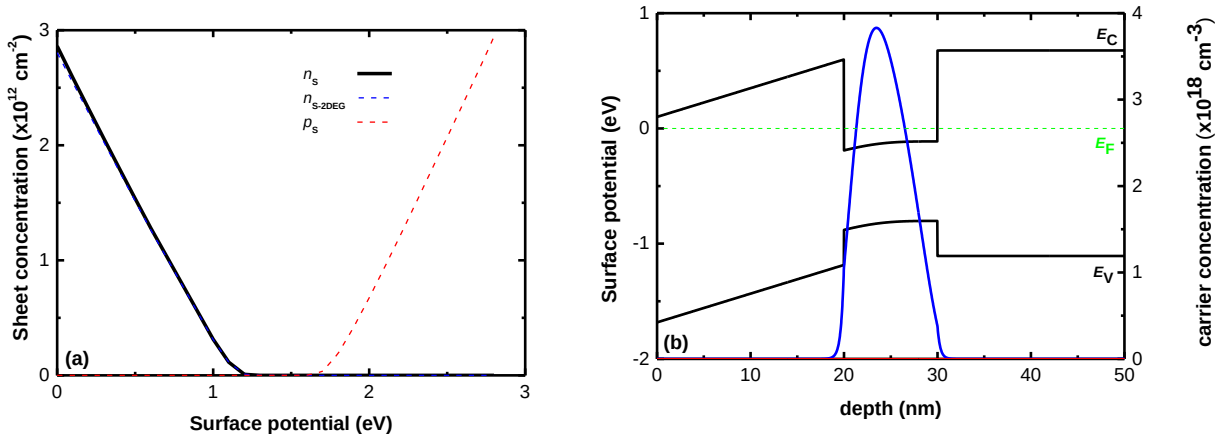


**Figure 6.13.** a) calculated electron and hole densities as function of the applied surface potential for undoped barrier cubic structure of Figure 6.7(b) with $10^{18}$ $cm^{-3}$ n-type doped InN. b) band diagram and electron and hole distributions in the on-state.

### 6.1.5. Conclusion

The study of formation of two-dimensional carrier gases in InN HEMTs reveals that the choice of a proper layer sequence is crucial. Due to the absence of polarisation effects in cubic InGaN/InN heterostructures, the designer adjusts the 2DEG density via the doping of the InGaN

barrier. Two possible doping options can be used, the homogenous or the delta-layer doped profiles. The latter gives the maximum of the electron sheet density when the doping level is high as possible whereas the position of the delta-layer is located close to the heterojunction contact. However, due to doping of the barrier for certain surface potentials, an undesirable saturation of the sheet density of the electron gas in the InN channel layer and a parasitic channel in the InGaN barrier may occur.

Special attention was paid to the gate capacitance $C_G$ in on-state region, i.e. the alternation of the electron sheet density in the InN layer depending on the change of the surface potential, and the usable voltage operation range. It has observed that, while the thickness of the InGaN barrier does not changed, the transconductance for well-designed cubic InGaN/InN heterostructures should be approximately the same for low operation voltage compared to undoped hexagonal structures with a very high In-content.

On the other hand, the fabrication process, especially the doping concentration of the buffer, can be critical to the optimum HEMT design. The above results show that cubic InN-doped HEMT are promising for low power applications.

## 6.2. The Formation of Two-Dimensional Electron Gases with High Sheet Density in AlScN/GaN and AlYN/GaN Heterostructures

### 6.2.1. Introduction

Today, AlGaN/GaN heterostructures are extensively used in high electron mobility transistors (HEMT) for radio frequency power amplifiers [6, 149] and power switches [7, 150]. To achieve a low on-state resistance of the transistor, which is beneficial for both applications, a characteristic feature of AlGaN/GaN heterostructures, namely the formation of a two-dimensional electron gas (2DEG) with high sheet density at the interface between the strained AlGaN barrier and the GaN channel layer, is exploited. Due to strong polarization effects, 2DEG sheet densities exceeding $10^{13}$ $cm^{-2}$ are easily achieved, even without intentionally doping the AlGaN barrier.

While GaN HEMTs with $Al_xGa_{1-x}N$ barriers ($x$ is the Al content) are now well established and commercially available, alternative barrier materials offering stronger polarizations are explored to achieve higher 2DEG sheet densities. Two promising candidates that recently have attracted considerable attention are AlScN and AlYN. AlScN films have been prepared by reactive magnetron sputtering on different substrates including sapphire [151, 152] and MgO [152-154]. As a big step towards the realization of AlScN/GaN HEMTs, recently high-quality wurtzite $Al_{0.86}Sc_{0.14}N$/GaN heterostructures have successfully been grown by molecular beam epitaxy and a 2DEG with high sheet density ($3.4\times10^{13}$ $cm^{-2}$) and an electron mobility exceeding 900 $cm^2/Vs$ at the AlScN/GaN interface has been demonstrated [155]. First results on the growth of AlYN by reactive magnetron sputtering on Si and sapphire have also been reported [156, 157], while AlYN/GaN heterostructures suitable for HEMTs have not been demonstrated yet.

First-principle calculations revealed that $Al_xSc_{1-x}N$ with $x$ around 0.82 and $Al_xY_{1-x}N$ with $x$ around 0.84 are lattice-matched to wurtzite GaN [158-161]. Moreover, spontaneous polarizations much larger compared to $Al_xGa_{1-x}N$ with $x$ around 0.3, which is a typical barrier composition in AlGaN/GaN HEMTs, have been predicted for both AlScN and AlYN lattice matched to GaN, [160-163]. This raised the expectation that lattice matched AlScN/GaN and AlYN/GaN heterostructures with extremely high 2DEGs sheet densities suitable for high-performance HEMTs with low on-state resistance should be feasible. A quantitative analysis of the 2DEG formation in AlScN/GaN and AlYN/GaN heterostructures, however, is still missing. This deficiency is the motivation for the present work where we perform a detailed study of the 2DEG formation in AlScN/GaN and AlYN/GaN structures by means of quantum-mechanical

simulations and compare the results with those obtained for conventional AlGaN/GaN structures.

In this section, the formation of two-dimensional electron gases (2DEGs) in lattice-matched AlScN/GaN and AlYN/GaN heterostructures is investigated by numerical self-consistent solutions of the Schrödinger and Poisson equations. The electron concentration profiles and the resulting 2DEG sheet densities in these heterostructures are calculated and compared to those occurring at AlGaN/GaN interfaces. The combined effect of the strong polarization-induced bound charges and the large conduction band offsets at the AlScN/GaN and AlYN/GaN heterojunctions results in the formation of 2DEGs with very high electron sheet densities. 2DEG sheet densities about 4 … 5 times as large as those in $Al_{0.3}Ga_{0.7}N$/GaN structures are calculated for the AlScN/GaN and AlYN/GaN heterostructures. Our results demonstrate the potential of AlScN and AlYN barriers for GaN-based high electron mobility transistors.

### 6.2.2. Studied structures and simulation approach

To calculate the electron distribution in heterostructures, the Schrödinger equation for electrons and Poisson's equation have to be solved self-consistently in the growth direction, i.e., along the c axis, of the heterostructures, which is called *z* direction in the following. For that purpose we use our in-house Schrödinger-Poisson solver [77, 78]. The Schrödinger equation for electrons is expressed as

$$\left[-\frac{\hbar^2}{2}\frac{d}{dz}\left(\frac{1}{m_{||}^{*}(z)}\frac{d}{dz}\right)-q\phi(z)+\Delta E_C(z)\right]\psi_i(z) \;=\; E_i\,\psi_i(z) \qquad 6\text{-}3$$

where $E_i$ and $\psi_i(z)$ are the energy level and wave function of the *i*th subband, $m_{||}^{*}(z)$ is electron effective mass in the *z*-direction, $\phi(z)$ is the electrostatic potential, and $\Delta E_C(z)$ is the conduction band offset at the heterointerface and zero elsewhere in the structure. In its general form, Poisson's equation in the *z* direction is given by

$$\frac{d}{dz}\left[-\varepsilon(z)\frac{d\phi(z)}{dz}+P(z)\right] \;=\; q\left[N_D^{+}(z)-N_A^{-}(z)+p(z)-n(z)\right] \qquad 6\text{-}4$$

where $P(z)$ is the overall polarization, i.e., the sum of spontaneous and piezoelectric polarizations, $N_D^{+}(z)$ and $N_A^{-}(z)$ are the ionized donor and acceptor concentrations, $\varepsilon(z)$ is the dielectric constant, and $n(z)$ and $p(z)$ are the electron and hole concentrations. Since for simplicity in the present study we assume only undoped materials, $N_D^{+}$ and $N_A^{-}$ are zero.

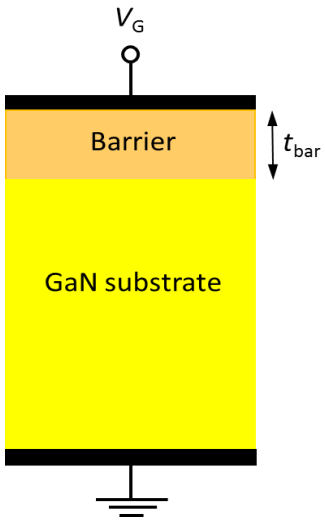


**Figure 6.14.** Schematic of the investigated heterostructures.

Figure 6.14 shows schematically the design of the heterostructures investigated in the present work. It consists (from top to bottom) of a Schottky gate, a barrier layer with a thickness $t_{bar}$, a thick GaN substrate, and a grounded back-side contact. The following three types of barriers are considered: (i) Strained $Al_{0.3}Ga_{0.7}N$ barriers with Al contents between 0.25 and 0.35 are very popular for AlGaN/GaN HEMTs [165-168]. (ii) $Al_{0.86}Sc_{0.14}N$ lattice-matched to GaN. (iii) $Al_{0.84}Sc_{0.16}N$ lattice-matched to GaN. The selection of the material parameters needed for the simulations turned out to be difficult since a consistent parameter set for the AlGaN, AlScN, and AlYN compounds does not exist yet and the values for several parameters cannot be found at all in the literature. Therefore, it was inevitable to take the parameters from various references and to make reasonable estimates for the unknown parameters. Table 6.2 summarizes the parameters selected for the three barrier materials and for the GaN substrate, and in Table 6.3 the conduction band offsets and the polarization-induced bound charges at the heterojunctions are listed. Note that the piezoelectric polarization (which is induced by strain) is zero for the $Al_{0.86}Sc_{0.14}N$ and $Al_{0.84}Sc_{0.16}N$ barriers since they are lattice matched to the GaN substrate while it is nonzero for the strained $Al_{0.3}Ga_{0.7}N$ barrier. Nevertheless, the polarization-induced bound interface charge $\sigma$ at the AlGaN/GaN interface is much lower compared to that of the AlScN/GaN and AlYN/GaN structures due to the strong spontaneous polarizations in AlScN and AlYN.

| Material | $\varepsilon_r$ | $m^*_{\parallel}$ ($m_0$) | $m^*_{\perp}$ ($m_0$) | $E_G$ (eV) | $P^{SP}$ (C/m$^2$) | $P^{PZ}$ (C/m$^2$) |
|---|---|---|---|---|---|---|
| $Al_{0.3}Ga_{0.7}N$ | 10.29 | 0.227 | 0.245 | 4.03 | -0.0464 | -0.0098 |
| $Al_{0.86}Sc_{0.14}N$ | 9.59 | 0.313 | 0.318 | 5.14 | -0.10968 | -0.01434 |
| $Al_{0.84}Y_{0.16}N$ | 12.13 | 0.312 | 0.318 | 4.96 | -0.1300 | 0 |
| GaN | 10.28 | 0.186 | 0.209 | 3.40 | -0.0340 | 0 |

**Tab. 6.2.** Dielectric constant $\varepsilon_r$, electron effective masses parallel ($m^*_{\parallel}$) and perpendicular ($m^*_{\perp}$) to the *z* direction, bandgap $E_G$, spontaneous polarization ($P^{SP}$), and piezoelectric polarization ($P^{PZ}$) polarization for the three barriers on GaN and for the GaN substrate ($m_0$ is the electron rest mass).

| Heterojunction | $\Delta E_C$ (eV) | $\sigma$ ($q$/cm$^2$) |
|---|---|---|
| $Al_{0.3}Ga_{0.7}N$/GaN | 0.441 | $1.39 \times 10^{13}$ |
| $Al_{0.86}Sc_{0.14}N$/GaN | 1.594 | $7.24 \times 10^{13}$ |
| $Al_{0.84}Y_{0.16}N$/GaN | 1.090 | $5.99 \times 10^{13}$ |

**Tab. 6.3.** Conduction band offset $\Delta E_C$ and polarization-induced bound interface charge $\sigma$ occurring at the barrier/GaN heterojunctions.

For the AlGaN-GaN system, the electron effective masses are taken from [78], the dielectric constants as well as the spontaneous and piezoelectric polarizations from [10], the bandgap from [10] assuming bandgaps of 6.2 eV for AlN [169] and 3.4 eV for GaN [170], and the conduction band offset from [171]. The material parameters for the system AlScN-ScN are obtained by linear interpolation using (i) the AlN parameters from [171] for $\varepsilon_r$, from [170] for $m^*$, and from [169] for $E_G$, and (ii) the ScN parameters from [172] for $\varepsilon_r$ and $m^*$ and from [170] for $E_G$. The conduction band offset is calculated based on the data from [169,170], and the spontaneous polarization is obtained from the model described in [160]. Finally, the dielectric constant and the electron effective masses for AlYN are obtained by linear interpolation using the between AlN parameters from [10,78] and the YN parameters from [158, 173]. The bandgap is obtained by a polynomial fit of the $E_G$ data from [157,168] and the spontaneous polarization is calculated using the model from [160]. For all barriers, the conduction band offset $\Delta E_C$ at the barrier/GaN junction is assumed to be 70% of the bandgap difference $\Delta E_G$ [81].

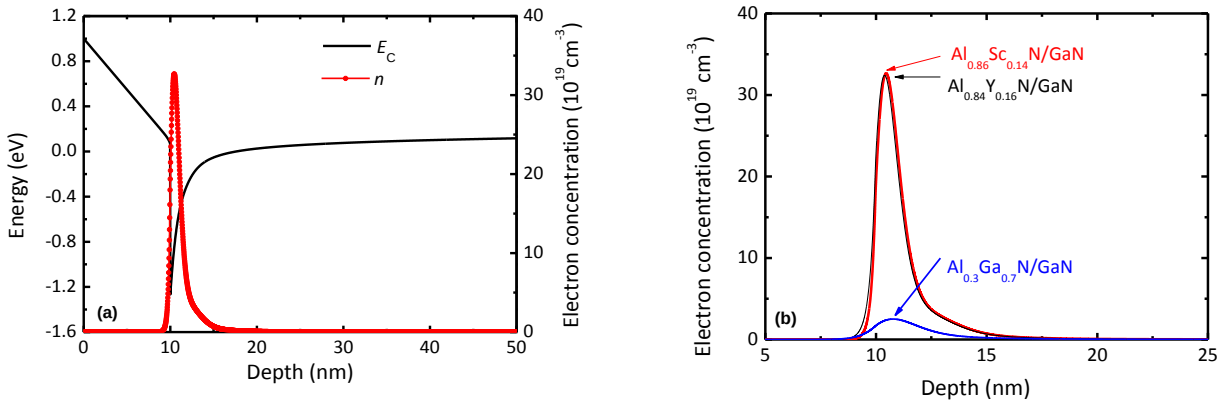


**Figure 6.15**. (a) Simulated conduction band edge $E_C$ (black line) and electron concentration (red line with symbols) in an $Al_{0.86}Sc_{0.14}N$/GaN structure. (b) Electron concentration in the AlScN/GaN structure from Figure. 2(a) and for the $Al_{0.84}Y_{0.16}N$/GaN and $Al_{0.3}Ga_{0.7}N$ structures. For all cases, the barrier thickness is 10 nm and the applied surface potential is 1 eV.

Figure 6.15(a) shows the simulated conduction band edge and electron concentration in an $Al_{0.86}Sc_{0.14}N$/GaN structure with a barrier thickness of 10 nm as a function of depth for a surface potential $E_{C0}$ of 1 eV. The surface potential $E_{C0}$ is defined as the conduction band edge in the barrier at the gate contact and is related to the applied gate voltage $V_G$ by

$$V_G = -(E_{C0} - \Phi_B)/q \qquad 6\text{-}5$$

where $\Phi_B$ is the Schottky barrier and $q$ is the elementary charge. Note that a value around 1.2-1.5 eV for a Schottky barrier of a metal-$Al_{0.3}Ga_{0.7}N$ contact is well established [10] while data for the Schottky barrier for AlScN and AlYN is not available yet. It can be seen that, caused by the combination of the large conduction band offset and the strong spontaneous polarization in the barrier, a high-density DEG forms in the deep and narrow potential well at the barrier/GaN interface. Figure 6.15(b) compares the electron concentrations of the three investigated heterostructures. Obviously much higher electron concentrations are achieved in the $Al_{0.86}Sc_{0.14}N$/GaN and $Al_{0.84}Y_{0.16}N$/GaN structures compared to the conventional $Al_{0.3}Ga_{0.7}N$/GaN structure due to the stronger polarizations in $Al_{0.77}Sc_{0.23}N$ and $Al_{0.84}Y_{0.16}N$ compared to $Al_{0.3}Ga_{0.7}N$ and the resulting higher polarization-induced bound interface charges.

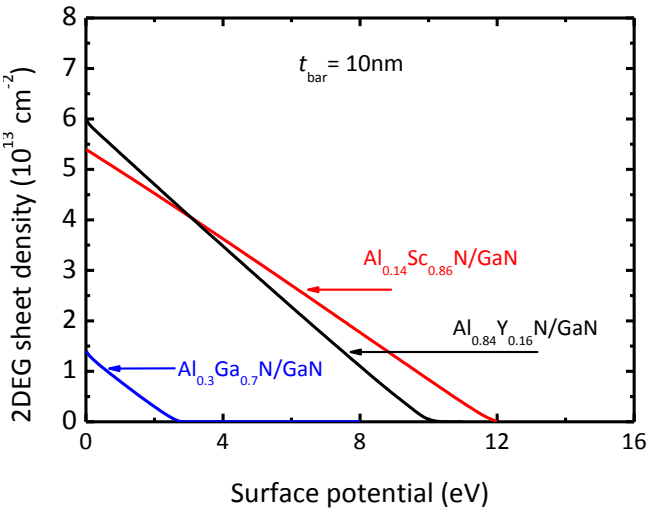


**Figure 6.16.** Calculated 2DEG sheet density for the three heterostructures from Figure 6.16(b) vs surface potential.

In Figure 6.16 we plot the calculated 2DEG sheet densities for the three heterostructures from Figure.6.15(b) as a function of surface potential. As to be expected, for a given surface potential the sheet density $n_{sh}$ is highest for $Al_{0.77}Sc_{0.23}N$/GaN, followed by $Al_{0.84}Y_{0.16}N$/GaN and $Al_{0.3}Ga_{0.7}N$/GaN. It should be noted, however, that the higher 2DEG sheet densities of the AlScN and AlYN structures come at the expense of higher surface potentials needed to deplete the 2DEG (which are designated as threshold surface potential $E_{C0\text{-th}}$ in the following), i.e., more negative gate voltages are needed to turn the 2DEG channel off (designated as threshold voltage $V_{th}$). This represents a problem for applications where HEMTs with zero or even positive threshold voltage, i.e., normally-off HEMTs, are needed. Next we consider the slope $\Delta n_{sh}/\Delta E_{C0}$ of the $n_{sh}$ vs $E_{C0}$ curves, which can be interpreted as a transconductance indicating the effectivity of the gate control. The curve for $Al_{0.84}Y_{0.16}N$/GaN shows the largest slope (around $6.1 \times 10^{12}$ cm$^{-2}$eV$^{-1}$), followed by $Al_{0.3}Ga_{0.7}N$/GaN (around $5.4 \times 10^{12}$ cm$^{-2}$eV$^{-1}$) and finally the $Al_{0.84}Sc_{0.14}N$/GaN structure ($5.0 \times 10^{12}$ cm$^{-2}$eV$^{-1}$), and the ratio of the slopes is almost identical to the ratio of the dielectric constants of the barriers (12.13 : 10.29 : 9.59). Finally, the 2DEG sheet density for zero surface potential is almost identical to the polarization-induced bound charge. Thus, the polarization has the strongest impact on the 2DEG formation while other properties of the heterostructure, such as barrier dielectric constant, conduction band offset and carrier effective mass, have only a minor effect.

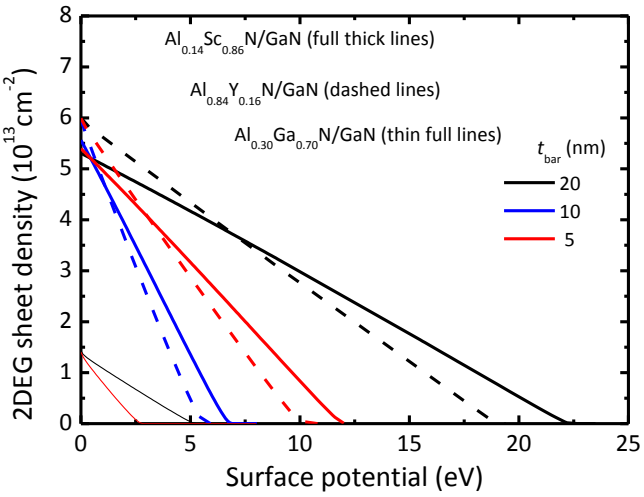


**Figure 6.17.** Calculated 2DEG sheet density as a function of surface potential for $Al_{0.86}Sc_{0.14}N$/GaN, $Al_{0.84}Y_{0.16}N$/GaN, and $Al_{0.3}Ga_{0.7}N$/GaN heterostructures with different barrier thicknesses $t_{bar}$. For the AlScN/GaN and AlYN/GaN structures, the $n_{sh}$ vs $E_{C0}$ curves are shown for 20, 10, and 5 nm thick barriers. For AlGaN/GaN, only the sheet densities for $t_{bar}$ = 20 and 10 nm are shown since for thinner barriers the 2DEG is already depleted for zero surface potential.

It is well established that by thinning the barrier the threshold surface potential can be decreased and the corresponding threshold voltage can be shifted towards zero [168, 174]. Figure 6.17 shows the effect of the barrier thickness on the 2DEG sheet density. Decreasing the barrier thickness leads to significantly reduced threshold surface potentials while the 2DEG sheet density for zero $E_{C0}$ is not affected. The $Al_{0.86}Sc_{014}N$/GaN structure with a 3-nm barrier and the $Al_{0.84}Y_{0.16}N$/GaN with a barrier thickness of 5 nm, for example, show practically the same $E_{C0\text{-}th}$ as the $Al_{0.3}Ga_{0.7}N$/GaN structure, but offer much higher 2DEG sheet densities and transconductances. Moreover, when using $Al_xSc_{1-x}N$/GaN or $Al_xY_{1-x}N$/GaN structures with strained barriers having properly adjusted Al contents and barrier thicknesses, positive threshold voltages can be achieved making normally-off AlScN/GaN and AlYN/GaN HEMTs with higher 2DEG sheet densities in the on-state and thus lower on-resistances than their AlGaN/GaN counterparts feasible.

In conclusion, we have investigated the 2DEG formation in lattice matched AlScN/GaN and AlYN/GaN heterostructures by means of quantum-mechanical simulations. It has been shown that, caused by the strong spontaneous polarization in AlScN and AlYN, extremely high 2DEG sheet densities, which by far exceed those in $Al_{0.3}Ga_{0.7}N$/GaN, can be achieved in $Al_{0.86}Sc_{0.14}N$/GaN and $Al_{0.84}Y_{0.16}N$/GaN structures. The downside of these high sheet densities are, however, larger threshold surface potentials and more negative threshold voltages

compared to $Al_{0.3}Ga_{0.7}N$/GaN structures with the same barrier thickness. Using thinner $Al_{0.86}Sc_{0.14}N$ and $Al_{0.84}Y_{0.16}N$ barriers, on the other hand, mitigates this problem significantly. The results of the present study show that AlScN/GaN and AlYN/GaN HEMTs represent promising alternatives to the conventional AlGaN/GaN HEMTs, particularly if a low on-state resistance is a primary design target.

## Conclusions and Outlook

This work presents a new advanced design methods and new layout structures, which are developed to achieve nonclassical GaN HEMTs. We can conclude this thesis as the follow:

- The formation of 2DHGs in GaN/AlGaN/GaN heterostructures has been investigated theoretically by numerical simulation and a new analytical model developed in the present work. It has been shown that for certain combinations of bias conditions and layer design coexisting 2DEGs and 2DHG are formed in the structure where the 2DHG is located at the cap/barrier interface and the 2DEG is at the barrier/bulk interface. Once a 2DHG is created, the effect of the gate voltage on the 2DEG diminishes rapidly and a saturation of the 2DEG density is observed.
- The formation of second channel in AlGaN/GaN/AlGaN/GaN heterostructures has been investigated theoretically by numerical simulation and a new technique developed in the present work. It has been shown that for certain combinations of bias conditions and layer design coexisting two channels can be formed in AlGaN2/GaN2/AlGaN1/GaN1 structures where the both channels are located at the AlGaN1/ GaN1 and AlGaN2/ GaN2. Once a second channel is created, the effect of the gate voltage on the first 2DEG diminishes rapidly and a saturation of the drain current is observed. Special attention was paid to the structure 2 as novel inverter with vertical-build technique.
- We have theoretically investigated three possible options for a normally-off GaN HEMT technology, i.e. the MIS HEMT and two alternatives, the so-called piezo neutralization technique (PNT) and p-type doped cap layer GaN MIS HEMT.

We find that the threshold voltage of the GaN/AlGaN/GaN MIS HEMT strongly depends on the oxide/semiconductor interface charge in the device. This can be explained by an analytical threshold voltage model that we have developed for the MIS HEMT structure. The model can be used to extract the oxide interface charge from measured threshold voltages. For the experimental MIS HEMTs fabricated at IAF, this charge is found to be positive having the same value as the bound polarization charge at the AlGaN/GaN interface. This positive charge compensates the negative bound charge at the GaN cap/AlGaN interface leading to the observed negative threshold voltage of the experimental devices.

The two alternative normally-off concepts are more stable regarding threshold voltage adjustment. In particular the PNT concept turns out to be very robust against process fluctuations. Its main advantage is that the threshold voltage does not depend on critical

parameters like the PNT layer and the channel layer thicknesses. These properties can be explained by the analytical Vth model we have derived for this structure. This model can be helpful to design appropriate PNT devices for a desired threshold voltage.

The p-type doped cap layer GaN MIS HEMT is an interesting new approach toward normally-off HEMTs. Here the threshold voltage strongly depends on the thickness and on the doping amount of the cap in the device.

- The study of formation of two-dimensional carrier gases in InN HEMTs reveals that the choice of a proper layer sequence is crucial. Due to the absence of polarisation effects in cubic InGaN/InN heterostructures, the designer adjusts the 2DEG density via the doping of the InGaN barrier. Two possible doping options can be used, the homogenous or the delta-layer doped profiles. The latter gives the maximum of the electron sheet density when the doping level is high as possible whereas the position of the delta-layer is located close to the heterojunction contact. However, due to doping of the barrier for certain surface potentials, an undesirable saturation of the sheet density of the electron gas in the InN channel layer and a parasitic channel in the InGaN barrier may occur.
- Special attention was paid to the gate capacitance $C_G$ in on-state region, i.e. the alternation of the electron sheet density in the InN layer depending on the change of the surface potential, and the usable voltage operation range. It has observed that, while the thickness of the InGaN barrier does not changed, the transconductance for well-designed cubic InGaN/InN heterostructures should be approximately the same for low operation voltage compared to undoped hexagonal structures with a very high In-content.
- On the other hand, the fabrication process specially the doping concentration of buffer can be critical to determine the optimum HEMT design. The above results show that cubic InN-doped HEMT are promising low operation voltage device for low power applications.
- we have investigated the 2DEG formation in lattice matched AlScN/GaN and AlYN/GaN heterostructures by means of quantum-mechanical simulations. It has been shown that, caused by the strong spontaneous polarization in AlScN and AlYN, extremely high 2DEG sheet densities, which by far exceed those in $Al_{0.3}Ga_{0.7}N$/GaN, can be achieved in $Al_{0.86}Sc_{0.14}N$/GaN and $Al_{0.84}Y_{0.16}N$/GaN structures. The downside of these high sheet densities are, however, larger threshold surface potentials and more negative threshold voltages compared to $Al_{0.3}Ga_{0.7}N$/GaN structures with the same barrier thickness. Using thinner $Al_{0.86}Sc_{0.14}N$ and $Al_{0.84}Y_{0.16}N$ barriers, on the other hand, mitigates this problem significantly. The results of the present study show that AlScN/GaN and AlYN/GaN

HEMTs represent promising alternatives to the conventional AlGaN/GaN HEMTs, particularly if a low on-state resistance is a primary design target.

## References


[1] D. J. W. Sjobbema, Aachen: Elektor-Verlag, 1998.

[2] M. A. Khan, A. Bhattarai, J. N. Kuznia, and D. T. Olson, Applied Physics Letters, vol. 63, pp. 1214 -1215, 1993.

[3] M. A. Khan, J. N. Kuznia, D. T. Olson, W. J. Schaff, J. W. Burm, and M. S. Shur, Applied Physics Letters, vol. 65, no. 9, pp. 1121-1123, 1994.

[4] U. K. Mishra, L. Shen, T. E. Kazior, and Y.-F. Wu, Proc. IEEE 96, 287-305, 2008.

[5] E. Bahat-Treidel et al., IEEE Trans. Electron Devices 57, 3050-3058, 2010

[6] R. S. Pengelly, S. M. Wood, J. W. Milligan, S. T. Sheppard, and W. L. Pribble, IEEE Trans. Microwave Theory Techn., 1764-1783, 2012.

[7] N. Ikeda et al., Proc. IEEE 98, 1151-1161, 2010.

[8] T. Imada, M. Kanamura, and T. Kikkawa, Proc. IPEC, 1027-1033, 2010.

[9] O. Ambacher, J. Smart, J. R. Shealy, N. G. Weimann, K. Chu, M. Murphy, R. Dimitrov, L. Wittmer, M. Stutzmann, W. Rieger, and J. Hilsenbeck, J. Appl. Phys. 85, 3222, 1999.

[10] O. Ambacher, J. Majewski, C. Miskys, A. Link, M. Hermann, M. Eickhoff, M. Stutzmann, F. Bernardini, V. Fiorentini, V. Tilak, B. Schaff, and L. F. Eastman, J. Phys.: Condens. Matter 14, 3399, 2002.

[11] Semiconductor Today, "GaN power devices market to grow at 24.5% to $2.6bn in 2022", www.semiconductortoday.com/news_items/2016/feb/marketandmarkets_230216.shtml, 2016.

[12] K. Shinohara et al., Tech. Dig. IEDM, 617-620, 2012.

[13] T. Ueda, T. Tanaka, and D. Ueda, Proc. ESSDERC, 36-41, 2011.

[14] O. Hilt et al., Proc. ISPSD, 239-242, 2011.

[15] D. Maier, M. Alomari, N. Grandjean, J. Carlin, M. Diforte-Poisson, C. Dua, S. Delage and E. Kohn, IEEE Electron Device Lett., vol. 33, no. 7, pp. 985–987, Jul., 2012.

[16] www.gansystems.com/why_gallium_nitride_new.php.

[17] H. Okumura, Japanese Journal of Applied Physics, vol. 45, no. 10A, pp. 7565- 7586, 2006.

[18] R. J. Trew, Proceedings of the IEEE, vol. 90, pp. 1032-1047, June 2002.

[19] R. Kemerley, H. Wallace and M. Yoder, Proceedings of the IEEE, vol. 90, no. 6, pp. 1059-1064, June 2002.

[20] E. Johnson, IRE International Convention Record, vol. 13, pp. 27 - 34, March 1965.

[21] B. J. Baliga, Journal of Applied Physics, vol. 53, pp. 1759 - 1764, 1982.

[22] B. J. Baliga, IEEE Electron Device Letters, vol. 10, no. 10, pp. 455-457, 1989.

[23] R. W. Keyes, IEEE Proceedings, vol. 10, p. 225, 1972.

[24] A. Trampert, O. Brandt, and Ploog.K.H., in "Gallium Nitride (GaN) ", I, Vol. 50. J. I. Pankove and T. D. Moustakas, Eds. San Diego, CA: Academic press, pp. 167-192, 1998.

[25] H. Morkoç, Wiley-VCH Verlag GmbH & Co. KGaA, Vol. 1, 2008.

[26] M. Kočan, Rheinisch-Westfälische Technische Hochschule, Aachen, PhD Thesis, 2003.

[27] F. Bernardini, V. Fiorentini and D. Vanderbilt, Physical Review B, vol. 63, no. 19, p. 193201, 2001.

[28] F. Bernardini, V. Fiorentini and D. Vanderbilt, Phys. Rev. B, vol. 56, no. 16, p. R10024, 1997.

[29] S. M. Sze and K. K. Ng, 3ed. Hoboken, New Jersey: John Wiley & Sons, Inc., 2007.

[30] O. Ambacher, Journal of Physics D: Applied Physics, vol. 31, no. 20, pp. 2653-2710, 1998.

[31] J. P. Ibbetson, P. T. Fini, K. D. Ness, S. P. DenBaars, J. S. Speck, and U. K. Mishra, Applied Physics Letters, vol. 77, no. 2, pp. 250-252, 2000.

[32] W. R. L. Lambrecht, K. Kim, S. N. Rashkeev, and B. Segall, Materials Research Society Symposium Proceedings, vol. 395, p. 455, 1996.

[33] O. Ambacher, M. Eickhoff, A. Link, M. Hermann, M. Stutzmann, F. Bernardini, V. Fiorentini, Y.Smorchkova, J. Speck, U. Mishra, W. Schaff, V. Tilak, and L. F. Eastman, Physica Status Solidi (c), vol. 0, no. 6, pp. 1878- 1907, 2003.

[34] M. A. Khan, Q. Chen, C. J. Sun, M. Shur and B. Gelmont, Applied Physics Letters, vol. 67, no. 10, pp. 1429-1431, 1995.

[35] M.Shur, B.Gelmont and K. Asif, J. Electron. Mater., vol. 25, no. 5, pp. 777-785, 1996.

[36] W. Walukiewicz, H. E. Ruda, J. Lagowski, and H. C. Gatos, Phys. Rev. B, vol. 30, no. 8, p. 4571,1984.

[37] C. Wood and D. Jena, New York, NY, Springer, 2008.

[38] I.P. Smorchkova, L. Chen, T. Mates, L. Shen, S. Heikman, B. Moran, S. Keller, S.P. DenBaars, J.S. Speck and U.K. Mishra, Journal of Applied Physics 90,5196, 2001.

[39] M. Miyoshi, T. Egawa and H. Ishikawa, Solid-State Electronics, Volume 50, Issues 9–10, 2006.

[40] M. Farahmand, C. Garetto, E. Bellotti, K. F. Brennan, M. Goano, E. Ghillino, G. Ghione, J. D. Albrecht, and P. P. Ruden, Electron Devices, IEEE Transactions on, vol. 48, no. 3, pp. 535-542, 2001.

[41] M. A. Littlejohn, J. R. Hauser, and T. H. Glisson, Applied Physics Letters, vol. 26, no. 11, pp. 625-627, June1975.

[42] B. Gelmont, K. Kim, and M. Shur, Journal of Applied Physics, vol. 74, no. 3, pp. 1818-1821, Aug.1993.

[43] U. V. Bhapkar and M. S. Shur, Journal of Applied Physics, vol. 82, no. 4, pp. 1649-1655,1997.

[44] G. Gonzalez, "Microwave Transistor Amplifiers: Analysis and Design", 2ed. Upper Saddle River, New Jersey: Prentice Hall, 1997.

[45] B. J. Baliga, Electron Devices, IEEE vol. 43, no. 10, pp. 1717-1731, 1996.

[46] K. Takahashi, H. Kuribayashi, T. Kawashima, S. Wakimoto, K. Mochizuki, and H. Nakazawa, Power Semiconductor Devices and IC's, ISPSD, IEEE International Symposium, pp. 1-4, 2006.

[47] S. Yamauchi, T. Shibata, S. Nogami, T. Yamaoka, Y. Hattori, and H. Yamaguchi, Power Semiconductor Devices and IC's, ISPSD, IEEE International Symposium, pp. 1-4, 2006.

[48] J. M. Hancock and I. Zverev, Infineon CoolMOS Application Note, 2000.

[49] C. Rochefort and R. van Dalen, Power Semiconductor Devices and ICs, Proceedings. ISPSD, The 17th International Symposium, pp. 35-38, 2005.

[50] T. P. Chow and R. Tyagi, Electron Devices, IEEE Transactions on, vol. 41, no. 8, pp. 1481-1483,1994.

[51] W. Saito, Y. Takada, M. Kuraguchi, K. Tsuda, I. Omura, T. Ogura, and H. Ohashi, Electron Devices, IEEE Transactions on, vol. 50, no. 12, pp. 2528-2531, 2003.

[52] S. Yoshida, J. Li, T. Wada, and H. Takehara, Power Semiconductor Devices and ICs, 2003. Proceedings. ISPSD '03. 2003 IEEE 15th International Symposium on, pp. 58-61, 2003.

[53] U. K. Mishra and J. Singh, "Semiconductor Device Physics and Design Fundamentals of Power Semiconductor Devices", Springer US, 2008.

[54] I. Daumiller, C. Kirchner, M. Kamp, K. J. Ebeling, and E. Kohn, IEEE Electron Device Lett., vol. 20, no. 9, pp. 448–450, 1999.

[55] P. G. Neudeck, R. S. Okojie and L. Y. Chen, Proc IEEE, 90(6): 1065, 2002.

[56] M. Micovic, T. Tsen, M. Hu, P. Hashimoto, P. J. Willadsen, I. Milosavljevic, A. Schmitz, M. Antcliffe, D. Zhender, J. S. Moon, W. S. Wong, and D. Chow, Electron. Lett., vol. 41, no. 19, pp. 1081–1083, Sep. 2005.

[57] Y. Cai, Z. Cheng, C. W. Tang, K. J. Chen, and K. M. Lau, IEDM Tech. Dig., Washington, DC, Dec. 4–7, 2005.

[58] S. Long and S. E. Butner, New York: McGraw-Hill, 1990.

[59] Y. Cai, Y. G. Zhou, K. M. Lau et al., IEEE Trans Electron Devices, 53(9): 2207, 2006.

[60] C. Zeng, "GaN MOSFETs Structures and Process Flows for Logic Applications", A dissertation submitted to the Graduate Faculty of North Carolina State University In partial fulfillment of the Requirements for the Degree of Doctor of Philosophy, 2006.

[61] B. J. Baliga, "Fundamentals of Power Semiconductor Devices", Springer US, 2008.

[62] B.J. Baliga, Springer, "Advanced High Voltage Power Device Concepts", 2011.

[63] B. J. Baliga, "Gallium nitride devices for power electronic applications", Semicond. Sci. Technol. 28, 2013.

[64] S. J. Pearton, C. R. Abernathy, and F. Ren, Sensors and Spintronics. London, Springer London, 2006.

[65] J. Wuerfl et al., Vo. 51, Issues 9–11, 2011.

[66] E. Bahat-Treidel et al., IEEE Trans Electron Dev, 55(12), 3354–9, 2008.

[67] C. Poblenz et al., J Vac Sci Technol B, Microelectron Process Phenom, 22(3):1145–9, 2004.

[68] J. Derluyn et al., IEDM Tech Dig.,157–60, 2009.

[69] X. Huili et al., IEEE Electron Dev Lett., 25(4):161–3, 2004.

[70] E. Bahat-Treidel et al., IEEE Trans Electron Dev., 1208–16, 2010.

[71] Y. Dora et al., IEEE Electron Dev Lett., 27(9):713–5, 2006.

[72] H. Umeda et al., IEDM Tech Dig., 480–3, 2010.

[73] R. Zhytnytska et al., Proceedings of the 35th workshop on compound semiconductor devices and integrated circuits, ISBN 978-88-8080- 123-8, p.163–4, 2011.

[74] W. Saito et al., IEEE Trans Electron Dev., 159–64, 2005.

[75] V. M. Polyakov and F. Schwierz, J. Appl. Phys. 98, 023709, 2005.

[76] ATLAS User's Manual – Device Simulation Software, Silvaco International, 2010.

[77] N. Al Mustafa, R. Granzner, V. M. Polyakov, J. Racko, M. Mikolášek, J. Breza and F. Schwierz, J. Appl. Phys. 111 044512, 2012.

[78] P. Rinke, M. Winkelnkemper, A. Qteish, B. Bimberg, J. Neugebauer and M. Scheffler, Phys. Rev. B 77, 075202, 2008.

[79] M. E. Levinshtein, S. L. Rumyantsev, and M. S. Shur, Wiley, New York, 2001.

[80] R. F. Pierret, Massachusetts: Addison Wesley Longman, pp.792, 1996.

[81] O. Ambacher, B. Foutz, J. Smart, J. R. Shealy, N. G. Weimann, K. Chu, M. Murphy, A. J. Sierakowski, W. J. Schaff, L. F. Eastman, R. Dimitrov, A. Mitchell and M. Stutzmann, J. Appl. Phys., vol. 87, pp. 334-344, 2000.

[82] I. P. Smorchkova, C. R. Elsass, J. P. Ibbetson, R. Vetury, B. Heying, P. Fini, E. Haus, S. P. DenBaars, J. S. Speck and U. K. Mishra, J. Appl. Phys., vol. 86, pp. 4520-4526, 1999.

[83] I.Vurgaftman, J.R.Meyer, and M. Ram, Journal of Applied Physics, vol. 89, no. 11, pp. 5815-5875, 2001.

[84] J. Piprek, UCSB: Academic Press, pp. 13-48, 2003.

[85] D. M. Caughey and R. E. Thomas, Proceedings of the IEEE, vol. 55, no. 12, pp. 2192-2193, June1967.

[86] www.silvaco.com/examples/tcad/section20/example2/index.html.

[87] S. Selberherr, Wien, New York: Springer-Verlag, 1984.

[88] A.G. Chynoweth, Phys. Rev. 109, 1537-1540, 1958.

[89] R. Van Overstraeten, and H. Deman, Solid-State Electronics 13, 583-608, 1970.

[90] I. Oguzman , et. al., J. Appl. Phys. V. 81, No. 12, 7827-7834, 1997.

[91] B. Jogai, J. App. Physics 93, 1631-1635, 2003.

[92] A. Nakajima, Y. Sumida, M. H. Dhyani, H. Kawai and E. M. S. Narayanan, Appl. Phys. Express 3, 121004, 2010.

[93] C. Buchheim, R. Goldhahn, G. Gobsch, K. Tonisch, V. Cimalla, F. Niebelschütz and O. Ambacher, Appl. Phys. Lett. 92, 013510, 2008.

[94] K. Tonisch, C. Buchheim, F. Niebelschütz, A. Schober, G. Gobsch, V. Cimalla, O. Ambacher and R. Goldhahn, J. Appl. Phys. 104, 084516, 2008.

[95] J. A. Seamons, D. R. Tibbetts, J. L. Reno and M. P. Lilly, Appl. Phys. Lett. 90, 052103, 2007.

[96] J.-J. Su and A. H. MacDonald, Nature Physics 4, 799-802, 2008.

[97] S. K. Banerjee, L. F. Register, E. Tutuc, D. Reddy, and A. H. MacDonald, IEEE Electron Device Lett. 30, 158-160, 2009.

[98] M. Saglam, K. Mutamba, A. Megej, C. Sydlo, H. L. Hartnagel, and I. Daumiller, Appl. Phys. Lett. 82, 227-229, 2003.

[99] A. Fox, G. Heidelberger, P. Kordos, and H. Luth, IEEE Electron Device Lett. 27, 945-947, 2006.

[100] T. Zimmermann, M. Neuburger, M. Kunze, I. Daumiller, A. Denisenko, A. Dadgar, A. Krost, and E. Kohn, IEEE Electron Device Lett. 25, pp. 450-452, 2004.

[101] J. Racko, M. Mikolasek, R. Granzner, N. Al Mustafa, F. Schwierz and J. Breza, Proc. ASDAM, 207-210, 2012.

[102] T. Egawa, G. Y. Zhao, H. Ishikawa, M. Umeno, and T. Jimbo, IEEE Trans. Electron Devices, vol. 48, no. 3, pp. 603–608, Mar. 2003.

[103] R. Kirschman Ed., New York: IEEE Press, 1999. (DRC), 2010, pp. 137–138, 2010.

[104] R. Chu, Y. Zhou, J. Liu, D. Wang, K.- J. Chen, and K. M. Lau, IEEE Transactions on Electron Devices, Vol. 52, No. 4, 2005.

[105] W. Choi, O. Seok, H. Ryu; H.Y. Cha and K.S. Seo, Electron Device Letters, IEEE , vol.35, no.2, pp.175,177, 2014.

[106] A.L. Corrion, M. Chen, R. Chu et al., Proc. device research conf., p. 213-214, 2011.

[107] R. Chu, A. Corrion, M. Chen et al., IEEE Electron Dev Lett, 32(5):632–4, 2011.

[108] Y. Uemoto, M. Hikita, H. Ueno, H. Matsuo, H. Ishida, M. Yanagihara, and D. Ueda, IEEE Trans. Electron Devices 54(12), 3393-3399, 2007.

[109] O. Hilt, P. Kotara, F. Brunner, A. Knauer, R. Zhytnytska and J. Wurfl, Electron Devices, IEEE Transactions on , vol.60, no.10, pp.3084,3090, Oct. 2013.

[110] J. Kashiwagi, T. Fujiwara, M. Akutsu, N. Ito, K. Chikamatsu, K. Nakahara, IEEE Electron Device Lett. 34(9), 1109-1111, 2013.

[111] Z. Xu, J. Wang, Y. Liu, J. Cai, J. Liu, M. Wang, M. Yu, B. Xie, W. Wu, X. Ma, & J. Zhang, IEEE Electron Device Lett. 34(7), 855-857, 2013.

[112] T.-H. Hung, P.S. Park, S. Krishnamoorthy, D.N. Nath and S. Rajan, IEEE Electron Device Lett. 35(3) 312-314, 2014.

[113] J. H. Lee, C. Park, K. W. Kim, & D.S. Kim, IEEE Electron Device Lett. 34(8), 975-977, 2013.

[114] J. J. Freedsman, T. Egawa, Y. Yamaoka, Y. Yano, A. Ubukata, T. Tabuchi and K. Matsumoto, Appl. Phys. Exp. 7(4), 041003, 2014.

[115] L.-Y. Su, F. Lee, & J. J. Huang, IEEE Trans. Electron Devices 61(2), 460-465, 2014.

[116] Z. Tang, Q. Jiang, Y. Lu, S. Huang, S. Yang, X. Tang, & K. J. Chen, IEEE Electron Device Lett. 34(11), 1373-1375, 2013.

[117] T. Kachi, Proc. IEEE Compound Semicond. IC Symp. Tech. Dig., pp. 13–16, 2007.

[118] M. Kodama, M. Sugimoto, E. Hayashi, N. Soejima, O. Ishiguro, M. Kanechika, K. Itoh, H. Ueda, T. Uesugi, and T. Kachi, Appl. Phys. Exp., vol. 1, no. 2, 021104, 2008.

[119] M. Kanechika, M. Sugimoto, N. Soejima, H. Ueda, O. Ishiguro, M. Kodama, E. Hayashi, T. Uesugi, and T. Kachi, Proc. Int. Workshop Nitride Semicond. Tech. Dig., p. 76, 2006.

[120] W. Huang, T. Khan, and T. P. Chow, IEEE Electron Device Lett., vol. 27, no. 10, pp. 796–798, 2006.

[121] H. Otake, S. Egami, H. Ohta, Y. Nanishi and H. Takasu, Jpn. J. Appl. Phys., vol. 46, no. 25, pp. L599–L601, 2007.

[122] K. Ota, K. Endo, Y. Okamoto, Y. Ando, H. Miyamoto, and H. Shimawaki, Tech. Dig. IEDM, 153-156, 2009.

[123] D. A. Grant and J. Guwar, "Power MOSFETs: Theory and Applications" , Wiley-Interscience, 1989.

[124] D. Marcon, M. Van Hove, B. De Jaeger, N. Posthuma, D. Wellekens, S. You, X. Kang, T. Wu, M. Willems, S. Stoffels & S. Decoutere, Proc. of SPIE Vol. 9363 936311-1, 2015.

[125] K. Matsuzawa, K. Uchida, and A. Nishiyama, IEEE Trans. Electron Devices, Vol. 47, No. 1, pp. 103-108, 2000.

[126] J. Crofton and S. Sriram, IEEE Trans. Electron Devices, Vol. 43, No. 12, 2305-2307, 1996.

[127] P. Pipinys and V. Lapeika, J. Appl. Phys. 99, 093709, 2006.

[128] S. Karmalkar, N. Satyan, and D. Mahaveer Sathaiya, IEEE Electron Device Lett., vol. 27, no. 2, pp. 87-89, 2006.

[129] R.N. Hall, Phys. Rev. 87, 387, 1952.

[130] V. M. Polyakov and F. Schwierz, Appl. Phys. Lett. 88, 032101, 2006.

[131] S. K. O'Leary, B. E. Foutz, M. S. Shur and L. F. Eastman, Appl. Phys. Lett. 88, 152113, 2006.

[132] A. G. Bhuiyan, A. Hashimoto, and A. Yamamoto, J. Appl.Phys. 94, 2779, 2003.

[133] C. H. Szwartz, R. P. Tomkins, T. H. Myers, H. Lu, and W. Schaff, phys. Stat. sol. C2, 2250-2253, 2005.

[134] M. Singh and J. Singh, J. Appl. Phys. 94, 2498-2506, 2003.

[135] Y. C. Kong, Y. D. Zheng, C. H. Zhou, Y. Z. Deng, B. Shen, S. L. Gu, R. Zhang, P. Han, R. L. Jiang, and Y. Shi, Solid-State Electron. 49, 199–203, 2005.

[136] M. T. Hasan, A. G. Bhuiyan, and A. Yamamoto, Solid-State Electron. 52, 134-139, 2008.

[137] R. Granzner, M. Kittler, and F. Schwierz, Proc. ESSDEC, 428-431, 2010.

[138] Y.-S. Lin, S.-H. Koa, C.-Y. Chan, S. S. H. Hsu, H.-M. Lee, and S. Gwo, Appl. Phys. Lett. 90, 142111, 2007.

[139] I. Mahboob, T. D. Veal, L. F. J. Piper, and C. F. McConville, Phys. Rev. B 69, 201307, 2004.

[140] T. D. Veal, P. H. Jefferson, L. F. J. Piper, C. F. McConville, T. B. Joyce, P. R. Chalker, H. Lu, and W. J. Schaff, Appl. Phys. Lett. 89, 202110, 2006.

[141] E. Tschumak, R. Granzner, J. K. N. Lindner, F. Schwierz, K. Lischka, H. Nagasawa, M. Abe, and D. J. As, Appl. Phys. Lett. 96, p. 253501, 2010.

[142] R. Granzner, E. Tschumak, M. Kittler, K. Tonisch, W. Jatal, J. Pezoldt, D. As, and F. Schwierz, J. Appl. Phys. 110, 114501 2011.

[143] V. M. Polyakov, F. Schwierz, F. Fuchs, J. Furthmüller, and F. Bechstedt, Appl. Phys. Lett. 94, 022102, 2009.

[144] W. A. Hadi, P. K. Guram, M. S. Shur, and S. K. O'Leary, J. Appl. Phys. 113, 113709, 2013.

[145] N. Nepal, N. A. Mahadik, L. O. Nyakiti, S. B. Qadri, M. J. Mehl, J. K. Hite, and C. R. Eddy Jr., Cryst. Growth Des. 13, 1485-1490, 2013.

[146] B.J. Baliga, "Silicon RF Power Devices", World Scientific, Singapore, 2005.

[147] L. Ramirez-Montes, W. Lopez-Perez, A. Gonzalez-Garcia, and R. Gonzalez-Hernandez, J. Mater. Sci. 51, 2817–2829, 2016.

[148] K. Lee, M. S. Shur, T. J. Drummond, and H. Morkoc, IEEE Trans. Electron Devices 31, 29-35, 1984.

[149] E. Ture, P. Brückner, M. Alsharef, R. Granzner, F. Schwierz, R. Quay, and O. Ambacher, Dig. IEEE MTT-S IMS, 35-37, 2017.

[150] T. Nagahisa, H. Ichijoh, T. Suzuki, A. Yudin, A. O. Adan, and M. Kubo, Jpn. J. Appl. Phys. 55, 04-01, 2016.

[151] R. Deng, S. R. Evans, and D. Gall, Appl. Phys. Lett. 102, 112103, 2013.

[152] C. Höglund, J. Birch, B. Alling, J. Bareño, Z. Czigány, P. O. Å. Persson, G. Wingqvist, A. Zukauskaite, and L. Hultman, J. Appl. Phys. 107, 123515, 2010.

[153] R. Deng, P. Y. Zheng, and D. Gall, J. Appl. Phys. 118, 015706, 2015.

[154] B. Saha, S. Saber, G. V. Naik, A. Boltasseva, E. A. Stach E. P. Kvam, and T. D. Sands, Phys. Satus Solidi B 252, 251–259, 2015.

[155] M. T. Hardy, B. P. Downey, N. Nepal, D. F. Storm, D. S. Katzer, and D. J. Meyer, Appl. Phys. Lett. 110, 162104, 2017.

[156] P. M. Mayrhofer, H. Riedl, H. Euchner, M. Stöger-Pollach, P. H. Mayrhofer, A. Bittner, and U. Schmid, Acta Mater. 100, 81-89, 2015.

[157] A. Zukauskaite, C. Tholander, J. Palisaitis, P. O. Å. Persson, V. Darakchieva, N. B. Sedrine, F. Tasnadi, B. Alling, J. Birch, and L. Hultman, J. Phys. D: Appl. Phys. 45, 422001, 2012.

[158] N. B. Sedrine, A. Zukauskaite, J. Birch, J. Jensen, L. Hultman, S. Schöche, M. Schubert, and V Darakchieva, J. Phys. D: Appl. Phys. 48, 415102, 2015.

[159] S. Zhang, W. Y. Fu, D. Holec, C. J. Humphreys, and M. A. Moram, J. Appl. Phys. 114, 243516, 2013.

[160] K. Shimada, M. Takouda, Y. Hashiguchi, S. F. Chichibu, M. Hata, H. Sazawa, T. Takada, and T. Sota, Semicond. Sci. Technol. 27 105014, 2012.

[161] K. Shimada, A. Zenpuku, K. Fujiwara, K. Hazu, S. F. Chichibu, M. Hata, H. Sazawa, T. Takada, and T. Sota, J. Appl. Phys. 110, 074114, 2011.

[162] K. Shimada, S. F. Chichibu, M. Hata, H. Sazawa, T. Takada, and T. Sota, Jpn. J. Appl. Phys. 52, 08-04, 2013.

[163] M. A. Caro, S. Zhang, M. Ylilammi, T. Riekkinen, M. A. Moram, O. Lopez-Acevedo, J. Molarius, and T. Laurila, J. Phys.: Condens. Matter 27, 279602, 2015.

[164] S. Maroldt, C. Haupt, W. Pletschen, S. Müller, R. Quay, O. Ambacher, C. Schippel, and F. Schwierz, Jpn. J. Appl. Phys. 48, 04C083, 2009.

[165] D. F. Brown, A. Williams, K. Shinohara, A. Kurdoghlian, I. Milosavljevic, P. Hashimoto, R. Grabar, S. Burnham, C. Butler, P. Willadsen, and M. Micovic, Tech. Dig. IEDM, 461-464, 2011.

[166] T. Egawa, Tech. Dig. IEDM, 613-616, 2012.

[167] S. Huang, K. Wei, G. Liu, Y. Zheng, X. Wang, L. Pang, X. Kong, X. Liu, Z. Tang, S. Yang, Q. Jiang, and K. J. Chen, IEEE Electron Device Lett. 35, 315-317, 2014.

[168] E. Ture, P. Brückner, B.-J. Godejohann, R. Aidam, M. Alsharef, R. Granzner, F. Schwierz, R. Quay, and O. Ambacher, IEEE J. Electron Devices Soc. 4, 1-4, 2016.

[169] S. W. King, R. J. Nemanich, and R. F. Davis, J. Appl. Phys. 118, 045304, 2015.

[170] S. W. King, R. J. Nemanich, and R. F. Davis, Appl. Phys. Lett. 105, 081606, 2014.

[171] O. Ambacher, B. Foutz, J. Smart, J. R. Shealy, N. G. Weimann, K. Chu, M. Murphy, A. J. Sierakowski, W. J. Schaff, L. F. Eastman, R. Dimitrov, A. Mitchell, and M. Stutzmann, J. Appl. Phys. 87, 334-344, 2000.

[172] H. A. Al-Brithen and A. R. Smith, Phys. Rev. B 70, 045303, 2004.

[173] Y. Oussaifi, A. Ben Fredj, M. Debbichi, N. Bouarissa, and M. Said, Semicond. Sci. Technol. 23, 095019, 2008.

[174] T. Oka and T. Nozawa, IEEE Electron Device Lett. 29, 668-670, 2008.